Focused Ion Beam patterning and imaging of novel spintronic devices for digital magnetic data storage, magnetic field sensing and quantum computing

Antonio Ruotolo

A dissertation submitted for the Doctor of Philosophy degree at
University of Naples

December 2006

Research is what I'm doing when I don't know what I'm doing.

Wernher von Braun

Declaration

This dissertation is submitted for the degree of Doctor of Philosophy at the University of Naples. Except where specific references are made, this work is entirely the result of my own work and includes nothing that is the outcome of work done in the Department of Physics of the Faculty of Engineering of the University of Naples, Italy. Part of the work was carried out in the Department of Materials Science of the University of Cambridge, UK and in the Micro- and Nano-Technology Department of the Fiat Research Centre of Turin, Italy. No part of this work has been or is being submitted for any other qualifications at this or any other university.

Parts of this thesis have been published, or submitted for publication as detailed below.

A. Ruotolo, A. Oropallo, F. Miletto Granozio, G.P. Pepe, P. Perna, U. Scotti di Uccio, D. Pullini, *Effect of Ga implantation and domain wall displacement in* $La_{0.7}Sr_{0.3}MnO_3$ *planar artificial spin-valves fabricated by Focused Ion Beam*, submitted (2006);

A. Ruotolo, A. Oropallo, F. Miletto Granozio, G.P. Pepe, P. Perna and U. Scotti di Uccio, D. Pullini, G. Innocenti and P. Perlo, *Novel low-field magnetoresistive devices based on manganites*, J. Magn. Magn. Mat. *in press* (2006);

A. Ruotolo, A. Oropallo, F. Miletto Granozio, G.P. Pepe, P. Perna and U. Scotti di Uccio, *Magnetic and magnetotransport properties of* $La_{0.7}Sr_{0.3}MnO_6$*/Permally heterostructures*, Appl. Phys. Lett. **88**, 252504 (2006);

A. Ruotolo, S. Wiebel, J.P. Jamet, N. Vernier, D. Pullini, J. Gierak and J. Ferré, *Magneto-optical microscopy as a favourite tool to probe focused ion beam patterning at low dose*, Nanotechnology **17**, 3308 (2006)

A. Ruotolo, D. Pullini, C. Adamo, G.P. Pepe, L. Maritato, G. Innocenti and P. Perlo, *NiCu–based superconducting devices: fabrication and characterization,* J. Phys. Conf. Series **43**, 1081 (2006);

G.P. Pepe, R. Latempa, L. Parlato, A. Ruotolo, G. Ausanio, G. Peluso, A. Barone A.A. Golubov, Ya.V. Fominov, M. Yu.Kupriyanov, *Proximity effect in planar superconducting tunnel junctions with Nb/NiCu S/F bilayers*, Phys. Rev. B **73**, 054506 (2006);

U. Scotti di Uccio, B. Davidson, R. Di Capua, F. Miletto Granozio, G. Pepe, P. Perna, A. Ruotolo, M. Salluzzo, *Effect of strain in LSMO epitaxial films with different crystallographic orientation,* J. Alloy Compd. **423**, 228 (2006).

M.G. Blamire, C. Bell, G. Burnell, D.-J. Kang, A. Ruotolo, and G. Testa, *Focused ion beam fabrication and properties of nanoscale Josephson junctions for sensors and other applications*, phys. stat. sol. (c) **2**, 1455 (2005);

A. Ruotolo, G.P. Pepe, C. Bell, C.W. Leung and M.G. Blamire, *Modulation of the dc Josephson current in pseudo spin-valve Josephson multilayers*, Supercond. Sci. Technol. **18**, 921 (2005);

A. Ruotolo, C. Bell, C.W. Leung and M.G. Blamire, *Perpendicular magnetic anisotropy and structural characterization of CuNi/Cu multilayers*, J. App. Phys **96**, 512 (2004);

G.P. Pepe, A. Ruotolo, L. Parlato, G. Peluso, G. Ausanio, G. Carapella and R. Latempa, *Nb/NiCu bilayers in single and stacked superconductive tunnel junctions: preliminary results,* J. Magn. Magn. Mat. **272-276**, e1103 (2004).

A. Ruotolo
December 2006

Acknowledgments

At the top of the list, I wish to thank my supervisor Prof. Giovanni Piero Pepe for understanding my need to always explore new paths and for walking these paths beside me. Only thanks to his expertise and patience this work can see the light.

I would also like to thank the head of the group Prof. Antonio Barone, with the hope not to have weakened his heart too much by putting a ferromagnet so close to a superconductor.

Part of this work has been possible thanks to my staying at the Department of Materials Science in Cambridge (UK). For this, I wish to thank Prof. Mark Blamire for giving me the possibility of becoming a member of his group. I would also like to thank all those in Cambridge with whom I have had the chance to exchange ideas and learn from, especially to Chris and Dennis.

Daily laboratory work can be enjoyable if shared with supportive fellow colleagues. Thanks to the HTS group: Francesco, Daniela and, specially, Davide "the joker" for making me laugh my soul out every holy day of the week. Thanks to the "lambda" boys: Gianrico, Emiliano, Mario e Giuseppe for lending me a lot of tools and helium. Thanks to the SQUID boys: Massimo and Carmela for sharing many lunches with me. Thanks to the "organic" boys: Mario, Antonio and, specially, Pasquale "the philosopher" for teaching me the ways of the female world. Thanks to Rossella and Aldo for their friendship.

Outside of the laboratory, I thank my friends, especially Francesco who has been keen on collecting my scientific publications, hence giving me the possibility to say that at least one person reads them.

And I finish with my family: those people who are always there no matter how crazy your life-choices can seem (and probably are). During the course of the project I became an uncle twice. My last thought is for my nephew and my niece, who I hope will soon be able to read this work.

A.R.

Contents

Introduction

This work deals with the fabrication and characterization of novel spintronic devices for magnetic field sensing, digital non-volatile magnetic data storage and quantum computing. The devices are patterned on nanometer scale by using a Focused Ion Beam microscope.

Moore's Law, the prediction that the number of transistors per square inch on integrated circuits will double every 18 months, has held remarkably accurate in the electronics industry since the 1970s. In recent years, however, electronic devices have been scaled down to sizes where quantum effects begin to interfere with their functioning. By incorporating one of these quantum effects, electron spin, into device design, spin electronics (or spintronics) offers a possible route to continue with the impressive gains in the capacity and speed of integrated circuits, and so much more. In spintronics both the electron charge and spin carry information.

The most common application for spintronic devices is in the data storage [1], particularly the hard disk drives. This is because the physical size of the recording bits of hard disk drives is already in the nanometer regime, and continues shrinking due to the ever-increasing demand for higher recording densities. The rapid shrinkage of bit size poses formidable challenges to the read sensors. This is because the sensor must be made smaller or at least comparable to the bit size, and at the same time, its sensitivity must be improved continuously so as to compensate the loss in signal-to-noise ratio due to the decrease in the bit size. The former has to rely heavily on the advance of nanotechnology, and the latter on the emerging field of spintronics. The combination of these two fields has played an important role in advancing the areal density of magnetic recording.

In addition to hard disk drives, the technologies developed have also been applied to magnetic random access memories (MRAMs). This type of memories combines the advantages of the fast charge-based state-of-the-art DRAM with the non-volatility of magnetic information storage. Single storage cells are written by a magnetic field and read out by a simple resistance measurement. These storage cells consist of magnetic multilayer systems, so-called spin valves or tunnel junctions [2]. A new approach for writing information to such storage cells is the current-induced magnetization switching [3]. Making use of the so-called spin transfer torque effect, magnetic layers can be switched by a current flowing through the element. The design of a possible memory device is significantly simplified, because field generating striplines are not needed any more. Initiated by the research on spin torque effects in multilayers, also the current-induced manipulation of single domain walls in nanostructures has received rapidly increasing interest both due to fundamental interest in the physics involved and due to the application background. A prominent example for a domain wall based storage device is the recently proposed racetrack memory [4]. The phenomenon of current-induced domain wall motion has been long known theoretically [5] as well as experimentally [6], but only recently controlled current-induced motion of single domain walls in magnetic nanostructures has been achieved (see for example [7,8]). The ongoing discussion within theory about the correct model for the description of spin transfer torque effects calls for in-depth experimental studies of current-induced domain wall motion.

Magnetic sensors can also be used in many other sensing fields, for instance as position, velocity and acceleration sensors for mechanical applications [9].

A less explored field in science is the use of spin-valve tunnel barrier in superconducting Josephson junctions. Ferromagnetism and superconductivity are two antagonist phenomena. Superconductivity lies on the electron-electron attraction around the Fermi surface to form Cooper pairs of electrons with antiparallel spins. In the case of ferromagnetism it is an electron repulsion, (due to Hund’s rule) that forms parallel aligned spins. In both cases the effects are only understandable on a microscopic level within the framework of quantum mechanics. Yet, when a ferromagnet and a superconductor become in contact, the behavior of the superconducting phase is complex [10] and can be exploited to realize new devices of potential applications in quantum computing.

The devices developed in this work can be divided in three main categories.

i) Multilayer-based spin valves using innovative materials;
ii) Thin-film based magnetoresistive devices based on domain wall resistivity;
iii) Superconducting spin-valve Josephson junctions.

The first two types can be used either as sensors or bit-cells in MRAMs, according with function configuration. The third type is meant to explore a new possibility towards the realization of a quantum bit cell for quantum computing.

The outline of the thesis is as follows.

In Chapter 1, the phenomenological and microscopic theories of ferromagnetism are reviewed. Magnetism in metals and manganites is explained in terms of Stoner model, for the former, and double exchange interaction, for the latter. The theory of micromagnetism is reviewed and used to introduce the Stoner-Wohlfarth model and to calculate width and energy of both unconstrained and constrained domain walls.

In Chapter 2, the intrinsic and extrinsic megnetoresistive effects are reviewed. It follows a discussion on the way these effects are, on one side, currently used to produce spintronic devices for applications and, on the other side, how they could be used for new devices. In this second part the theories of spin transfer torque in multilayers and domain walls are reviewed. Finally, the concept of spin-valve Josephson junction is introduced.

The experimental techniques used are discussed in chapter 3. The film deposition, lithography and milling used to form micron scale tracks are discussed, as well as the method of characterization of the films and multilayers in terms of structural, electrical and magnetic properties.

In Chapter 4, the basic principles of Focused Ion Beam microscopy and patterning are discussed, as well as advantages and limitations of this lithography technique as compared with other techniques. The method of processing the films in the focused ion beam to create planar devices is discussed, as well as the three-dimensional focused ion beam fabrication technique used to create current-perpendicular-to-plane junctions.

In Chapter 5, the experimental results for all of the fabricated devices are discussed, according with the classification made above. The issues related to the fabrication procedure are highlighted for each kind of devices considered.

Finally, the results are concluded and a brief outlook to possible future experiments is given.

Note on the units

Throughout this work we chose to use the SI unit system, in particular in the theoretical treatments. This statement surely will sound superfluous for those who are not familiar with magnetism. I am sure all the others will appreciate (or despise) the effort.

References

[1] M. Ziese and M. J. Thornton Eds., *Spin Electronics* (Springer, Berlin, 2001).

[2] G. A. Prinz. *J. Magn. Magn. Mater.* **200**, 57 (1999).

[3] J. C. Slonczewski, *J. Magn. Magn. Mater*. **159**, L1 (1996).

[4] S. S. P. Parkin. U.S. Patent 6,834,005.

[5] L. Berger, *J. Appl. Phys.* **49**, 2156 (1978).

[6] P. P. Freitas and L. Berger, *J. Appl. Phys.* **57**, 1266 (1985).

[7] J. Grollier, P. Boulenc, V. Cros, A. Hamzic, A. Vaurès, A. Fert, and G. Faini. *Appl. Phys. Lett.* **83**, 509 (2003).

[8] N. Vernier, D. A. Allwood, D. Atkinson, M. D. Cooke, and R. P. Cowburn, *Europhys. Lett.* **65**, 526 (2004).

[9] S. Tumanski, *Thin Film Magnetoresistive Sensors*, (Inst. of Physics Publishing, Bristol and Philadelphia, 2000).

[10] V. V. Ryazanov, V. A. Oboznov, A. Y. Rusanov, A. V. Veretennikov, A. A. Golubov, and J. Aarts, *Phys. Rev. Lett.* **86**, 2427 (2001).

Chapter 1

Basics of magnetism

The phenomenological and microscopic theories of ferromagnetism are reviewed. Magnetism in metals and manganites is explained in terms of Stoner model, for the former, and double exchange interaction, for the latter. The theory of micromagnetism is reviewed and used to calculate width and energy of constrained domain walls.

1.1 Microscopic exchange interaction

Ferromagnetism is a collective quantum mechanical phenomenon that favours parallel alignment of individual magnetic moments and gives rise to a spontaneous magnetic moment in a ferromagnet even without an external magnetic field applied. In the Heisenberg model, the effective Hamiltonian, describing the interaction of N spins $\mathbf{S}_i$, is written as [1]:

$$\mathcal{H}_{eff} = -\sum_{i,j=1}^{N} J_{i,j}\mathbf{S}_i \cdot \mathbf{S}_j = -2\sum_{i>j}^{N} J_{i,j}\mathbf{S}_i \cdot \mathbf{S}_j \,. \tag{1.1.1}$$

Conventionally, the “-“ sign is chosen so that $J_{i,j} > 0$ gives ferromagnetic coupling. The *exchange integral*

$$J_{i,j} = 2\int \phi_i^*(\mathbf{r}_1)\phi_j^*(\mathbf{r}_2)\frac{e^2}{|\mathbf{r}_1 - \mathbf{r}_2|}\phi_i(\mathbf{r}_2)\phi_j(\mathbf{r}_1)d\mathbf{r}_1 d\mathbf{r}_2 \tag{1.1.2}$$

describes the Coulomb interaction due to the overlap of the wavefunctions ϕ_i and ϕ_j. The origin of the *exchange interaction* is thus electrostatic but the explanation involves quantum mechanics. In case of interacting atoms (functions ϕ_i not orthogonal), a rough estimation of the exchange integral J always leads to a negative value. If one considers simple systems, such as the H_2 molecule, the negative exchange is easy to understand: the two electrons would prefer (due to the Coulomb term) to be near to both nuclei. Pauli exclusion forbids parallel spins occupying the same space; therefore the anti-parallel state is lower in energy. A simple physical argument can be given to understand the positive exchange integral in some systems: as a consequence of the Pauli exclusion principle, it can be energetically convenient for two electrons to have separate orbits and thus a reduced Coulomb interaction. Yet, a first principle calculation using eq. (1.1.2) is usually misleading. Even for reasonable assumptions about the functions ϕ_i the computation leads always to negative exchange integral. However, from experiment, ferromagnetism is found in, for example, the 3*d* transition metals Cobalt (Co), Nichel (Ni) and Iron (Fe), and thus the exchange integral must be positive. Ferromagnetism in metals is easier to explain by the Stoner criterion, which ignores the first principle calculations and assumes $J_{i,j} > 0$ to give a phenomenological justification for the appearance of ferromagnetism. It must also be added that eq. (1.1.2) refers to the so-called “direct” exchange interaction and is not suitable to explain ferromagnetism in more complex materials like manganites where "double" exchange interaction is the dominant mechanism.

1.2 Ferromagnetism in metals: the Stoner criterion

In metallic solid-state materials, electrons are allowed to move freely through the lattice, and therefore well-defined electronic states are spread into dispersive bands. Let us start with assuming a simplified density of states (DOS):

$$N(E) = 4\pi\left[\frac{2m_e}{h^2}\right]^{3/2}\sqrt{E} \tag{1.2.1}$$

with m_e the electron mass, h Plank's constant, and E the electron energy. The total number of electrons per unit of volume, n, is obtained by integrating $N(E)$ over energy, up to the so-called *Fermi level* E_F, the maximum occupied energy at temperature $T = 0$:

$$n = \int_0^{E_F} N(E)dE = \frac{8\pi}{3}\left[\frac{2m_e}{h^2}\right]^{3/2} E_F^{3/2}. \tag{1.2.2}$$

Therefore we can rewrite the DOS as:

$$N(E) = \frac{3n}{2E_F^{3/2}}\sqrt{E} \tag{1.2.3}$$

which at the Fermi level is:

$$N(E_F) = \frac{3n}{2E_F}. \tag{1.2.4}$$

For the Pauli exclusion principle, at each energy level there are two electrons, each with a different spin quantum number. The spin degeneracy has already been taken into account in eq. (1.2.1), so the DOS per unit of energy for each spin channel is simply half of the full DOS (Fig. 1.1a):

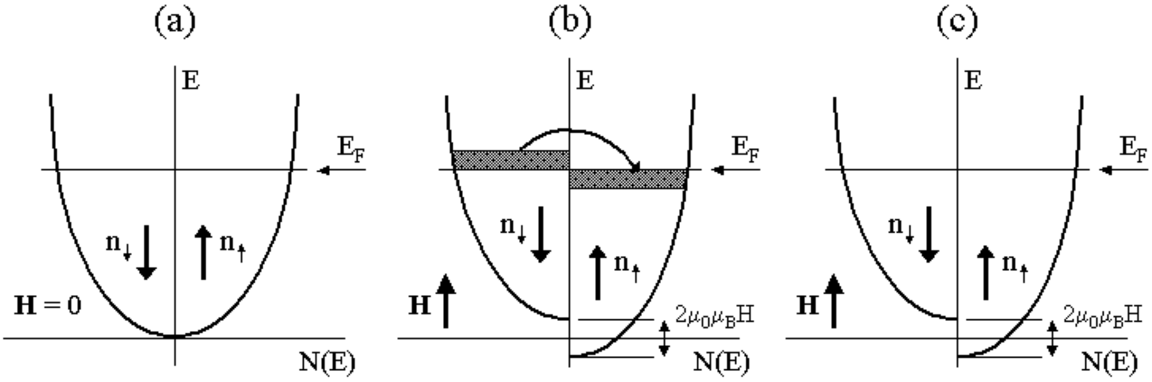

Fig. 1.1: *(a) Spin resolved density of states is balanced in zero magnetic field. Application of a field (b) shifts the sub-bands by the Zeeman energy. After redistribution up to the Fermi level (c), an unequal population of spin states is established.*

$$N_{\uparrow\downarrow}(E) = 2\pi\left[\frac{2m_e}{h^2}\right]^{3/2}\sqrt{E}\,. \tag{1.2.5}$$

When a magnetic field H is applied (Fig. 1.1b), the additional energy (*Zeeman energy*) will shift the spin-up and spin-down band with an amount $\mu\mu_0 H$, with μ the projection of the electron magnetic moment along the H axis, corresponding to $\pm\mu_B$, with μ_B the *Bohr magneton*. On a very short time scale, the electrons with spin-down (those with magnetic moment opposite to the field) will flip their spin to be accommodated in the spin-up band. This will continue until, at equilibrium, both bands are again filled up to the Fermi level (Fig. 2.1c). In this new situation, we can evaluate the number of spin-up and spin-down electrons occupying both sub-bands as:

$$2n_\uparrow = \int_{-\mu_0\mu_B H}^{E_F} N(E+\mu_0\mu_B H)dE = \int_0^{E_F+\mu_0\mu_B H} N(E)dE\,, \tag{1.2.6}$$

$$2n_\downarrow = \int_{+\mu_0\mu_B H}^{E_F} N(E-\mu_0\mu_B H)dE = \int_0^{E_F-\mu_0\mu_B H} N(E)dE\,. \tag{1.2.7}$$

Now we write down the magnetization of the conduction electrons as the population difference (per unit of volume) multiplied by the electron magnetic moment:

$$M = (n_\uparrow - n_\downarrow)\mu_B\,. \tag{1.2.8}$$

With the help of eqs. (1.2.6) and (1.2.7) this becomes:

$$2M/\mu_B = \int_0^{E_F+\mu_0\mu_B H} N(E)dE - \int_0^{E_F-\mu_0\mu_B H} N(E)dE = \int_{E_F-\mu_0\mu_B H}^{E_F+\mu_0\mu_B H} N(E)dE \tag{1.2.9}$$

with N as defined by eq. (1.2.2). When the Zeeman energy is much smaller than the Fermi energy[1], $\mu_0\mu_B H << E_F$, we can take the integrant out of the integral in the above equation. In other words, we approximate the shaded area in Fig. 1.1b by $\pm N(E_F)\mu_0\mu_B H$, as if the DOS were constant for the small applied field. Hence:

$$M = \mu_0\mu_B^2 N(E_F)H = \chi H \tag{1.2.10}$$

and the so-called *Pauli susceptibility* χ reads:

$$\chi = \mu_0\mu_B^2 N(E_F) = \frac{3\mu_0\mu_B^2 n}{2E_F}. \tag{1.2.11}$$

Here we used the free-electron DOS at the Fermi energy as given in eq. (1.2.4).

If $T \neq 0$, in eqs. (1.2.6) and (1.2.7) the DOS must be multiplied by the Fermi-Dirac function. In hypothesis that $N(E)$ does not vary rapidly with energy as compared to k_BT, after some calculation one end up with:

$$\chi = \mu_0\mu_B^2 N(E_F)\left[1 - \frac{\pi^2}{12}\left(\frac{k_BT}{E_F}\right)^2\right]. \tag{1.2.12}$$

The magnitude of the Pauli susceptibility is rather small, in accordance with experiments.

Up to now, we have considered non-magnetic metals in which no exchange interaction is at play. In magnetic metals, the interaction between magnetic moments can be approximated by an *average*, *molecular* or *exchange field*, which is assumed to be proportional to the macroscopic magnetization M. This implies we are neglecting all details of the interaction (e.g., the fluctuation interactions in space on atomic level), which is, similar to other fields in physics, referred as a *mean-field approximation*. Thus we can simply write:

---

[1] It can be easily verified that laboratory magnetic fields correspond to energies much smaller than a few eV, i.e., the typical Fermi energy.

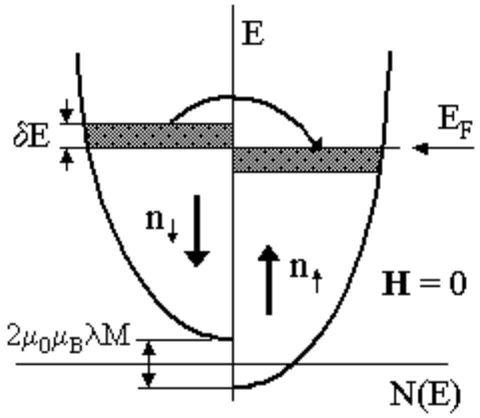

Fig. 1.2: *The exchange field splits the up- and down-band of conduction electrons, by which ferromagnetism can be stabilized.*

$$\mathbf{H}_{ex} = -\lambda \mathbf{M}, \tag{1.2.13}$$

with λ the *Weiss or molecular-field constant*. This field can be seen as the field in eqs. (1.2.6) and (1.2.7) that produces the band shift (Fig. 1.2). The magnetic energy density involved is (see eq. (1.2.8)):

$$u = \frac{\mu_0}{2}\mathbf{M}\cdot\mathbf{H}_{ex} = -\frac{\mu_0}{2}\mu_B(n_\uparrow - n_\downarrow)\lambda\mu_B(n_\uparrow - n_\downarrow) = -U(n_\uparrow - n_\downarrow)^2, \tag{1.2.14}$$

where $U = (1/2)\mu_0\mu_B^2\lambda$ is a parameter governing the strength of the magnetic interaction. We further define the *normalized excess of spin up electrons R* as:

$$R = \frac{n_\uparrow - n_\downarrow}{n}, \tag{1.2.15}$$

a number that can range between -1 and +1. Notice that R do not necessarily coincide with the so-called *electron polarization*, which defines the excess of spin up electrons at the Fermi level:

$$P = \frac{N_\uparrow(E_F) - N_\downarrow(E_F)}{N_\uparrow(E_F) + N_\downarrow(E_F)}, \tag{1.2.16}$$

Substituting eq. (1.2.15) in eq. (1.2.14):

$$u = -Un^2R^2. \tag{1.2.17}$$

If this were the only energy involved, a non-zero magnetization, i.e. $R \neq 0$, would always lead to a stable ferromagnetic state ($u < 0$). However, a second energy contribution has to be taken into account, which is the energy needed to transfer electrons from the down- to the up-band, as shown in Fig. 1.2. The amount of energy (per volume) needed to transform spin-down electrons within the energy δE to the spin-up band equals:

$$u = \frac{n_\uparrow - n_\downarrow}{2}\delta E = \frac{nR}{2}\delta E. \tag{1.2.18}$$

Therefore, the total energy required to set up a ferromagnetic magnetization is given by the sum of eqs. (1.2.17) and (1.2.18), yielding:

$$\begin{aligned} u &= -Un^2R^2 + \frac{nR}{2}\delta E \\ &= -Un^2R^2 + \frac{nR}{2}\frac{nR}{N(E_F)} \\ &= \frac{n^2}{2N(E_F)}R^2[1 - 2UN(E_F)]. \end{aligned} \tag{1.2.19}$$

Here we used the approximation: $nR = n_\uparrow - n_\downarrow = N(E_F)\delta E$, the number of states per energy times the energy interval at the Fermi level.

The equation tells us that to sustain spontaneous ferromagnetic order ($R \neq 0$) it is necessary that:

$$1 - 2UN(E_F) < 0, \tag{1.2.20}$$

or

$$2UN(E_F) > 1, \tag{1.2.21}$$

which is known as the *Stoner criterion* for ferromagnetism.

The magnetization of metallic materials, $M = (n_\uparrow - n_\downarrow)\mu_B$ (eq. (1.2.8)), can be written as $M = nR\mu_B$ with the help of eq. (1.2.15). Then eq. (1.2.19) transforms into:

$$u = \frac{M^2}{2\mu_B^2 N(E_F)}[1 - 2UN(E_F)] - \mu_0 MH, \tag{1.2.22}$$

where an additional Zeeman term has been added. Minimizing this energy ($\partial u/\partial M = 0$) leads to:

$$\chi = \frac{\mu_0 \mu_B^2 N(E_F)}{1 - 2UN(E_F)} = \frac{\chi_0}{1 - 2UN(E_F)}. \tag{1.2.23}$$

with χ_0 the Pauli-susceptibility as earlier given in eq. (1.2.11). This tells us that the susceptibility is larger by a factor determined by the interaction strength and density of states, which is often referred as the *Stoner enhancement*. This is the reason why metals with unfilled *d*-band show generally higher susceptibility when they have large $N(E_F)$, for instance Palladium (Pd).

Of course, the picture is more complicated than that considered here. Not only because temperature has been neglected (which is a reasonable assumption, unless one approaches the ferromagnetic-to-paramagnetic transition temperature, i.e. the *Curie temperature*) but also because the considered DOS is oversimplified for the *d*-band. Moreover, hybridization of *s*- and *d*-electrons has been neglected. This hybridization is instead important for interpreting the *non-integer* spontaneous moment shown by ferromagnetic metals. If we take Fe as an example, with its $3d^6 4s^2$ electronic configuration, it shows a magnetic moment of $2.2\mu_B$. From transport data, it is known that only 0.6*s* electrons effectively are still free and have their original *s*-character; the other 1.4*s* electrons are hybridized (mixed) with the *d*-electrons. This means in total 7.4 electrons have to be shared over the spin-up and spin-down bands in such a way to establish a magnetic moment of $2.2\mu_B$. It must than be: $d_\uparrow + d_\downarrow = 7.4$ and $d_\uparrow - d_\downarrow = 2.2$ per atom, which yields $d_\uparrow = 4.8$ and $d_\downarrow = 2.6$. On going from Fe to Co, the spin-up band will be completely filled. Of course, the spin down band is increasingly occupied by the addition of more *d*-electrons, which leads to a reduction of the magnetic moment. In the case of Ni ($3d^8 4s^2$), only a difference of $0.6\mu_B$ is left.

1.3 Ferromagnetism in manganites: the double exchange model

Mixed valence manganites, $Re_{1-x}Ae_x\mathrm{MnO}_3$, where *Re* is a rare earth ion an *Ae* is an alkali

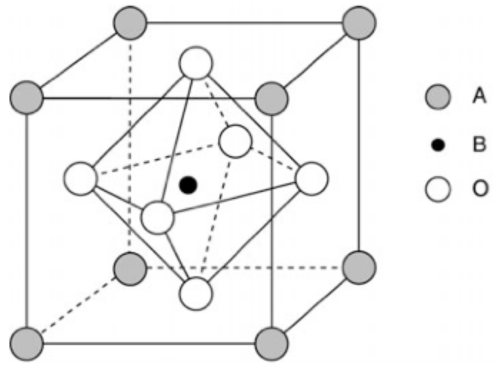

Fig. 1.3: *Schematic view of the cubic perovskite structure.*

earth, are solid solutions based on *Re*MnO$_3$ and *Ae*MnO$_3$ parent compounds. In the perovskite structure (*ABO$_3$*), the Mn ions occupy the *B*-site with octahedral oxygen coordination and the MnO$_6$ building blocks share corners to form a three-dimensional network (Fig. 1.3). As in other perovskite materials, the fundamental electronic and magnetic features in manganites come from the overlap between Mn-3*d* orbitals and O-2*p* orbitals, which form valence and conduction bands. The $x = 0$ compounds, that is the rare-earth manganites, are insulating, because only Mn^{3+} ions are present, resulting in a full band. When a divalent *Ae* replaces a trivalent *Re* ($Re_{1-x}Ae_x$MnO$_3$), Mn ions have mixed Mn^{3+} / Mn^{4+} valence. Since *x* electrons are subtracted from the band, the divalent doping implies a conducting state via the introduction of holes. In the formula $Re_{1-x}Ae_x$MnO$_3$, the average Mn valence is given by $3 + x$. At $x = 1$, that is in the alkali manganites, the compounds are again insulating because the last band is empty.

We will restrict our attention here to the manganite $La_{1-x}Sr_x$MnO$_3$, which is the compound used in this work. The electronic structure of the compound can be briefly pictured as follows. The La^{3+} (Sr^{2+}) has the same electronic configuration as xenon, and therefore it is electronically inactive. Mn^{3+} (Mn^{4+}) has four (three) electrons in 3*d*-states, the other electrons are in closed shells (argon configuration, Mn: [Ar]$3d^5 4s^2$). The electrons of O^{2-} are in neon configuration.

According to *Hund's rule*, in order to minimize the energy, all the unpaired electrons in the outer *d*-shells have their spins parallel to one another. Thus, only the five *d*-levels corresponding to the spin-up (*majority spin*) are accessible. In isolated atoms, the five *d*-orbitals are degenerate. In the cubic environment of the octahedron, hybridization and electrostatic interaction with O *p*-electrons will create a *crystal field* for the outer 3*d*-electrons. This field (estimated to be ~ 1eV [2]) lifts (*crystal field splitting*) the 5-fold degeneracy of *d*-electrons by splitting the energy levels and forming lower lying triply

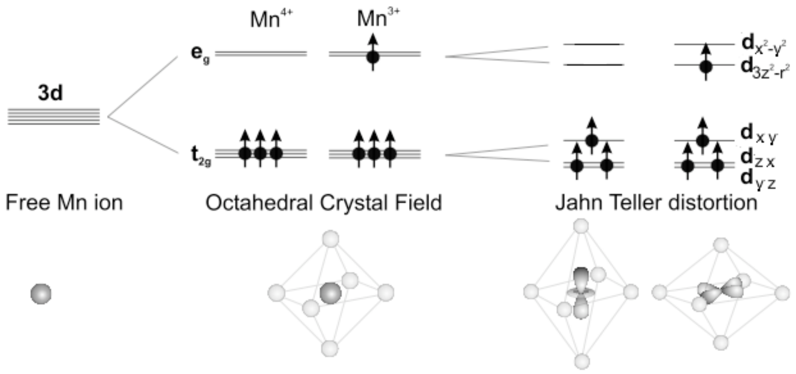

Fig. 1.4: *Crystal field lifts the degeneracy of the d-electrons of the* $Mn^{3+(4+)}$ *ions into a* t_{2g} *triplet and an* e_g *doublet. The Jahn-Teller distortion then further splits the* t_{2g} *and* e_g *levels*

degenerate t_{2g} states and a higher doublet of e_g states, as shown in Fig. 1.4. The filling of these levels still follows Hund's rule, i.e. there is strong Hund's coupling between the t_{2g} and the e_g states (antiparallel spins on either level is inhibited by Coulomb repulsion). t_{2g} orbitals are lower in energy than e_g orbitals because the latter are aligned with the O *p*-levels leading to a larger Coulomb repulsion than in other directions. Mn^{4+} has three electrons in the outer *d*-shell that can be considered as localized in the three t_{2g} levels giving a total spin $S = 3/2$ (core spin). The two e_g levels remain empty. On the other hand, Mn^{3+} has an extra electron that fills one of the e_g levels ($S = 2$). e_g levels form the conduction band.

Electrical conductivity can be explained as follows [3]. An electron is transferred from one Mn^{3+} ion to an adjacent Mn^{4+} ion by the transfer of an electron from Mn^{3+} to the oxygen that is in the middle and, simultaneously, by the transfer of an electron from the central oxygen to the Mn^{4+} ion. As two simultaneous processes are involved this model is called *double exchange* (DE). There are then two states:

$$\begin{aligned} \psi_1&: Mn^{3+} - O_2 - Mn^{4+} \\ \psi_2&: Mn^{4+} - O_2 - Mn^{3+} \end{aligned} \tag{1.3.1}$$

which are degenerate in energy. A necessary condition for this degeneracy (and hence, metallic conductivity) is that the spins of their respective *d*-shells point in the same direction, because the carrier spin does not change in the hopping process and Hund's coupling punishes anti-alignment of unpaired electrons. In other words, one of the two spin-bands (*majority band*) is completely filled while the other (*minority band*) is empty and much higher in energy. The polarization is then $P = 1$. For this reason, manganites are *half-metals* (Fig. 1.5).

This basic concept, first proposed by Zener [3], was further theoretically developed by

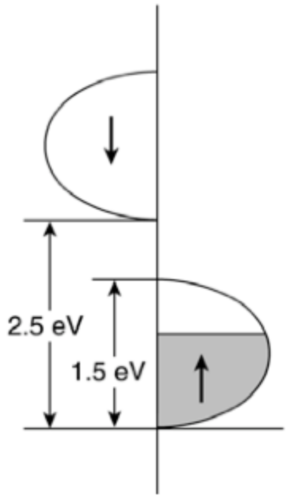

Fig.1.5: *Schematic view of the band structure of ferromagnetic doped $LaMnO_3$. The energy and filling of the band correspond to $La_{2/3}Sr_{1/3}MnO_3$* at $T = 0$.

Anderson and Hasagawa [4]. The large Hund's coupling aligns the spin of the itinerant e_g electron to the core t_{2g} spin. When an electron is transferred to a neighboring Mn ion, it has to go into the parallel state with the core of the receiving ion (Fig. 1.6). This implies that **s** has to be projected into $\mathbf{S}_2$ direction. Consequently, the transfer integral (transfer probability) t of the e_g electrons between neighboring Mn sites (via the intermediate quantum state involved with O ions) is modulated by the relative orientation of the core spins. If the internal exchange integral (Hund's coupling) J_H is much larger than the transfer integral (that is always true in manganites), then the latter can be simply expressed as:

$$t_{ij} \rightarrow t = t_0 \cos\frac{\theta}{2} \quad for \;\; J_H / t >> 1 \tag{1.3.2}$$

where θ is the angle between the core spins of the neighboring sites. Notice that t is maximum

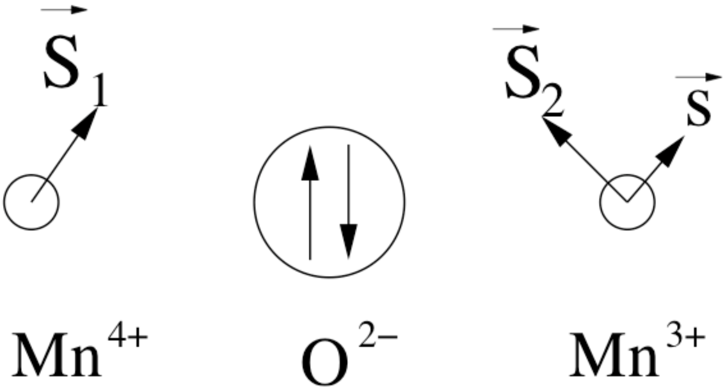

Fig. 1.6: *Semi-classical model for double exchange as seen by Anderson and Hasewaga [4].*

for $\theta = 0$ (parallel state) and minimum for $\theta = \pi$, in agreement with the ferromagnetic character of the DE interaction. The kinetic energy of the e_g electrons (which is proportional to t) is tunable by either temperature (T) or magnetic field (H).

In a simple one-band model the carrier conduction can be defined by two parameters, band-filling and bandwidth (W). The band filling varies according to x. For $x < 0.5$ carriers are holes while for $x > 0.5$ the carriers are electrons with concentration $1 - x$. They are currently labeled as hole-doped and electron-doped manganites, respectively. The bandwidth can be expressed as [5]: $W(e_g) = 2zt_0\cos(\theta/2)$ where $z = 6$ is the number of Mn nearest neighbors (single electron tight-binding approximation). t_0 has been estimated to be between 0.1eV and 0.5eV [6] while J_H is reported to be between 1.5eV and 2eV. Notice that $J_H > W$ (see Fig. 1.5), from which we find again the half-metallicity of the compound. Since J_H is the larger parameter, it can be considered ∞ in a practical sense.

The DE interaction is not the only interaction at play. There is an anti-ferromagnetic *superexchange coupling* (J_{AF}) among t_{2g} levels of nearest neighbor ions [7] mediated by the non-magnetic ion (oxygen). For $x = 0$ ($x = 1$) only Mn^{3+} (Mn^{4+}) ions are present in the crystal than DE is absent and the ground state at low temperature is antiferromagnetic. Although the superexchange coupling is much smaller than the DE coupling ($J_{AF} = 0.01t_0$ [8]), when x approaches the extreme values, the antiferromagnetic interaction still dominates on the ferromagnetic DE interaction. For intermediate values the F phase is the ground state. A naïve phase diagram picture could be then that shown if Fig. 1.7a. Actual diagram can be much more complex. This is due to the presence of effects neglected so far, among which the most important is the so-called *Jahn-Teller distortion*. Interstitial ions do not fit to maintain cubic symmetry for the MnO_6 octahedra and this leads to lower crystal symmetry, e.g. orthorhombic or rhomboedral, with the distortion of the octahedron. This distortion modifies the magnetic and electric properties depending on both the size and the concentration of the two cations present in the compound. For instance, large cations, as Ca, produce large distortion with a bending of the Mn-O-Mn bonding. This reflects in a reduction of t (see eq. (1.3.2)) and, consequently of bandwidth W and Curie temperature. Moreover, the Mn^{3+} ions are themselves Jahn-Teller active, so the contribution of the doping x is twofold.

In $La_{1-x}Sr_xMnO_3$, this distortion is rather small and in a first approximation the ideal cubic perovskite structure can be assumed. Therefore in many cases, especially when discussing thin films, a pseudo-cubic notation is used to describe the lattice parameter of the (bulk) manganite. The phase diagram of $La_{0.7}Sr_{0.3}MnO_3$ (see Fig.1.7b) resembles that of the naïve picture with a maximum T_{Curie} achieved for $x = 1/3$.

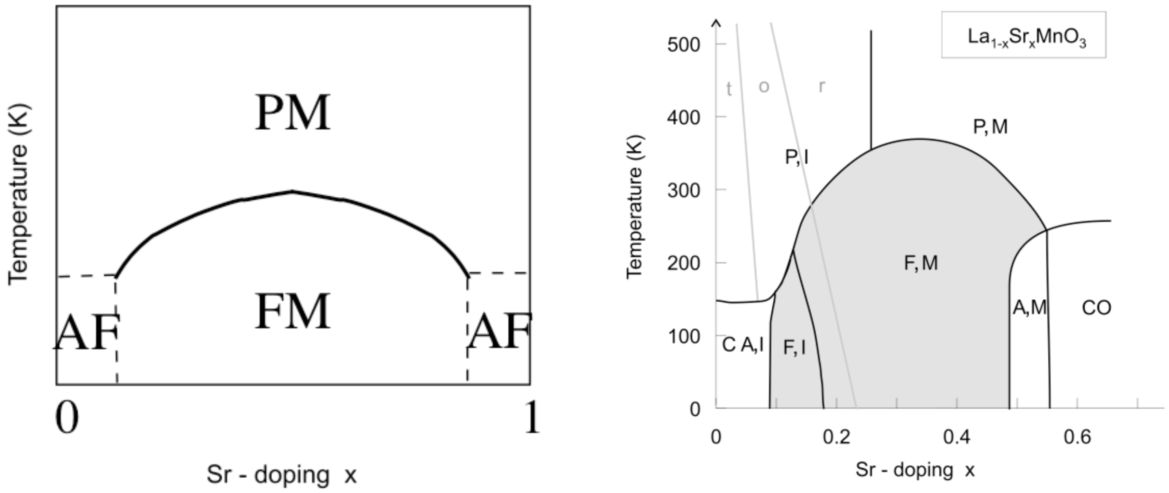

(a) (b)

Fig. 1.7: *(a) Naïve phase diagram picture where only DE and superexcange have been taken into account in a perfect cubic crystal structure; (b) actual phase diagram for* $La_{1-x}Sr_xMnO_3$. *Legend: A = antiferromagnetic, F =ferromagnetic, P = paramagnetic, M = metallic, I = insulating, CA = canted antiferromagnetic, CO = charge ordered phase; in grey the structural phases are indicated with o = orthorhombic, r = rhombohedral and t = tetragonal.*

For the sake of completeness, it is worth mentioning that the Jahn Teller effect also produces a splitting of the e_g and t_{2g} bands (see Fig. 1.4) due to the elongation of the O_6-octahedron in one direction and, consequently, a compression of the atomic planes. This effect is not observed in $La_{0.7}Sr_{0.3}MnO_3$ and hence not discussed here in details.

1.4 Micromagnetism: the Landau-Lifshitz-Gilbert equation

Sufficiently large samples display much more complex magnetic structures, such as the formation of magnetic domains. The spins in each domain remain parallel, but the magnetization directions of neighboring domains are different from each other. This is due to the presence of a large number of competing energies other than the exchange energy. The goal of micromagnetics is to find the magnetization **M**(**r**) as a function of the position **r** inside the sample, assuming that **M**(**r**) has a constant module M_S in each small volume dV: **M**(**r**) = M_S **m**(**r**) with **m**(**r**) *magnetization unit vector field* or *normalized magnetization*.

The total free energy is given by:

$$G(\mathbf{M};\mathbf{H}_a)=\int_V g_{tot}(\mathbf{M}(\mathbf{r});\mathbf{H}_a)dV=\int_V(e_{ex}+e_{an}+e_{ms}+e_h)dV \qquad (1.4.1)$$

where $g_{\mathrm{tot}}(\mathbf{M}(\mathbf{r});\mathbf{H}_{\mathrm{a}})$ is the total energy density given by the sum of exchange, anisotropy, magnetostatic and external field energies and $\mathbf{H}_{\mathrm{a}}$ is an applied external field. In the following we introduce the various energy terms involved in eq. (1.4.1).

1.4.1 Exchange energy in the continuum approximation

Consider a cubic lattice of spins, with interaction energy given by the Heisenberg Hamiltonian of eq. (1.1.1). Assume that the sum is extended to the nearest neighbors only and that the forces between spins are sufficiently strong to keep the neighbor spins almost parallel. Thus, if $\mathbf{m}_i$ ($\mathbf{m}_j$) is the unit-vector in the direction $\mathbf{S}_i$ ($\mathbf{S}_j$), such that $\mathbf{S}_i$ ($\mathbf{S}_j$) = $S\mathbf{m}_i$ ($S\mathbf{m}_j$) (S is the spin magnitude), and if $\theta_{i,j}$ is the small angle between the directions $\mathbf{m}_i$ and $\mathbf{m}_j$, one can rewrite eq. (1.1.1) as:

$$\begin{aligned}\mathcal{H} &= -2JS^2\sum\cos\theta_{i,j} \approx -2JS^2\sum 1-\frac{1}{2}\theta_{i,j}^2 \\ &= \text{const.}+JS^2\sum\theta_{i,j}^2 \approx \text{const.}+JS^2\sum(\mathbf{m}_j-\mathbf{m}_i)^2\end{aligned}, \tag{1.4.2}$$

since for small $\theta_{i,j}$, $|\theta_{i,j}| = |\mathbf{m}_j - \mathbf{m}_i|$. We now assume that the displacement vector $\mathbf{m}_j - \mathbf{m}_i$ can be written in terms of a continuous function $\mathbf{m}$ such that:

$$\mathbf{m}_j-\mathbf{m}_i=(\Delta\mathbf{r}_j\cdot\nabla)\mathbf{m} \tag{1.4.3}$$

where $\Delta\mathbf{r}_j = \mathbf{r}_j - \mathbf{r}_i$ is the position vector of neighbor j with respect to site i. Then, if $\mathbf{m} = m_x\mathbf{e}_x + m_y\mathbf{e}_y + m_z\mathbf{e}_z$,

$$\begin{aligned}\mathcal{H} &= \text{const.}+JS^2\sum\left[(\Delta\mathbf{r}_j\cdot\nabla)\mathbf{m}\right]^2 \\ &= \text{const.}+JS^2\sum\left[\left((\Delta\mathbf{r}_j\cdot\nabla)m_x\right)^2+\left((\Delta\mathbf{r}_j\cdot\nabla)m_y\right)^2+\left((\Delta\mathbf{r}_j\cdot\nabla)m_z\right)^2\right]\end{aligned} \tag{1.4.4}$$

Now we sum over j and multiply by the number of spins per unit volume n in order to obtain the energy per unit volume e_{ex}. It is important to notice that, if $\Delta\mathbf{r}_j = x_j\mathbf{e}_x + y_j\mathbf{e}_y + z_j\mathbf{e}_z$, due to the cubic symmetry it happens that $\Sigma_j x_jy_j = 0$ and $\Sigma_j x^2_j = 1/3\Sigma_j \Delta\mathbf{r}^2_j$. By using these properties and neglecting the constant term, one ends up with:

$$e_{ex}(\mathbf{m}(\mathbf{r})) = A[(\nabla m_x)^2 + (\nabla m_y)^2 + (\nabla m_z)^2]. \tag{1.4.5}$$

where the notation $(\nabla\alpha)^2 \equiv \left(\frac{\partial\alpha}{\partial x}\right)^2 + \left(\frac{\partial\alpha}{\partial y}\right)^2 + \left(\frac{\partial\alpha}{\partial z}\right)^2$ is introduced. A is *the exchange constant*, $A = \frac{1}{6}nJS^2\sum \mathbf{r}_{i,j}^2 = \frac{JS^2}{a}c$ with a edge of the unit cell and c = 1, 2 and 4 for a simple cubic, bcc and fcc cell, respectively. In case of hcp structure $c = 2\sqrt{2}$ with a distance between nearest neighbors. Typical values of A are in the order of 10^{11} J/m.

The exchange energy is an isotropic quantity because it depends only on the angle between neighbor magnetic moments and not on their relative orientation.

Although the form of exchange interaction expressed by eq. (1.4.5) has been derived for the case of direct exchange, it can be used for any types of interaction that tend to align spins parallel to each other, for instance the DE interaction, by defining an appropriate *effective* exchange stiffness.

1.4.2 Anisotropy energy

In magnetic materials the magnetization is induced to lie along specific directions called easy axes. The *spin-orbit interaction* couples the electron spins, responsible for the magnetism, to the anisotropic orbitals in a crystalline structure. The ions of the crystal create an electric potential that couples the spins to the lattice. The *anisotropy energy* is proportional to the product **L**·**S** between the orbital momentum **L** and the spin momentum **S**. Therefore, in absence of magnetic field, the energetic minimum is obtained for **S** parallel to **L**. A higher order source of anisotropy can be the stress, either tensile or compressive, applied to a crystal lattice. The stress changes the distance between neighbor ions so that the electric potential, the electronic orbitals and finally the spin-orbit coupling are modified. Both the *magnetocrystalline anisotropy* and the *stress induced anisotropy* find their origin in the spin-orbit coupling (see also Sec. 2.1.2).

For a cubic crystal, the anisotropy energy is often expressed [9] as:

$$\begin{aligned} e_c(\mathbf{m}(\mathbf{r})) &= K_0 \\ &+ K_1(\cos^2\theta_1 \cos^2\theta_2 + \cos^2\theta_2 \cos^2\theta_3 + \cos^2\theta_3 \cos^2\theta_1) \\ &+ K_2\cos^2\theta_1 \cos^2\theta_2\cos^2\theta_3 + \ldots, \end{aligned} \tag{1.4.6}$$

where K_0, K_1, K_2, … are constants and θ_1, θ_2, and θ_3 are the angles between the magnetization direction and the three crystal axes, respectively. K_0 is independent of angle and can be ignored since it is the difference in energy between different crystal orientations that is of interest. The anisotropy constants K_1 and K_2 depend on the temperature and can be obtained experimentally. In many cases, terms involving K_2 are small and can also be neglected. If $K_1 > 0$, e_c is minimum in the <100> directions; hence, these directions are the easy axes. Conversely, if $K_1 < 0$, the easy axes correspond to the <111> directions. The difference in magnetocrystalline energy between the [111] direction and the [100] direction $\Delta K_{[111]-[100]}$ is equal to $K_1/3$. Similarly, the difference between the [110] direction and the [100] direction $\Delta K_{[110]-[100]}$ is equal to $K_1/4$.

The magnetocrystalline anisotropy energy associated with a hexagonal close-packed crystal is often expressed as [10]:

$$e_u(\mathbf{m}(\mathbf{r})) = K_0 + K_1\sin^2\theta + K_2\sin^4\theta + \ldots \tag{1.4.7}$$

where K_0, K_1, K_2, … are constants and θ is the angle between the *c*-axis and the magnetization. As described above, K_0 is independent from angle. For most cases in which K_2 can be neglected, if $K_1 > 0$, the energy is smallest when $\theta = 0$, i.e. along the *c*-axis, so that this axis is the easy axis. If $K_1 < 0$, the basal plane is the easy axis. As a result of the symmetry of the hexagonal close-packed lattice, the magnetocrystalline anisotropy is a uniaxial anisotropy.

Equations (1.4.6) and (1.4.7) are volume energy densities. At surface the breaking of symmetry generates an additional term of anisotropy [11] given by:

$$e_s(\mathbf{m}(\mathbf{r})) = \tfrac{1}{2}K_s\,(\mathbf{n}\cdot\mathbf{m}(\mathbf{r}))^2 \tag{1.4.8}$$

where **n** is a unitary vector perpendicular to the surface and the constant K_s can be taken from the experiments. Note that e_s, called *surface anisotropy energy*, can favour both an in-plane or an out-of-plane magnetization and therefore the sign of K_s can be positive or negative. This surface contribution has been neglected in eq. (1.4.1) on purpose because of no relevance in the present work. It has been here introduced for the sake of completeness and must be taken into account in the case of thin films that spontaneously tend to align their magnetization out of the plane (*perpendicular magnetic anisotropy*).

1.4.3 External field energy

It is simply the Zeeman energy (already introduced in Sec. 1.2), i.e., the energy of the magnetization in an externally applied magnetic field $\mathbf{H}_a$. It can be written as:

$$e_h(\mathbf{m}(\mathbf{r})) = -\mu_0 \mathbf{M} \cdot \mathbf{H}_a = -\mu_0 M_S \mathbf{H}_a \cdot \mathbf{m}(\mathbf{r}) \tag{1.4.9}$$

1.4.4 Magnetostatic energy

The magnetization $\mathbf{M}(\mathbf{r})$ can interact also with the magnetic field generated by the body itself. In this case the energy density is given by:

$$e_{ms}(\mathbf{m}(\mathbf{r})) = -\tfrac{1}{2}\mu_0 M_s \mathbf{H}_d \cdot \mathbf{m}(\mathbf{r}) \tag{1.4.10}$$

where the *demagnetizing* or *stray field* $\mathbf{H}_d$ is generated by the sample itself. The factor ½ is introduced in order to avoid counting twice the interaction between couples of magnetic moments. It is important to notice that the magnetostatic field at a given location depends on the contributions from the whole magnetization vector field. This makes the free energy of the system being a functional. In order to calculate the magnetostatic energy we first need to evaluate $\mathbf{H}_d$. In this view we have to introduce some fundamental relations for magnetized media based on the equations of Maxwell. In absence of conduction currents the following relation is valid:

$$\nabla \times \mathbf{H}_d = 0 \tag{1.4.11}$$

In analogy with electrostatics, we can define the magnetic scalar potential ϕ that is linked to $\mathbf{H}_d$:

$$\mathbf{H}_d = -\nabla\phi \tag{1.4.12}$$

Since $\nabla \cdot \mathbf{B} = 0$, it is $\nabla \cdot \mathbf{H}_d = -\nabla \cdot \mathbf{M}$, the magnetic potential ϕ is solution of the Poisson's equation:

$$\nabla^2\phi = -\nabla \cdot \mathbf{M} \tag{1.4.13}$$

Considering the boundaries at the surface of the ferromagnet we obtain:

$$\phi(\mathbf{r}) = -\int_v \frac{\nabla\cdot\mathbf{M}(\mathbf{r}')}{|\mathbf{r}-\mathbf{r}'|} d^3r' + \oint_S \frac{\mathbf{n}\cdot\mathbf{M}(\mathbf{r}')}{|\mathbf{r}-\mathbf{r}'|} dS' \tag{1.4.14}$$

where the first is a volume integral over the body of volume V and the second is a surface integral extended to the surface S of the body. The form of eq. (1.4.14) is analogous to the electrostatic potential. In fact, the first integral can be interpreted as the potential due to a spatial distribution of a volume charge with density $\rho/\varepsilon_0 = -\nabla \cdot \mathbf{M}$; the second as the potential due to a surface charge with density $\sigma/\varepsilon_0 = \mathbf{n} \cdot \mathbf{M}$.

In general, the calculation of the stray field $\mathbf{H}_\mathrm{d}$ is complicated because it involves a three-fold integral, see eq. (1.4.14). In the case of a uniformly magnetized body $\nabla \cdot \mathbf{M} = 0$ the first integral in eq. (1.4.14) vanishes. Moreover, **M** can be taken out of the surface integral and the potential depends only on the shape of the body. In particular, if the body is of ellipsoidal shape, the demagnetizing field $\mathbf{H}_\mathrm{d}$ has the same direction as **M**:

$$\mathbf{H}_\mathrm{d} = -\mathcal{N}\mathbf{M} \tag{1.4.15}$$

where $\mathcal{N}$ is a tensor. If **M** is parallel to one of the principal axis of the ellipsoid, $\mathcal{N}$ is a number and it is called *demagnetizing factor*. The trace of the tensor $\mathcal{N}$ is 1. In a sphere for symmetry reasons the three demagnetizing factors are equal, $N_\mathrm{x} = N_\mathrm{y} = N_\mathrm{z} = 1/3$. In an infinite cylinder along the z direction $N_\mathrm{z} = 0$ while $N_\mathrm{x} = N_\mathrm{y} = 1/2$. In fact no surface charges are present at infinity, when the cylinder is magnetized along z. Similarly, a film infinitely extended in the xy plane has demagnetizing factors $N_\mathrm{x} = N_\mathrm{y} = 0$ and $N_\mathrm{z} = 1$. In all these cases it is easy to calculate the magnetostatic energy density from equations (1.4.15) and (1.4.10):

$$e_{ms} = \frac{1}{2}\mu_0(N_x M_x^2 + N_y M_y^2 + N_z M_z^2) \tag{1.4.16}$$

where M_i are the projections of the magnetization along the reference axes. In particular in the case of the infinite film eq. (1.4.16) becomes:

$$e_{ms} = \frac{1}{2}\mu_0 M_z^2 = \frac{1}{2}\mu_0 M_S^2 \cos^2\theta \qquad (1.4.17)$$

where θ is the angle of the magnetization vector with respect to the z axis. Equation (1.4.17) is characteristic of systems with uniaxial anisotropy (see eq. (1.4.7)) and is called *shape anisotropy*, because it depends only on the shape of the body. In fact, equation (1.4.17) may be generalized to the case of spheroid with $N_x = N_y \neq 0$. The minimum of equation (1.4.17) is obtained for $\theta = 90°$, i.e. when the magnetization lies in the plane of the film. The direction of the easy axis is determined by the competition between shape and crystalline anisotropy.

Notice that if the shape of the body is not ellipsoidal H_d is generally not uniform even if M is. In this case, equation (1.4.15) is no more valid.

1.4.5 Micromagnetic equations

The magnetization configuration can be determined by minimizing the free energy in eq. (1.4.1). It is important to notice that micromagnetism ignores the atomic nature of matter and the material is considered as continuous, i.e. the magnetization vector is taken as a continuous function of space. This represents the most important limit of the micromagnetism: it cannot be used when the system approaches atomic size.

The set of local minima is found by means of variational calculus. In fact, because of the precence of the magnetostatic energy, the free energy is a functional, as already discussed. The solution of the variational problem takes the form of a stability condition to be fulfilled at equilibrium [12,13]. In each point of the magnetic body is defined an *effective field* $\mathbf{H}_{\mathrm{eff}}$ given by:

$$\mathbf{H}_{eff} = -\frac{\partial G(\mathbf{m};\mathbf{H}_a)}{\partial \mathbf{m}} = \frac{2A}{\mu_0 M_S}(\nabla\mathbf{m})^2 + \mathbf{H}_{an} + \mathbf{H}_d + \mathbf{H}_a \qquad (1.4.18)$$

where $\mathbf{H}_{\mathrm{an}}$ denotes the anisotropy field defined as $\mathbf{H}_{an} = -\frac{1}{\mu_0 M_S}\frac{\partial e_{an}}{\partial \mathbf{m}}$ and $(\nabla\mathbf{m})^2 \equiv (\nabla m_x)^2 + (\nabla m_y)^2 + (\nabla m_z)^2$.

The effective field creates a torque on the magnetization that must be zero at equilibrium. Therefore the stability condition to be fulfilled in each point of the magnetic body is:

$$\mathbf{m} \times \mathbf{H}_{\mathrm{eff}} = 0 \qquad (1.4.19)$$

Equation (1.4.19) is known as Brown's equation and it is completed by the boundary condition:

$$\mathbf{m} \times \left(2A \frac{\partial \mathbf{m}}{\partial \mathbf{n}} + \frac{\partial e_s}{\partial \mathbf{m}} \right) = 0 \qquad (1.4.20)$$

where **n** is the unity vector normal to the surface. In absence of surface anisotropy, eq. (1.4.20) becomes:

$$\frac{\partial \mathbf{m}}{\partial \mathbf{n}} = 0 \qquad (1.4.21)$$

where the condition $\mathbf{m} \cdot \partial \mathbf{m}/\partial n = 0$, valid for any vector of constant magnitude, has been used.

If the system is not in equilibrium equation (1.4.19) is not fulfilled and the vector **m** precesses around the field $\mathbf{H}_{\text{eff}}$. The time dependence of the magnetization can be obtained directly from the quantum-mechanical expression for a precession of the magnetization in a magnetic field (momentum theorem), by considering the effective field to be the acting field, in SI units:

$$\frac{\partial \mathbf{m}}{\partial t} = -\gamma_0 \mathbf{m} \times \mathbf{H}_{eff} \qquad (1.4.22)$$

where t is the time and $\gamma_0 = \mu_0 \gamma = \mu_0 (g\,|e\,|)/(2m_e c) = g\mu_0\,|\mu_B\,|/\hbar$ is called *gyromagnetic ratio*. The boundary conditions are the same as in the static case.

This equation represents an undamped precession. However, from the experiments is known that the precession decays in a finite time [14]. The damping cannot be derived theoretically from basic principles, and is just added as a phenomenological term:

$$\begin{aligned} \frac{\partial \mathbf{m}}{\partial t} &= -\gamma_0 \mathbf{m} \times \left(\mathbf{H}_{eff} - \frac{\alpha}{\gamma_0} \frac{\partial \mathbf{m}}{\partial t} \right) \\ &= -\gamma_0 \mathbf{m} \times \mathbf{H}_{eff} + \alpha \mathbf{m} \times \frac{\partial \mathbf{m}}{\partial t} \end{aligned} \qquad (1.4.23)$$

where α is a phenomenological damping parameter. Eq. (1.4.23), called Gilbert's equation, is the generalization of eq. (1.4.19) to the dynamical case. If $\alpha \rightarrow 0$ the damping vanishes and the precession continues forever. If $\alpha \rightarrow \infty$ the precession is negligible compared with the damping term. Finally, if $\partial m/\partial t = 0$ the eq. (1.4.19) is recovered.

An equivalent form of eq. (1.4.19) had already been derived by Landau and Lifshitz [15], which can be derived from Gilbert's equation as follows. By vector multiplying both sides of eq. (1.4.23) by **m**, one obtains:

$$\mathbf{m}\times\frac{\partial\mathbf{m}}{\partial t} = -\gamma_0\mathbf{m}\times\left(\mathbf{m}\times\mathbf{H}_{eff}\right)+\mathbf{m}\times\left(\alpha\mathbf{m}\times\frac{\partial\mathbf{m}}{\partial t}\right); \qquad (1.4.24)$$

remembering the vector identity $\mathbf{a}\times(\mathbf{b}\times\mathbf{c}) = \mathbf{b}(\mathbf{a}\cdot\mathbf{c}) - \mathbf{c}(\mathbf{a}\cdot\mathbf{b})$ and observing that $\mathbf{m}\cdot(\partial\mathbf{m}/\partial t) = 0$, one ends up with:

$$\mathbf{m}\times\frac{\partial\mathbf{m}}{\partial t} = -\gamma_0\mathbf{m}\times\left(\mathbf{m}\times\mathbf{H}_{eff}\right)+\alpha\frac{\partial\mathbf{m}}{\partial t}; \qquad (1.4.25)$$

that is called Landau-Lifshits equation, while eq. (1.4.23) is usually called Landau-Lifshits-Gilbert (LLG) equation. Substituting the right-end side of this equation for $\mathbf{m}\times\partial\mathbf{m}/\partial t$ in eq. (1.4.23), and rearranging, leads to:

$$\frac{\partial\mathbf{m}}{\partial t} = -\gamma'\left(\mathbf{m}\times\mathbf{H}_{eff}\right)-\alpha'\mathbf{m}\times\left(\mathbf{m}\times\mathbf{H}_{eff}\right); \qquad (1.4.26)$$

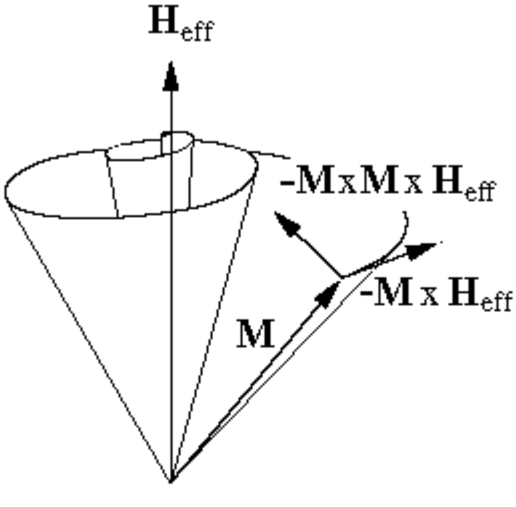

Fig. 1.8: *Geometrical interpretation of the Landau-Lifshitz-Gilbert equation.*

where $\gamma' = \gamma_0 / (1+\alpha^2)$ and $\alpha' = (\alpha\gamma_0) / (1+\alpha^2)$. This form of the LLG equation is suitable for the explicative geometrical interpretation of Fig. 1.8.

1.4.6 Domains and domain walls

A straightforward consequence of energy minimization is the formation of *domains* [16,17]. If the magnetization were homogenous throughout the sample, there would be a high cost of magnetostatic energies due to the formation of free poles. This could be avoided if the magnetization is divided into regimes known as domains and arranged in a way to minimize the stray field energy (Fig. 1.9).

In the process, boundaries are formed between adjacent domains having different magnetization directions. Abrupt transitions, however, are not favourable due to the strong exchange interaction in the ferromagnets. Instead these boundaries spread out into a region of finite thickness known as *domain walls* (DWs), in which the magnetization directions twist and form relatively smooth transitions between two domains.

Fig. 1.10a shows a *Bloch domain wall* [18] containing smoothly rotating moments, which minimises the energy cost due to the exchange interaction. For the case of thin films (that do not show significant surface anisotropy), the 'magnetic charges' formed by the Bloch wall moments rotating out of plane would cost a high magnetostatic energy, hence it is more favourable for the moments to rotate in the plane of the film. A *Néel wall* [19] (Fig. 1.10b) is formed in preference to a Bloch wall in this way. The width of the domain wall is strongly dependent on the material and its anisotropies, but is typically of the order of tens to 100 nm.

The width and the energy of a wall can be calculated (in absence of an external applied magnetic field) by minimizing the total energy of the system. Let us consider a Bloch wall

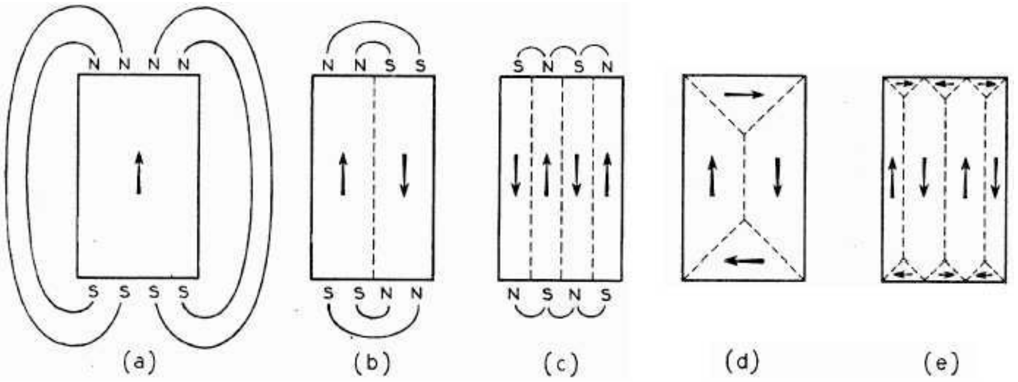

Fig. 1.9: *Origin of domains, after Kittel [17].*

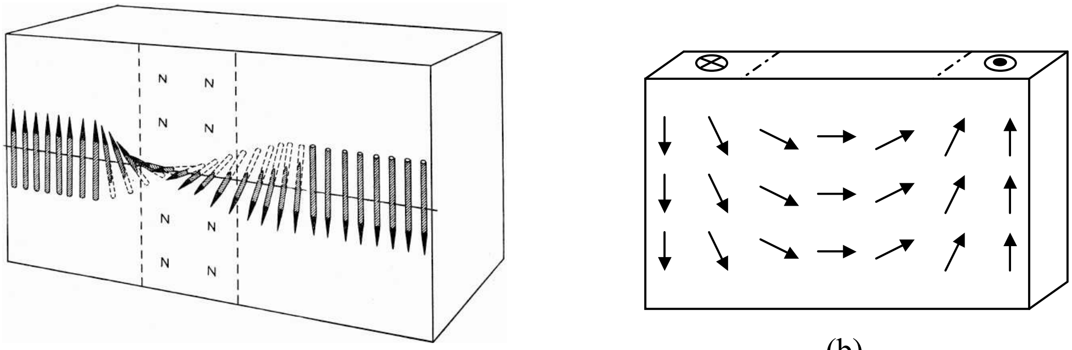

(a) (b)

Fig. 1.10: *Schematic diagrams showing (a) a 180° Bloch wall and (b) a Néel wall.*

and assume that *Ox* is the axis perpendicular to the DW. The moments make an angle θ with the *Oz* axis and the angle between two successive moments along the *x*-axis will be $\Delta\theta$. The total energy of the wall (with unit surface area) will be:

$$E(\theta) = \int_{-\infty}^{+\infty} \left[A\left(\frac{d\theta}{dx}\right)^2 + e_{an}(\theta) \right] dx \qquad (1.4.27)$$

where A is the exchange stiffness and $e_{an}(\theta)$ is the anisotropy energy density, which will be assumed to be zero along the easy directions of magnetization. $\theta(x)$ must take the values that minimize the integral. For this, if at each point x, $\theta(x)$ varies by a small amount $\delta\theta(x)$, the modification in configuration of the spins does not provoke, to first order, any variation δE, thus:

$$\delta E(\theta) = \int_{-\infty}^{+\infty} \left[2A\left(\frac{d\theta}{dx}\right)\left(\frac{d\delta\theta}{dx}\right) + \frac{de_{an}(\theta)}{\partial\theta} \right] dx = 0. \qquad (1.4.28)$$

We can write:

$$\int_{-\infty}^{+\infty} \left[2A\left(\frac{\partial\theta}{\partial x}\right)\left(\frac{d\delta\theta}{dx}\right) \right] dx = \left[2A\left(\frac{\partial\theta}{\partial x}\right)\delta\theta \right]_{-\infty}^{+\infty} - \int_{-\infty}^{+\infty} 2A\left(\frac{\partial^2\theta}{\partial x^2}\right)\delta\theta dx \qquad (1.4.29)$$

since $\partial\theta/\partial x = 0$ when $x = \pm\infty$, the first term is zero, from which:

$$\int_{-\infty}^{+\infty}\left[\frac{\partial e_{an}(\theta)}{\partial\theta}-2A\left(\frac{\partial^2\theta}{\partial x^2}\right)\right]\delta\theta dx=0. \tag{1.4.30}$$

The relation must remain true whatever the variation *δθ(x)* chosen. This implies that:

$$\frac{\partial e_{an}(\theta)}{\partial\theta}-2A\left(\frac{\partial^2\theta}{\partial x^2}\right)=0. \tag{1.4.31}$$

This is the *Euler's equation* of variational calculus. On multiplying by $\partial\theta/\partial x$ and integrating over x, one obtains:

$$e_{an}(\theta)=A\left(\frac{\partial\theta}{\partial x}\right)^2+const \tag{1.4.32}$$

but, when $x\rightarrow\pm\infty$ (within the domain), $e_{an}(\theta)=0$ and $\partial\theta/\partial x=0$, indicating that *const* is zero. Hence

$$e_{an}(\theta)=A\left(\frac{\partial\theta}{\partial x}\right)^2 \tag{1.4.33}$$

which reads: at all point of the domain wall the cost in anisotropy energy and in exchange energy balance each other. In other words, inside the domain wall, where the anisotropy energy is most costly, the angle between adjacent spin is greater, and vice versa.

The domain wall energy is:

$$E(\theta)=2\int_{-\infty}^{+\infty}e_{an}(\theta)dx \tag{1.4.34}$$

Extracting *dx* from eq. (1.4.33):

$$dx=\sqrt{\frac{A}{e_{an}(\theta)}}d\theta \tag{1.4.35}$$

one can write the general energy expression for a Bloch wall:

$$E(\theta) = 2\sqrt{A}\int_{\theta_i}^{\theta_f} \sqrt{e_{an}(\theta)}d\theta . \qquad (1.4.36)$$

For a 180° wall ($\theta_i = -\pi/2$ and $\theta_f = \pi/2$) and assuming a uniaxial anisotropy ($e_{an}(\theta) = K\cos^2\theta$):

$$E(\theta) = 4\sqrt{AK} \qquad (1.4.37)$$

From eq. (1.4.35):

$$x = \sqrt{\frac{A}{K}\int_0^{\theta}\frac{d\theta}{\cos\theta}} = \sqrt{\frac{A}{K}}\log\left[\tan\left(\frac{\theta}{2}+\frac{\pi}{4}\right)\right]. \qquad (1.4.38)$$

Since eq. (1.4.38) cannot be calculated in ($\theta = \pm\pi/2$) various definitions have been proposed for the DW width *w*. One widely accepted is that that consider the angular deviation constant and equal to the value at the centre of the wall, which yields:

$$w = \pi\left(\frac{\partial x}{\partial\theta}\right)_{x=0} = \pi\sqrt{\frac{A}{K}} \qquad (1.4.39)$$

where $\theta_f - \theta_i = \pi$ has been assumed.

In the case of a Néel wall, energy minimization will vary the angle θ from -90 to 90 by changing the magnetization parallel to the surface in order to restrict the demagnetization effects created by the proximity of the planes. The characteristic length of a Néel wall can be calculated to be:

$$w = \pi\sqrt{\frac{A}{K_d}} \qquad (1.4.40)$$

where K_d is the out-of-plane shape anisotropy constant.

It is worth mentioning that, while reducing the thickness of a film, the transition from Bloch wall to Néel wall is not sharp. In a certain region of film thicknesses, a third type of wall is observed that is named *cross-tie wall*. This kind of wall is not of interest for the present work. The reader is remanded to Ref. 20 for more information.

1.4.7 Magnetization reversal and hysteresis

The domain theory has permitted the understanding of the reversal of magnetization within ferromagnets under the influence of an external magnetic field. The process can be described qualitatively by domain nucleation, domain wall motion and magnetization rotation [9], with the aid of a hysteresis loop ($M(H)$ loop) (Fig. 1.11). Starting from a saturation field (point A in the figure), reversible magnetization rotation occurs as the field decreases (section A-B), returning the magnetization back to its anisotropy axes. As the field continues to decrease (section B-C), new domains are nucleated within the existing ones. The Zeeman energy associated with individual domains favours the 'growth' of domains with magnetization vectors along (or with a component along) the field direction, which takes place by domain wall motion. This process continues until the unfavourable domains are eliminated. The final stage of the reversal process (section C-D) involves the rotation of remaining domains from their anisotropy axes towards the field direction, finishing half of the reversal cycle. The above descriptions are highly simplified from the actual situation, and deviations are likely to happen locally due to inhomogenities.

Typical among the magnetization measurements of different ferromagnetic materials is the phenomenon of hysteresis: the magnetization of the sample does not vanish when the field sweeps towards zero. There is some lapse of field before the total magnetization comes to

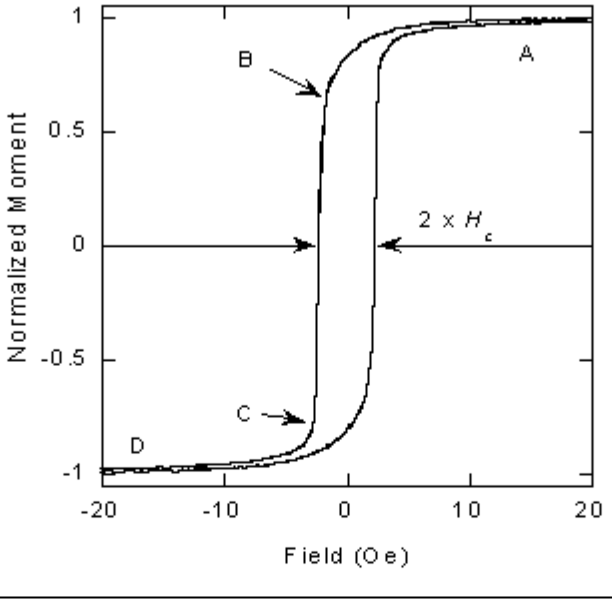

Fig. 1.11: *A typical magnetic hysteresis loop of a single layer of magnetic film. H_c is the coercivity of the film. Labels on different parts of the descending field cycle of the loop refers to the different stages of magnetization reversal, as described in the text.*

zero. Such a lapse, in the special case in which the sample was previously brought to saturation before the reverse field cycle commences, is called the coercivity of the sample (H_c). The size of coercivity is important in determining the potential applications of particular materials, and is the consequence of a number of intrinsic and extrinsic factors.

- Anisotropy

As discussed in the previous section, it is the tendency of the magnetization to stay along particular axes. Anisotropy could be either intrinsic (magnetocrystalline) or extrinsic (induced and shape) in nature. The strength of the anisotropy is the dominating factor in determining the coercivity of bulk ferromagnets in epitaxial films.

- Grain size and defects

In polycrystalline and amorphous films, other mechanisms that hinder the magnetization reversal processes can be extra sources of coercivity. These include the grain boundaries and numerous defects in the films. In general, these features act as additional barriers for the motion of domain walls. Magnetization reversal becomes more energy consuming than in perfect lattice structures, giving rise to the enhanced coercivity. On the other hand, it is also known that amorphous films do have extremely low coercivity in general [21]. In this case the defect separations are smaller than the domain wall size, which become inefficient in impeding the magnetization processes. This, together with the virtual absence of magnetocrystalline anisotropy in such films due to their amorphous nature, gives very low H_c values.

On a principle basis, the hysteresis loop can be obtained by solving the Brown's equation (eq. 1.4.19) and integrating over the volume. Yet, it is usually not easy to solve either the static equations of Brown or the dynamic LLG equation (eq. 1.4.23). Analytical solutions are particularly rare, but do exist for a few cases related to highly symmetric ferromagnets with uniaxial anisotropy. One of the most well-known examples is *coherent rotation*. Coherent rotation means that the magnetization is collinear everywhere in a ferromagnet at any time (this is for instance the case of small particles). In other words, the spins remain parallel to each other not only in the static state, but also during the magnetization reversal process. Since $\nabla \cdot \mathbf{m} = 0$, coherent rotation is a 'trivial' solution for Brown's equation. However, the result is equivalent to the model proposed earlier by Stoner-Wohlfarth (SW) [22].

The *SW model* is the most commonly employed model in describing the hysteresis behaviour of magnetic materials, although strictly speaking it deals only with polycrystalline, non-interacting, single domain particles with uniaxial anisotropy. In such a model the free energy consists of the magnetostatic energy and the Zeeman energy:

$$E = -HV\mu_0 M_S \cos(\theta - \phi) + KV\sin^2\theta \tag{1.4.41}$$

where θ is the angle between the external field and the magnetization easy axis, ϕ is the angle between the magnetization and the magnetization easy axis (see Fig. 1.12) and V is the volume. Notice that the constant K in the second term equals $½\mu_0 M_S^2$ in case of shape anisotropy.

We define a reduced energy as:

$$\eta = \frac{E}{2KV} + \text{const} = -h\cos(\theta - \phi) - \frac{\cos 2\theta}{4}, \tag{1.4.42}$$

where const = -1/4 and we have defined the reduced field:

$$h = \frac{H\mu_0 M_S}{2K}. \tag{1.4.43}$$

The magnetization at equilibrium corresponds to the free energy minimum, namely $d\eta/d\theta = 0$ and $d^2\eta/d\theta^2 > 0$:

$$\frac{\partial\eta}{\partial\phi} = h\sin(\theta - \phi) + \frac{1}{2}\sin 2\theta = 0 \tag{1.4.44}$$

$$\frac{\partial^2\eta}{\partial\phi^2} = h\cos(\theta - \phi) + \cos 2\theta > 0 \tag{1.4.45}$$

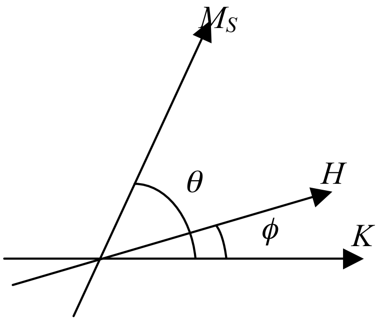

Fig. 1.12: *Definition of symbols used for the SW model.*

Because of the multi-valued trigonometric function, eq. (1.4.44) has more than one solution for a given h and ϕ, and it can happen that more than one of these solution represents an energy minimum. In order to obtain a unique solution, it is necessary to specify, and follow, the *history* of the value of h for each ϕ. A solution that starts from a particular branch cannot be just allowed to jump into another branch. The jump must be at a field value at which there is no energy barrier between these branches. This important feature is the basis of the hysteresis in magnetism. In order to see how it works it helps to look first at the trivial case $\phi = 0$. In this case eqs. (1.4.44) and (1.4.45) become:

$$(h + \cos\theta)\sin\theta = 0, \tag{1.4.46}$$

$$h\cos\theta + \cos 2\theta > 0. \tag{1.4.47}$$

One solution of eq. (1.4.46) is $\cos\theta = -h$, which is a valid solution if $|h| < 1$, but it does not fulfill eq. (1.4.47), i.e. is a maximum. The other solution is $\sin\theta = 0$, and $1 + h\cos\theta > 0$. The combination means that it is necessary to use $\theta = 0$ for $h > -1$ and $\theta = \pi$ for $h < 1$.

It is thus seen that the solution is unique if $|h| > 1$, but in the region $|h| < 1$ both $\theta = 0$ and $\theta = \pi$ are valid energy minima. At this point it is necessary to introduce the field history. If we start by applying a large positive h, then reduce the field to zero, and increase it in the opposite direction, the physical system remains on the branch of the solution $\theta = 0$ until the field $h = -1$ is reached. At this field the solution becomes unstable and the system must jump

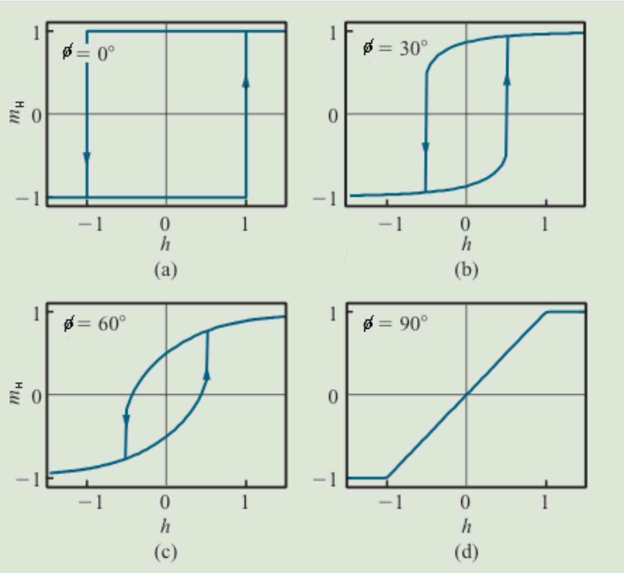

(a) (b) (c) (d)

Fig. 1.13: *Hysteresis curves calculated for various field angles with Stoner-Wohlfarth model.*

to the other branch, $\theta = \pi$. Notice that, when h passes zero the state $\theta = 0$ has a higher energy than that with $\theta = \pi$. However, the magnetization cannot jump into the lower energy state because there is an energy barrier. A reversed argument applies when starting from a large negative h. The hysteresis curve is then that represented in Fig. 1.13a with a coercivity $h = H/H_K = 1$, with $H_K = 2K/\mu_0 M_S$.

Let us consider the other extreme case $\phi = \pi/2$, i.e. field perpendicular to the easy axis. Eqs. (1.4.44) and (1.4.45) become:

$$(h - \cos\theta)\sin\theta = 0, \tag{1.4.48}$$

$$h\cos\theta - \cos 2\theta > 0. \tag{1.4.49}$$

In this case, the solution $\cos\theta = h$, which is a valid solution if $|h| < 1$, also fulfill eq. (1.4.49), i.e. is a energy minimum. It yields a magnetization proportional to the field, as in a paramagnet, with no hysteresis and with zero coercivity (Fig. 1.13d). At $h = \pm 1$ it changes over to the second solution of $\sin\theta = 0$, which is the saturation of $\theta = 0$ or $\theta = \pi$.

If $\phi \neq 0$ and $\pi/2$, eq. (1.4.44) has to be solved numerically. But the behavior is similar to the case $\theta = 0$, except that while sweeping, for instance h down from a high positive value, the minimum of eq. (1.4.44) moves down, consequently the magnetization in the field direction $M_H = M_S\cos(\theta\text{-}\phi)$ becomes smaller (see Fig. 1.13b,c), until the branch stops to be a minimum. Then there is a jump to a second branch that occurs when the left hand side of eq. (1.4.45) passes through zero. The combination of a zero for this equation with eq. (1.4.44) gives the following critical values of h_s and θ_s at which the jump occurs for a given ϕ:

$$h_s = \frac{1}{(\cos^{2/3}\phi - \sin^{2/3}\phi)^{3/2}} \tag{1.4.50}$$

$$\tan^3(\phi - \theta_s) = -\tan\phi \tag{1.4.51}$$

It should be noted that for 45° < ϕ < 90° (see Fig. 1.13c) the switching field do not correspond to the coercivity field ($h_c < h_s$). In this case h_c must be calculated by imposing $M = 0$ that yields:

$$h_c = sen\phi\cos\phi. \tag{1.4.52}$$

If one plots (h_s,θ_s) as defined in eqs. (1.4.50) and (1.4.51), or equivalently minimizes the energy density in Cartesian coordinates ($h_\perp$, $h_{//}$) that gives as the solution:

$$\begin{aligned} h_\perp &= -\cos^3\theta_s \\ h_{//} &= \sin^3\theta_s \end{aligned} \qquad (1.4.53)$$

or

$$h_{//}^{2/3} - h_\perp^{2/3} = 1, \qquad (1.4.54)$$

the so-called *SW asteroid* is obtained (Fig. 1.14). When the external field has components such that the point ($h_\perp$,h_{II}) lies outside the asteroid (point A), only one minimum of the free energy is present and the magnetization will end up there. When ($h_\perp$,h_{II}) lies inside the asteroid (point A) the situation is more complicated since there exist two minima of the free energy. This can be exploited in several ways. For some of the points inside the asteroid, although one of the field components is larger than that of point B, their magnetizations still cannot be switched. This simple mechanism makes it possible to write, for instance, the individual cell in a magnetic random access memory (as will be seen in Sec. 2.4.4).
On the other hand the dynamics of magnetization motion, which is not described by the SW model, can reach the other minimum, resulting in a switching.

The SW model can be used to have a rough estimation of the anisotropies in thin films. For instance, assuming that the film is too thin to form domains along the direction perpendicular to the film, the reversing of the magnetization along this "hard axis" can be considered coherent and the *M-H* loop will be similar to that shown in Fig. 1.13d (case ϕ =

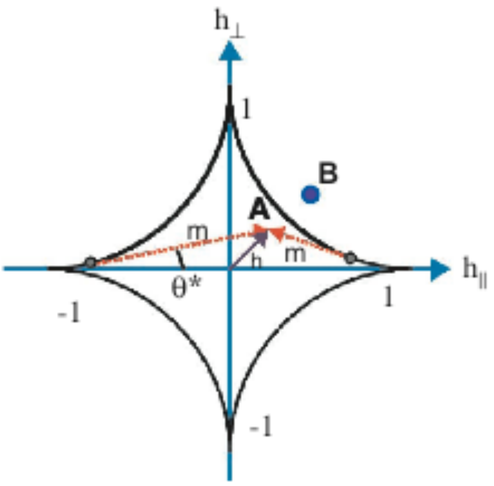

Fig. 1.14: *The Stoner-Wohlfarth asteroid.*

90°) with a *saturation field* $H_S = H_K$. When the field is instead applied in the plane, because of the formation of domains, the *M-H* loop will be similar in shape to that shown in Fig. 1.13a (case $\phi = 0°$) but with a *coercive field* $H_c \neq H_K$. If $H_c << H_K$, than K can be determined by the measurement of the out-of-plane saturation field $H_S = H_K \equiv 2K/\mu_0 M_S$.

The estimation is rather accurate when considering the shape anisotropy in thin films that do not show significant out-of-plane magnetocrystalline anisotropy or perpendicular magnetic anisotropy. It is often used to estimate in-plane magnetocrystalline anisotropies but in this case the estimation is rather rough because the hypothesis $H_c << H_S$ is not well satisfied.

1.5 Constrained domain walls

With the diffusion of the nanotechnologies it becomes interesting to study and investigate whether the DW width can be controlled by geometrical parameters when patterning down on nanometer scale.

When one is interested in the electrical transport properties of the DW (see Sec. 2.3), since the electrical resistance of a DW is determined by $d\theta/dx$, a more appropriate definition of the DW width is [23]:

$$w \equiv 4\left[\int_{-\infty}^{+\infty}\left(\frac{d\theta}{dx}\right)^2 dx\right]^{-1} = 4\left[\int_{-\pi/2}^{+\pi/2}\frac{d\theta}{dx}d\theta\right]^{-1} \tag{1.5.1}$$

where the prefactor is chosen so that the definition yields $w_0 = 2\ (A/K)^{1/2}$ for an unconstrained Bloch wall in the context of an uniaxial anisotropy.

Keeping using the coordinate system introduced in the previous paragraph, we will discuss the three models of constrictions for explicit calculation:

$$S(x) = S_0 \quad \text{for } |x| \leq d \qquad \text{(model I)}$$
$$\quad = S_1 > S_0 \quad \text{for } |x| > d$$

$$S\,(x) = S_0\,(1 + x^2/d^2) \qquad \text{(model II)}$$

$$S\,(x) = S_0 \cosh(x/d) \qquad \text{(model III)}$$

where *S(x)* is the cross section and *d* is a measure of the length of the constriction. Notice that in the model I, the most interesting in practice, 2*d* is the exact length of the constriction. Three assumptions are made in the following: (i) the wall is plane, (ii) the magnetization remains in the *yz* plane as in a Bloch wall, (iii) the dipolar interaction is neglected. This third assumption will be verified *a posteriori*. With these assumptions the total energy of the wall is easily written by introducing the cross section in eq. (1.4.27):

$$E(\theta) = \int_{-\infty}^{+\infty} \left[A\left(\frac{d\theta}{dx}\right)^2 + e_{an}(\theta) \right] S(x)dx. \tag{1.5.2}$$

The corresponding Euler's equation becomes:

$$\left(\frac{\partial^2\theta}{\partial x^2}\right) + \frac{1}{S}\left(\frac{\partial\theta}{\partial x}\right)\left(\frac{\partial S}{\partial x}\right) - \frac{1}{2A}\frac{\partial e_{an}(\theta)}{\partial\theta} = 0. \tag{1.5.3}$$

A first case in which the term $-(\partial e_{an}/\partial x)/A$ is neglected is considered. The solutions in this case are indicated by a star and take the general form [23]:

$$\theta^*(x) = \pi\left[\frac{\int_{-\infty}^{x} S^{-1}(x')dx'}{\int_{-\infty}^{+\infty} S^{-1}(x')dx'} - \frac{1}{2}\right], \tag{1.5.4}$$

$$w^* = \frac{4}{\pi^2}\frac{\left[\int_{-\infty}^{+\infty} S^{-1}(x)dx\right]^2}{\int_{-\infty}^{+\infty} S^{-2}(x)dx}, \tag{1.5.5}$$

$$E^* = \frac{\pi^2 A}{\int_{-\infty}^{+\infty} S^{-1}(x)dx}. \tag{1.5.6}$$

The term $-(\partial e_{an}/\partial x)/A$ is negligible if $w^* << w_0$. The usefulness of this approximation depends on whether *S(x)* is integrable or not. The former case is valid for model I with $S_1 = \infty$ and for model II and III. The latter for model I with S_1 finite. The exact solutions can be found in Ref. 23. What comes out is that, for the integrable case, *d* can be chosen so that $w^* << w_0$ and *w* depends only on *d*.

Actually, from an experimental point of view, the most interesting case is just the not integrable one (model I with S_1 finite). So we will focus on this case in the following. Considering for the sake of simplicity a uniaxial anisotropy, the Euler's equation is:

$$\left(\frac{\partial^2\theta}{\partial x^2}\right)+\frac{1}{S}\left(\frac{\partial\theta}{\partial x}\right)\left(\frac{\partial S}{\partial x}\right)+\frac{\sin\theta\cos\theta}{L^2}=0. \tag{1.5.7}$$

where $L \equiv \sqrt{A/K}$. In order to make the equation easily soluble, the following approximation can be made [23]:

$$\cos^2\theta \approx \alpha(\pi - 2|\theta|), \tag{1.5.8}$$

which implies:

$$\sin\cos\theta \approx \alpha\,\mathrm{sgn}(\theta), \tag{1.5.9}$$

for $|\theta| \le \pi/2$, and where α is determined variationally by minimizing the energy with respect to α for the case of unconstrained wall (eq. 1.4.27 with the approximation made). That yields α = 0.298. The analytical solution of the Euler's equation with this approximation is cumbersome and can be found in Ref. 23. We will give below only approximate expressions valid in a restricted range of parameters, from which the physical meaning appears more clearly.

If $d << w_0$, most of the magnetization rotation takes place in a region of width 2*d*. Thus, the constrained wall can be much narrower than an unconstrained Bloch wall. Three regimes can be distinguished.

If $w_0/d \le 1$, the energy and the width of the wall are approximately equal to those of the unconstrained wall. This is reasonable since in this case a Bloch wall can be completely confined in the constrain and is therefore not influenced by it.

If $1 \le w_0/d \le S_1/S_0$ the wall width and energy are the same (with the approximation eq. 1.5.8) as obtained for $S_1 = \infty$, which means the DW width depends only on the geometry of the construction while the energy is of pure exchange character. The larger is S_1/S_0, the wider is the range of values w_0/d in which the regime is achieved.

Finally, if $w_0/d \geq S_1/S_0$, the wall is again determined primarily by the competition between exchange and anisotropy energy.

It remains to verify the assumption made on the dipolar interaction, which was neglected. Assuming the dipolar energy to be given by $\frac{1}{2}\mu_0 M_S^2$ (eq. 1.4.17), the dipolar energy is obtained by multiplying by the wall volume: $E_d \approx \frac{1}{2}\mu_0 M_S^2 S_0 w$. For the case of practical interest ($1 \leq w_0/d \leq S_1/S_0$), one finds that dipolar interaction can be neglected if $d << l_{ex}$, where $l_{ex} \equiv \sqrt{2A/\mu_0 M_S^2}$ is the *exchange length*. Typical values of l_{ex} are 2.2, 4, 11.5, for Fe, Co and Ni, respectively, so the condition $d << l_{ex}$ should be valid only for point contact systems. Yet, this result has been demonstrated [24] to be valid under less restrictive hypotheses, for instance in case of negligibility of surface anisotropy and in case of Néel wall. Moreover, the wall can have Néel-type configuration for constrictions much narrower than the normal wall width, although being Bloch-type in the unconstrained case.

In conclusion, in a narrow constriction the structure of a wall becomes almost independent of the material parameters (magnetization, exchange stiffness, anisotropy constant) and is determined mostly by the geometry of the constriction. In particular, the width of the geometrically constrained domain wall is similar in size to the constriction, if the constriction is smaller than a few tens of nanometers.

References

[1] A. Aharoni, *Introduction to the Theory of Ferromagnetism* (Oxford Science Publications, 1996).

[2] A. M. Hagiri-Gosnet and J. P. Renard, *J. Phys. D: Appl. Phys.* **36**, R127 (2003).

[3] C. Zener, *Phys. Rev.* **82**, 403 (1951).

[4] P. W. Anderson and H. Hasegawa, *Phys. Rev.* **100**, 67 (1955).

[5] P. G. de Gennes, *Phys. Rev.* **118**, 141 (1960).

[6] A. P. Ramirez, *J. Phys.: Condens. Matter* **9**, 8171 (1997).

[7] R. von Helmot, J. Wecker, B. Holzapfel, L. Schultz and K. Samwer, *Phys. Rev. Lett.* **71**, 2331 (1993).

[8] F. Moussa, M. Hennion, J. Rodriguez-Carvajal, H. Moudden, L. Pinsard and A. Revcolevschi, *Phys. Rev. B* **54**, 15149 (1996).

[9] R. D. Cullity, *Introduction to Magnetic Materials* (Addison-Wesley, Reading, MA, 1972).

[10] S. Chikazumi, *Physics of ferromagnetism* (Clarendon Press – Oxford, 1997).

[11] M. T. Johnson, P. J. H. Bloemen, F. J. A. den Broeder, and J. J. de Vries, *Rep. Prog. Phys.* **59**, 1409 (1996).

[12] W. F. Brown, *J. Phys. Rev.* **58**, 736 (1940).

[13] W. F. Brown, *J. Phys. Rev.* **60**, 139 (1941).

[14] G. Bertotti, *Hysteresis in magnetism* (Academic-Press, 1998).

[15] W. F. Jr. Brown, *Micromagnetics* (Interscience, New York, 1963).

[16] L. D. Landau and E.M. Lifshitz, *Phys. Z. Sowjetunion* **8**, 153 (1935).

[17] C. Kittel, *Rev. Mod. Phys.* **21**, 541 (1949).

[18] F. Bloch, *Z. Physik* **74**, 295 (1932).

[19] L. Néel, *Comptes. Rendus* **241**, 533 (1955).

[20] D. J. Craig and R. S. Tebble, *Magnetic domains, Repts. Prog. Phys.* **24**, 116 (1961).

[21] J. Evetts, *Concise encyclopedia of magnetic & superconducting materials* (Pergamon Press, 1992).

[22] E. C. Stoner and E. P. Wohlfarth, *Phil. Trans. Roy. Soc. A* **240**, 599 (1948).

[23] P. Bruno, *Phys. Rev. Lett.* **83**, 2425 (1999).

[24] Y. Labaye, L. Berger and J. M. D. Coey, *J. Appl. Phys.* **91,** 5341 (2002).

Chapter 2

Magnetoresistive effects and spintronic devices

All the intrinsic and extrinsic megnetoresistive effects are reviewed. How these effects are exploited to produce spintronic devices for several applications is discussed. Finally, the concept of spin-valve Josephson junction is introduced.

Magnetoresistance (MR) is the change in resistance in a conductor due to an applied external magnetic field. This term has been later extended to the change of resistance due to a magnetic field in multilayer structures. Various and much different physical origins can be responsible of the effect in the different systems, although all of them are important candidates for technological applications.

We will here review all the known MR effects with particularly emphases on those of interest in this work.

MR effect can be divided into two categories: *intrinsic* and *extrinsic MR effects*. The only MR effect that cannot be strictly catalogued as either intrinsic or extrinsic is the domain wall resistivity that will be treated apart.

2.1 Intrinsic magnetoresistive (MR) effects

Intrinsic MR effects are those occurring in bulk materials or thin films. They are due to intrinsic physical phenomena only related to the structural, magnetic and electrical properties of the materials.

2.1.1 Ordinary MR (OMR)

This effect occurs in conducting films (not necessarily magnetic) and is due to the Lorentz force **F** affecting the trajectories of the conduction electrons when a magnetic field **B** is applied perpendicular to the electric field (see Fig. 2.1):

$$\mathbf{F} = -e\mathbf{v} \times \mathbf{B} \tag{2.1.1}$$

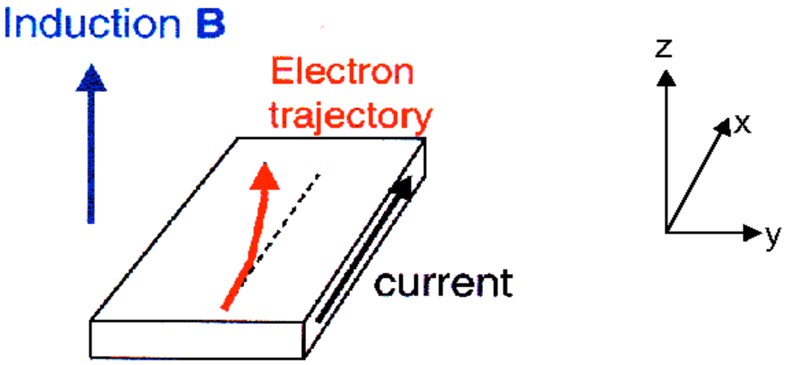

Fig. 2.1: *Effect of the Lorentz force on the electrons trajectory when a magnetic field **B** is applied along the direction z perpendicular to the electric field **E** direction x.*

with **v** electron velocity. The effect of the Lorenz force is twofold. The induced non-uniform electron distribution along z gives rise to the so-called *Hall voltage*, which varies linearly with **B**, and hence of great interest for magnetic sensing. On the other hand the non-uniform electron distribution gives rise to an increase of the resistance along x whose quadratic dependence from **B** can be easily understood: the conduction electrons see a reduced *effective cross-section* $A_{eff} < A$. From Ohm's law: $R = (l/A^2)\rho$, hence the quadratic dependence is straightforward. This effect is not much of use for several reasons. First of all, it is neither linear nor sign-dependent, while the *Hall effect* is. Moreover, the effect is much weaker than the Hall effect: in normal metals changing of resistance of 1% require fields up to 1 Tesla. Since the OMR comes along with the Hall effect, it is obviously the latter to be exploited for practical applications.

2.1.2 Anisotropic MR (AMR)

The resistance of ferromagnetic metals or alloys under a magnetic field is anisotropic and changes according to the relative orientation of the magnetization to the measuring current (Fig. 2.2). The resistance is maximum when the current is parallel to the magnetization direction and minimum when the current is perpendicular to the magnetization direction. A measure for the size of this effect is the *MR ratio*, which is defined by:

$$AMR = \frac{\rho_{//} - \rho_{\perp}}{\rho_{//}} \tag{2.1.2}$$

At intermediate angles θ between the current and the magnetization direction, the resistivity is given by:

$$\rho(\theta) = \rho_{\perp} + (\rho_{//} - \rho_{\perp})\cos^2\theta = \rho_{\perp} + \Delta\rho_{\max}\cos^2\theta \tag{2.1.3}$$

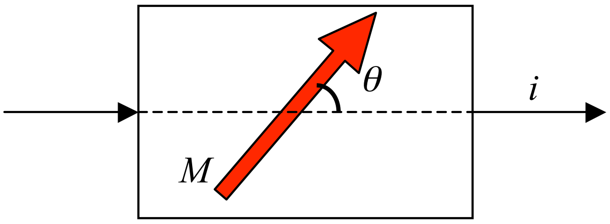

Fig. 2.2: *Plain view of the AMR effect.*

The AMR effect was already discovered in 1857 by Thomson [1] but it took a century to explain the phenomenon [2]. This is because the explanation requires quantum mechanics. AMR effect arises from the so-called *spin-orbit interaction* that is a relativistic effect that occurs when a quantum mechanical particle with a non-zero spin moves in a region with a non-zero electric field. When an electron is moving with relativistic velocities in a static electric field, in the rest frame of the electron the original static electric field transforms into a field that has also a magnetic field component, whose magnitude is given by the standard Lorentz transformation:

$$\mathbf{B}_{eff}(x) = (\mathbf{v} \times \mathbf{E}(x))/c \tag{2.1.4}$$

The presence of this effective magnetic field, that the electron feels in its rest frame, affects both the dynamics of the spin and the total energy of the electron. One should keep in mind that the only possible interaction for the spin degree of freedom is with a magnetic field, whose source can be either an externally applied magnetic field, or the *effective field* generated by the spin-orbit interaction. The static electric field causing the spin-orbit interaction can have different physical origins, for example being the electric field of the atomic nucleus, or related to the crystal or band structure of the solid.

The reader is reminded to Ref. 3 for a theoretical treatment of the spin-orbit interaction. It is interesting to recall here the naïve, but effective, picture often proposed to explain spin-orbit interaction (see Fig. 2.3). Staring from a symmetrical orbital, when the external magnetic field is applied along the current direction, the effective scattering cross-section is increased, whereas if the field is parallel to the current, the scattering cross-section is reduced.

Spin-orbit interaction is also the main mechanism at the origin of spin relaxation for conduction electrons in films. Three main spin relaxation mechanism were found as the most relevant for conduction electrons in metals and semiconductors:

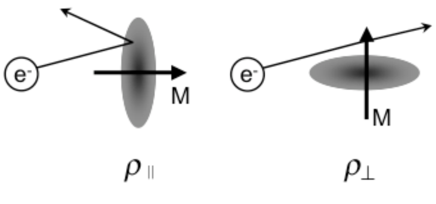

Fig 2.3: *Naïve picture of the spin-orbit coupling. The external magnetic field stretches the orbital along the field direction increasing or reducing the scattering cross-section.*

]

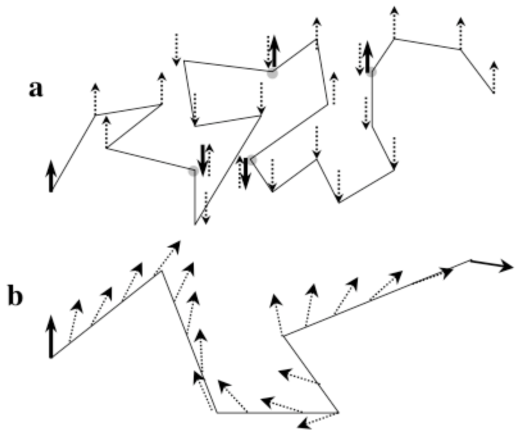

Fig 2.4: *Schematic view of the Elliot-Yafet (**a**) and the D'yakonov Perel' (**b**) relaxation mechanisms. The Elliot-Yafet spin-flip mechanism is due to the interaction of spins with the electric field of the atomic nuclei. The D'yakonov Perel' spin-flip mechanism is due to the presence of a crystal field.*

i) *the Elliot-Yafet mechanism* [4]. The lattice ions induce a local atomic electric field, which via the spin orbit interaction will mix spin up and spin down states (see fig. 2.4a). The Elliot-Yafet mechanism leads to a *spin relaxation rate* $1/T$ proportional to the momentum scattering rate. Usually this is expected to be the main spin-flip mechanism in metals. If Elliot-Yafet is the main spin scattering mechanism, the *spin flip length* ($\lambda_{sf} = \sqrt{D\tau_{sf}}$, *D spin averaged diffusion constant* and τ_{sf} *spin-flip time*) will be linearly proportional to the mean free path

ii) *the D'yakonov Perel' mechanism* [5]. This mechanism is related to a lift in spin degeneracy due to the presence of a finite electric field in crystals lacking inversion symmetry (the crystal field already encountered in Sec. 1.3). Therefore, the electrons feel a momentum-dependent effective magnetic field and the spin precesses around this effective field (see fig. 2.4b). The process can be imagined as a random walk in spin space. The spin relaxation rate induced by the D'yakonov Perel' mechanism will be inversely proportional on the momentum scattering rate, therefore the corresponding spin flip length is independent of the mean free path (the dependence on the momentum scattering rate is cancelled out by the diffusion constant).

iii) *the Bir-Aronov Pikus mechanism* [6] is due to the electron-hole exchange interaction, and it plays an important role in semiconductors with a high overlap between the electron and hole wavefunctions. Fluctuations in the effective hole concentration, due to different effective mass, produce a fluctuating effective magnetic field generated by the total spin of holes. This induces a precession of the electron spin around an instantaneous axis, analogous to the D'yakonov Perel' mechanism.

2.1.3 Colossal MR (CMR)

Colossal MR refers to the large change of resistance observed in manganites when a high magnetic field is applied.

In 1993 von Helmholt et al. [7] observed an $((R(7T)-R(0))/R(0)$ ratio of 60% at room temperature in $La_{0.67}Ba_{0.33}MnO_3$ thin film. In the following year, Jin et al. [8] reported an MR effect of millions percent at 77K in $La_{0.67}Ca_{0.33}MnO_3$ thin film. The effect is believed to arise from the close correlation between the magnetic phase transition and the electronic phase transition near the Curie Temperature T_{Curie}, though the fundamental physics is yet to be understood. A qualitative explanation of the phenomenon is that pictured in Fig. 2.5: close to the transition temperature, a high magnetic field forces the spin to align parallel, therefore forcing the transition from insulating to metal phase (see Sec. 1.3).

Because the CMR effect requires large magnetic fields (several Tesla) near T_{Curie}, imminent technological applications are largely limited at the moment. As will be shown in the following paragraph, manganites can be used for low-field applications by using extrinsic MR effects.

2.2 Extrinsic magnetoresistive effects

Extrinsic MR effects are those occurring in heterostructures composed by magnetic and non-magnetic thin films. They are due to extrinsic physical phenomena only related to the magnetic properties and the magnetic coupling of the films in the structure.

2.2.1 Giant magnetoresistive effect (GMR)

Giant magnetoresistance (GMR) occurs in ferromagnetic/non-magnetic (F/N) multilayers when the current is applied either in the plane or perpendicular to the plane of the structure.

GMR was discovered in 1988 [9] in a superlattice multilayer with alternating Fe and Cr

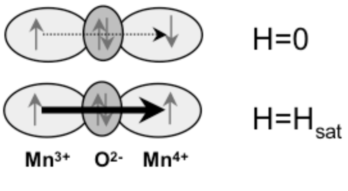

Fig 2.5: *Schematic picture of the CMR effect. The external magnetic field aligns spin parallels, forcing a transition from insulating to metal phase.*

layers. As shown in Fig. 2.6a, the resistance of such a superlattice structure is high at zero field, decreases when a magnetic field is applied in both directions along the sample surface, and finally saturates at a field of about 2T. The MR ratio of superlattices with an [Fe(3 nm)/Cr(0.9 nm)]$_{60}$ structure was measured to be about 45% at 4.2 K, which is much larger than the AMR effect. It was proved soon afterward that the resistance of the superlattice structure depends on the relative orientation of the magnetization of the adjacent magnetic layers.

In a F/N multilayer, the nearest neighbor adjacent F layers can spontaneously align either parallel (P) (ferromagnetic coupling) or antiparallel (AP) (antiferromagnetic coupling) according to the N spacer thickness. This effect is called *interlayer exchange coupling* because it can be seen as the "macroscopic" version of the microscopic direct exchange coupling expressed by eq. (1.1.1). Starting from eq. (1.1.1), if one substitutes the single spin $\mathbf{S}_{i,j}$ with the "macroscopic spins" represented by the magnetizations $\mathbf{M}_{i,j}$ in the two adjacent F-layers (assumed uniformely magnetized), then eq. (1.1.1) reads:

$$\mathcal{H}_{i,j} = -J_{i,j}\mathbf{M}_i \cdot \mathbf{M}_j \tag{2.2.1}$$

If one writes the exchange integral in accordance with the Ruderman-Kittel-Kasuya-Yoshida, or RKKY, theory (originally developed to explain the oscillatory spin polarization behavior of dilute magnetic clusters in a non-magnetic host) [11]:

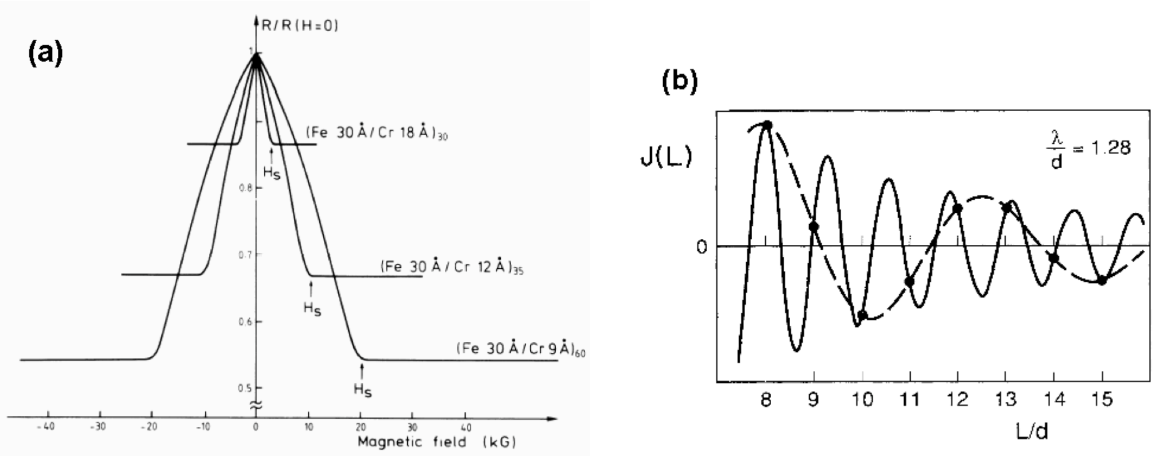

Fig. 2.6: *(a) Magnetoresistance of Fe/Cr superlattices. Both the current and the applied field are along the same [110] axis in the film plane. Taken from [9]. (b) Exchange-coupling strength of two ferromagnetic layers across a monovalent fcc (100) metal (arbitrary units) calculated using the continuum version of the RKKY model. Broken curve: the actual coupling strength with the experimentally measured periodicity for L = Nd. Here, L is the thickness of the spacer, d is the atomic layer spacing in the thickness direction, and N is an integer number. Taken from [10]*

$$J \propto \frac{\sin(2k_F t_N)}{t_N^{\,2}} \tag{2.2.2}$$

with t_N thickness of the normal layer and k_F Fermi wavevector. This model predicts accurately the oscillation behavior and the rate of decay of the coupling strength observed experimentally (see Fig. 2.6b) but fails in predicting the period, which is overestimated. This is because the model suffers from a number of drawbacks. The model, strictly speaking, should not be applicable to 3*d* transition metal ferromagnets due to their itinerant nature: electrons responsible for magnetism in these metals also take part in conduction. Besides, the above model is based on the free electron assumption, which have spherical Fermi surface. The true Fermi surface topology (which is never spherical even in the case of noble metals like Cu or Au) plays a decisive part of the oscillation period(s). Moreover, the discrete nature of atomic planes in multilayers must be taken into account. Sampling of the coupling strength through the spacer can only take place at integral values of atomic planes in the growth direction. By taking the true picture into account, Bruno and Chappert [12] managed to predict the presence of the multiple periods of oscillations in some systems, which have been observed experimentally. The period of oscillation is given by $\Lambda = \left|\frac{k_F}{\pi} - \frac{n}{d}\right|^{-1}$, d being the lattice parameter along the growth direction and n is an integer.

In this framework, the explanation of the results shown in Fig. 2.6a, for $t_{Cr} = 0.9$ nm is straightforward: for the values of t_{Cr} reported in Fig. 2.6a, J is always negative (AF coupling).

In Fig. 2.6a the resistance is detected by applying the current in the plane (CIP configuration). Larger MR ratio can be achieved by making the current pass perpendicular to the planes (CPP configuration). In both cases the resistance can be written, considering a trilayer structure, in the following form [13] comparable to eq. (2.1.3):

$$R(\theta) = R_o + \frac{\Delta R_{GMR}}{2}(1 - \cos\theta) \tag{2.2.3}$$

with θ is the angle between the magnetization directions of the F-layers.

It remains the question why the resistance is higher in the AP configuration as compared to the case of P configuration. The main idea behind all the models proposed is the difference of resistivities between the spin up and spin down electron channels, first proposed by Mott [14].

The mechanism of GMR can be understood using the simple two-current model [15]. Consider a trilayer with two magnetic layers separated by a non-magnetic metallic spacer layer. Assume that the thickness of the N-layer is much smaller than the *spin diffusion length* λ_{sd} that is the lengthscale over which the spin accumulation (that decay exponentially from the F/N interface) is conserved. We can thus assume that electrical current in the trilayer flows in two channels, one corresponding to electrons with spin up and the other to electron with spin down. Since the up- and down-spin channels are indipendent (spin is conserved) they can be regarded as two wires connected in parallels.

The electron with different spin polarization are scattered in a different way when they enter an F-layer. Given that electrons obey the Pauli exclusion principle, an electron can be scattered from an impurity only to quantum states that are not occupied by other electrons. At zero (low) temperatures, all the states with energy E below the Fermi energy E_F are occupied and those with $E > E_F$ are empty. Since scattering from impurities is elastic (energy conservation), electrons at the Fermi level (which carry the current) can be scattered only to states in the immediate vicinity of the Fermi level. It follows that the scattering probability is proportional to number of states available for scattering at E_F, i.e. to the density of states $N_{\uparrow\downarrow}(E_F)$. Different $N_\uparrow(E_F) \neq N_\downarrow(E_F)$ implies different scattering probability.

Assume now that electrons with spin antiparallel to the magnetization are scattered more strongly. This is for instance the case for the Co/Cu combination but the opposite is true for the Fe/Cr system (see Fig. 2.7). The GMR effect can be explained qualitatively using the resistor model shown in Fig. 2.8. In the P-configuration electrons with ↑ spin are weakly

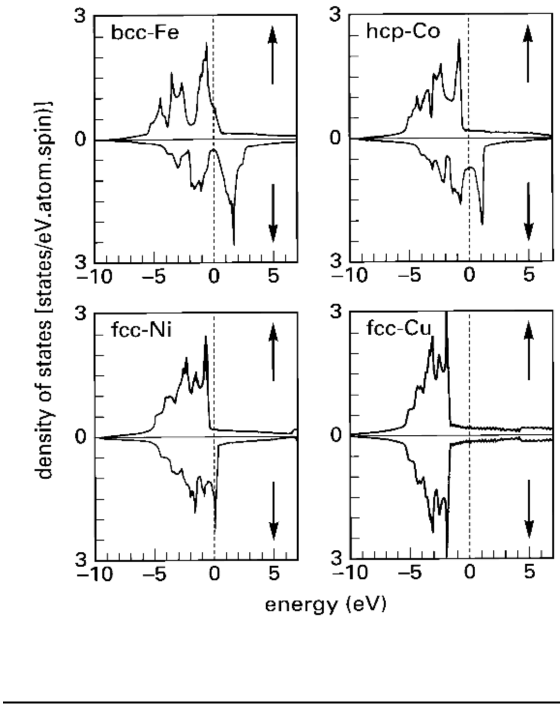

Fig. 2.7: *Calculated DOS for Fe, Co, Ni and Cu. Notice that $N_\uparrow(E_F) < N_\downarrow(E_F)$ for Co an Ni, while $N_\uparrow(E_F) > N_\downarrow(E_F)$ for Fe.*

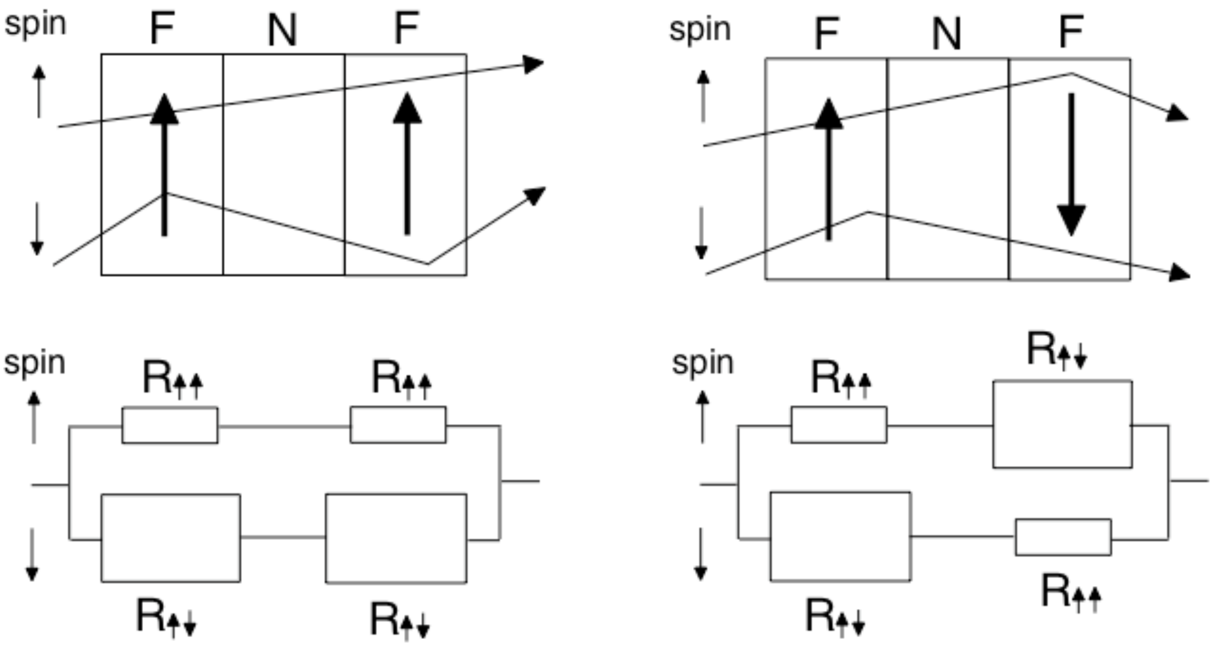

(a) (b)

Fig. 2.8: *Resistor model of GMR.*

scattered both in the first and second ferromagnet, whereas the ↓ electrons are strongly scatterd in both F-layers. This is modeled by two small resistors in the ↑ channel and by two large resistors in the ↓ channel, in the equivalent resistor network shown in Fig. 2.8a. Since the ↑ and ↓ channel are connected in parallel, the total resistance is determined by the low-resistance ↑ spin channel that shorts the high-resistance ↓ spin channel and is given by:

$$\rho_P = \frac{\rho_{\uparrow\uparrow}\rho_{\uparrow\downarrow}}{\rho_{\uparrow\uparrow} + \rho_{\uparrow\downarrow}} \tag{2.2.4}$$

On the other hand, ↓ spin electrons in the AP configuration are strongly scattered in the first F-layer but weakly scattered in the second F-layer. The ↑ spin electrons are weakly scattered in the first F-layer but strongly scattered in the second F-layer. This is modeled in Fig. 2.8b. There is no shorting now and the total resistance is much higher:

$$\rho_{AP} = \frac{\rho_{\uparrow\uparrow} + \rho_{\uparrow\downarrow}}{2} \tag{2.2.5}$$

The MR ratio is thus given by:

$$MR = \frac{\rho_P - \rho_{AP}}{\rho_{AP}} = -\left(\frac{\rho_{\uparrow\uparrow} - \rho_{\uparrow\downarrow}}{\rho_{\uparrow\uparrow} + \rho_{\uparrow\downarrow}}\right)^2 \tag{2.2.6}$$

The negative sign indicates that the resistivity at saturation state is lower than that at the zero-field state.

In the above discussion we have discarded a second type of scattering that occurs in both the N- and F-layers, that is spin-flip scattering. Alike from the *spin dependent scattering*, which causes the GMR, the spin flip scattering is detrimental to the GMR. In the case of spin dependent scattering the orientation of the electron spin is conserved but the probability of scattering for ↑ and ↓ electrons is different. In the spin flip scattering, the spin orientation changes from $\mathbf{s} = \hbar/2$ to $\mathbf{s} = -\hbar/2$ or vice versa and, at the same time, the spin of the scattering centre changes by $\Delta = \hbar$ so that the total spin is conserved.

There are several sources of spin-flip scattering. In the non-magnetic spacer, some of the magnetic atoms may enter during the multilayer preparation. When an electron is scattered off a magnetic impurity, the spin of the electron traveling and that of the impurity can interchange. This causes a reduction of the spin diffusion length in the N-layer. Another origin of spin flip is the spin orbit interaction that can occur both in the F-layers, as already discussed in Sec. 2.1.2, and in the N-layer. In the N-layer, the spin orbit scattering shortens the mean free path and then reduces the spin diffusion length. Finally, electron can be scattered in the F-layers from spin-waves. Spin-waves are quasiparticles with spin one, therefore creation (annihilation) of a spin-wave in collision with an electron leads to a flip of the electron spin. Since creation (annihilation) of spin waves involves the spin-wave energy, this is an inelastic process, which is important at elevated temperatures.

Readers interested in extension of the model to the case of spin diffusion length comparable to the N-layer thickness (Valet-Fert model) are reminded to Refs. 16 and 17. A quantitative treatment of the GMR effect is possible using either the Boltzmann transport equation [18,19] or the quantum Kubo formula [20,21] using either the simple parabolic band structure or the more realistic band structures [22,23].

2.2.2 Tunnel magnetoresistive effect (TMR)

It can be regarded as CPP GMR effect in magnetic tunnel junctions (MTJs) where the electrical conduction is based on spin-dependent quantum mechanical tunneling across a thin potential barrier. To have a sound understanding of MTJ, we first look at the basic properties of a normal non-magnetic tunnel junction. A typical quantum-mechanical tunnel junction is a sandwich of two conductive electrodes separated by a thin insulating barrier layer. For a tunnel junction with a sufficiently high potential barrier, the tunneling current can be calculated using the transfer Hamiltonian approach, which reads [24]:

$$\begin{aligned} I = A\int_{-\infty}^{+\infty} |\mathbf{T}|^2 N_1(E + E_{F1}) N_2(E + E_{F2} + eV) \\ \times [f(E + E_{F1}) - f(E + E_{F2} + eV)]dE \end{aligned} \tag{2.2.7}$$

where **T** is the matrix element of the transfer Hamiltonian, *A* is a constant, *V* is the applied voltage and *f* is the Fermi.Dirac distribution function. In the case where the voltage applied across the junction is small, one has:

$$f(E + E_{F1}) - f(E + E_{F2} + eV)] = -\left.\frac{\partial f}{\partial E}\right|_{E=E_F} (eV) \tag{2.2.8}$$

$$G(V = 0) = \frac{dI}{dV} \propto |\mathbf{T}| N_1(E_F) N_2(E_F) \tag{2.2.9}$$

where *G* is the conductance. For tunnel junctions with ferromagnetic electrodes, eq. (2.2.9) is still valid, except that N_1 and N_2 are now dependent on the spin polarization of electrons. This is known to result in a different tunneling conductance between the parallel and antiparallel alignment of the magnetizations of the two electrodes, as shown schematically in Fig. 2.9. The total conductance in the parallel configuration is thus approximately given by:

$$G_P(0) \propto N_1^{\uparrow}(E_F) N_2^{\uparrow}(E_F) + N_1^{\downarrow}(E_F) N_2^{\downarrow}(E_F) \tag{2.2.10}$$

and that in the antiparallel configuration is:

$$G_{AP}(0) \propto N_1^{\uparrow}(E_F) N_2^{\downarrow}(E_F) + N_1^{\downarrow}(E_F) N_2^{\uparrow}(E_F) \tag{2.2.11}$$

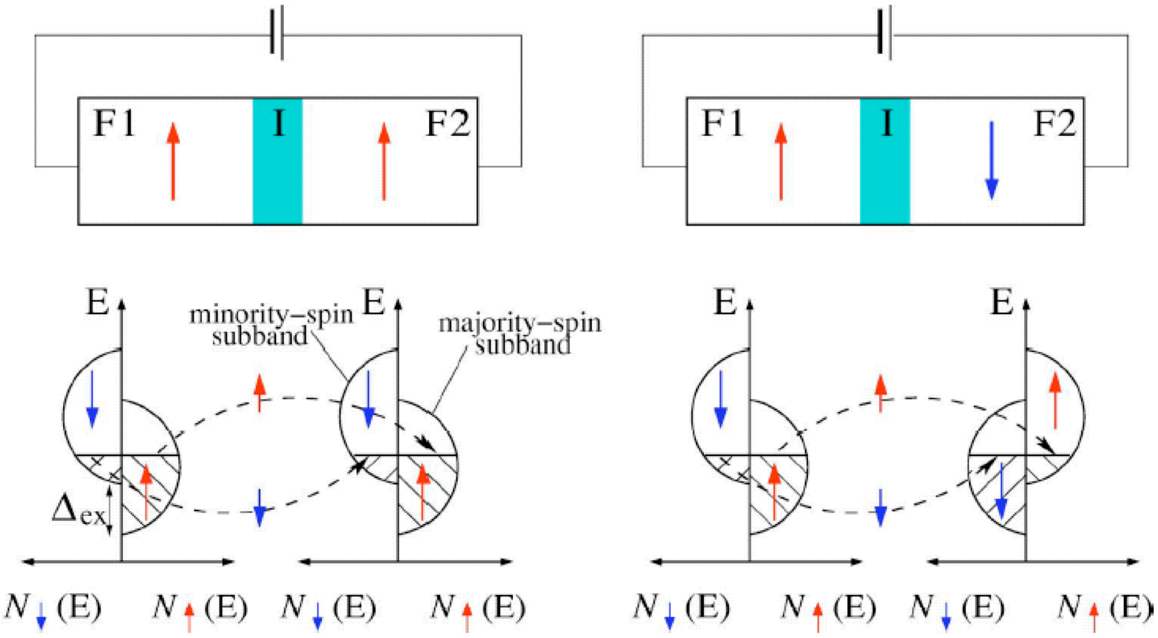

Fig. 2.9: *Schematic illustration of spin-dependent tunneling across an insulating barrier.*

In deriving the above equation, we have assumed that spin is conserved during tunneling, which is always true in the ideal case. The *junction magnetoresistance ratio* (JMR) is defined as:

$$\mathrm{JMR} = \frac{1/G_{AP} - 1/G_P}{1/G_{AP}} \tag{2.2.12}$$

which can be further reduced to:

$$\mathrm{JMR} = \frac{2P_1P_2}{1+P_1P_2} \tag{2.2.13}$$

with P polarization as defined in Sec. 1.2.

This is the result that has been predicted by the Jullière model [25]. Notice that an alternative definition frequently used in the literature and called *tunnel magnetoresistance ratio* (TMR) is:

$$\mathrm{TMR} = \frac{1/G_{AP} - 1/G_P}{1/G_P} = \frac{2P_1P_2}{1-P_1P_2} \tag{2.2.14}$$

Obviously, the TMR is always larger than the JMR, although the actual size of the effect is the same.

2.3 Domain wall magnetoresistivity (DWMR)

Domain wall magnetoresistivity (DWMR) is a mesomagnetic effect whose origin can be tackled by considering the geometrical similarity between a GMR structure and a domain wall, as illustrated in Fig. 2.10. In both cases, regions of different magnetization are separated by an intermediate layer. In the former case, this layer is in the form of a thin film of non-magnetic metal whereas in the latter it is a region of twisted magnetization.

The GMR functions provided that spin conservation occurs across the intermediate zone. By analogy, it is possible to develop a model of domain wall resistance in which the value of the resistance is determined by the degree of spin depolarization of the charge carriers in the twisted magnetic structure formed at the heart of the domain wall. The model, proposed by Viret et al. [26,27] assumes that an electron moves through a domain wall by precessing about an axis, which is tilted at a fixed angle to the local magnetization direction in the wall. They used this "spin mistracking" picture as the basis of a phenomenological model of diffusive transport through a domain wall, in which spin follows adiabatically the magnetization in the wall but the mistracking causes electrons to experience a weighted combination of the spin up and down resistivities of a uniformly magnetized ferromagnet. This mistracking of, say, an up spin leads to its making an average angle:

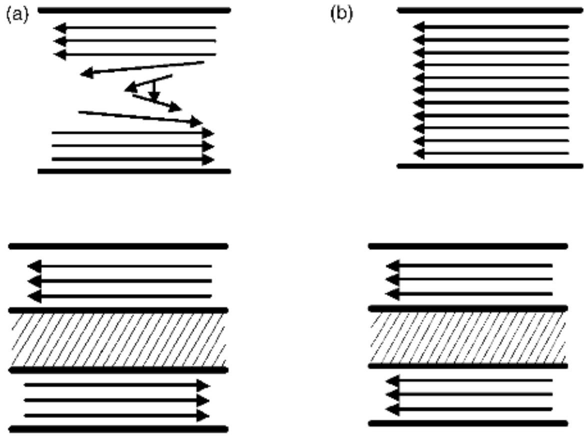

Fig. 2.10: *Geometrical similarities between (a) a DW and (b) a GMR trilayer. After [26].*

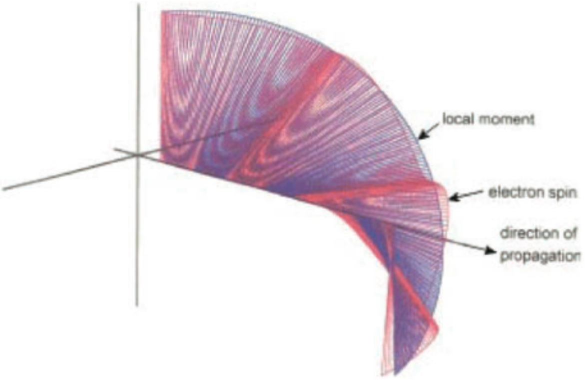

Fig. 2.11: *Spin orientation versus trajectory for the electrical carriers in transit through a domain wall in Co. The blue vector represents the cobalt magnetization and the red vector represents the spin orientation. Taken from [26].*

$$\theta = \frac{hk_F v_f}{E_{ex} w} \tag{2.3.1}$$

with the local magnetization direction in the domain wall, where h is the Planck constant, v_F the Fermi velocity, E_{ex} is the exchange length, w domain wall thickness and k_F is the Fermi wavevector. This is equivalent to its wave function being contaminated by a fraction sin(θ/2) of the down-spin wave function (Fig. 2.11). The up spin is then susceptible to additional scattering by an amount equivalent to $\left\langle \sin^2(\theta/2) \right\rangle$ multiplied by the down-spin scattering rate. This model leads to a formula for the spin-dependent contribution to the domain wall resistivity:

$$\frac{\Delta\rho_W}{\rho_0} = \left(\frac{\lambda^*}{\lambda} + \frac{\lambda}{\lambda^*} - 2 \right) \left\langle \sin^2\left(\frac{\theta}{2}\right) \right\rangle \tag{2.3.2}$$

where λ and λ^* are the majority and minority spin mean free paths, ρ_0 and $\Delta\rho_W$ are, respectively, the bulk F resistivity and the resistivity increase due to domain wall contribution. Notice from eqs. (2.3.1) and (2.3.2) that the magnetoresistive contribution falls rapidly while increasing the wall thickness w. For bulk wall thicknesses (several tens of nanometers) this contribution is not detectable (or at least very small).

This model has been re-analyzed [28] by replacing this simple rotating frame approach with a more sophisticated quantum mechanical analysis: to within a simple numerical factor, identical results are obtained.

When the domain wall thickness becomes smaller than the mean free path (ballistic regime) the abrupt wall becomes a spin-dependent potential step [29]. The system is more similar to the case of a GMR system, or, in the limit of complete non-adiabaticity, to a MTJ system, consequently the MR ratio is significatevely increased. In this case the DWMR is often called ballistic magnetoresistance (BMR) and has been invoked to explain the huge MR ratio detected in magnetic point contact systems [30]. Yet, the effective observation of this regime in point contacts is still under debate and not of interest for the present work.

2.4 Magnetoelectronic devices

2.4.1 AMR magnetic field sensors

The immediate application of the AMR was in magnetic recording as read head in hard disks because sensors based on the AMR effect offer higher output as compared to the thin-film inductive head [31,32]. Although, for Ni (Fe, Co) alloys, the largest AMR effect so far was found for $Ni_{70}Co_{30}$, 26.7% at 4.2 *K* and 6.6% at 300 *K* [31], the material of choice for magnetic recording applications is $Ni_{80}Fe_{20}$ Permalloy (Py) because of its softness (low coercivity), high permeability, and low magnetorestriction. The typical AMR ratio for thin Py films (30–50 nm) is about 2%, although the AMR of its bulk counterpart can be as high as 4% [33]. Fig. 2.12 shows a schematic drawing of an AMR sensor element. We assume that the external magnetic field points in the *y*-axis direction. Assuming that the entire element is a single-domain particle with a uniaxial anisotropy (SW approximation), the magnetization direction is given by eq. 1.4.42:

$$\sin\theta = \frac{H}{2K/\mu_0 M_S} \tag{2.4.1}$$

If the magnetocrystalline anisotropy and the shape anisotropy are distinguished in the constant *K,* eq. (2.4.1) can be rewritten as:

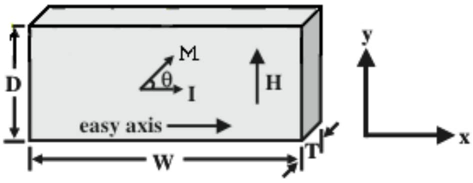

Fig. 2.12: *Schematic of a single domain AMR sensor.*

$$\sin\theta = \frac{H}{2K_{mc}/\mu_0 M_S + H_d} = \frac{H}{H_K + H_d} \tag{2.4.2}$$

with H_d demagnetizing field along the y-axis.

Substituting eq. (2.4.2) in eq. (2.1.3) yields:

$$\rho(H) = \rho_{//} + \rho_{\perp}\left(\frac{H}{H_K + H_d}\right)^2 \tag{2.4.3}$$

For soft materials ($H_K << 1$):

$$\rho(H) = \rho_{//} + \rho_{\perp}\left(\frac{H}{H_d}\right)^2 \tag{2.4.4}$$

It is apparent from the above equation that the simple AMR sensor element exhibits a nonlinear response to the external field, which cannot be used as a read sensor for magnetic recording as it is. However, it is not difficult to realize from eq. (2.4.4) that the sensor can be made linear if an additional field, which is much larger than that of the external field, is added to it to make the total effective external field as $H' = H + H_B$ with $H_B >> H$. In the case of $H_d << H$, which is true for magnetic recording, eq. (2.4.4) becomes :

$$\rho(H) = \rho_{//} + \rho_{\perp}\left(\frac{H_B}{H_d}\right)^2 - \rho_{\perp}\frac{2HH_B}{H_d^2} \tag{2.4.5}$$

It shows that now the sensor responds linearly to the external field. H_B is the so-called *bias field* or, more precisely, the *traverse bias field* because it is perpendicular to the easy axis direction of the sensor element. In actual sensor design, the strength of the bias field is chosen such that the magnetization direction at zero field is about 45° away from the easy axis so as to maximize the sensitivity. It is obvious from eq. (2.4.5) that the smaller the demagnetizing field, the larger the sensitivity.

There are many different ways to form a traverse bias. Among them, the most successful is the *soft adjacent layer (SAL) bias scheme*, in which a soft ferromagnetic layer is laminated with the sensing layer via a thin insulating spacer, as shown schematically in Fig. 2.13 [34].

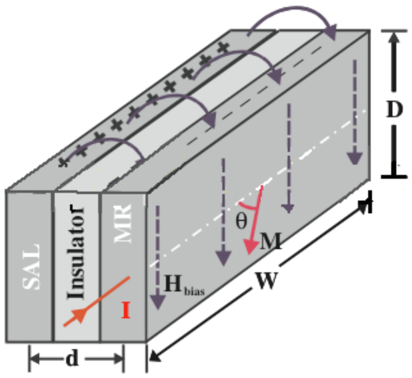

Fig. 2.13: *Schematic of an AMR sensor using an SAL bias. The sensor consists of an MR element as the active layer and a soft adjacent layer (SAL) for traverse bias. The MR element and the SAL are separated by an insulating spacer.*

As the SAL is normally chosen such that most of the current flows through the sensing layer, the magnetic field induced by the sensing current magnetizes and saturates the SAL into one direction (pointing upward in Fig. 2.13). The fringe field thus generated, in turn, provides a traverse bias to the sensing layer itself. The SAL scheme offers several advantages, such as adjustable bias field, relatively uniform bias field distribution, and reduced demagnetizing field. Although it also has drawbacks such as the current shunting effect, it so far has remained the most successful engineering design. In actual sensors, in addition to the traverse bias, one also needs a longitudinal bias to stabilize the domain structure so as to reduce the Barkhausen noise caused by the domain-wall motion [34].

As we mentioned above, the AMR sensor, intrinsically, is not a linear sensor. In addition to the nonlinearity issue, it also suffers drawbacks such as thermal asperity [35] (that is the large voltage generated at the output of the read head pre-amplifier when the read head occasionally comes into contact with the disk) and side reading asymmetry [36]. Perhaps the most fatal shortcoming of the AMR sensor is that it is difficult to scale it down in thickness so as to meet the requirement of shrinkage in bit length. These intrinsic characteristics of the AMR plus the tremendous progress made in GMR in the early 1990s have determined the short lifetime of the AMR sensor in the history of hard disk drives. It was gradually replaced by the spin-valve sensor, which was first introduced into disk drives by IBM in 1997.

2.4.2 GMR magnetic field sensors: the spin-valve

The research on read sensors using the GMR effect commenced soon after the GMR effect was reported. This was mainly because it gives a much higher MR ratio as compared to its AMR counterpart. However, the original GMR structure consisting of Fe/Cr, Co/Cu, or other types of magnetic multilayers could not be applied to read sensors in the original form

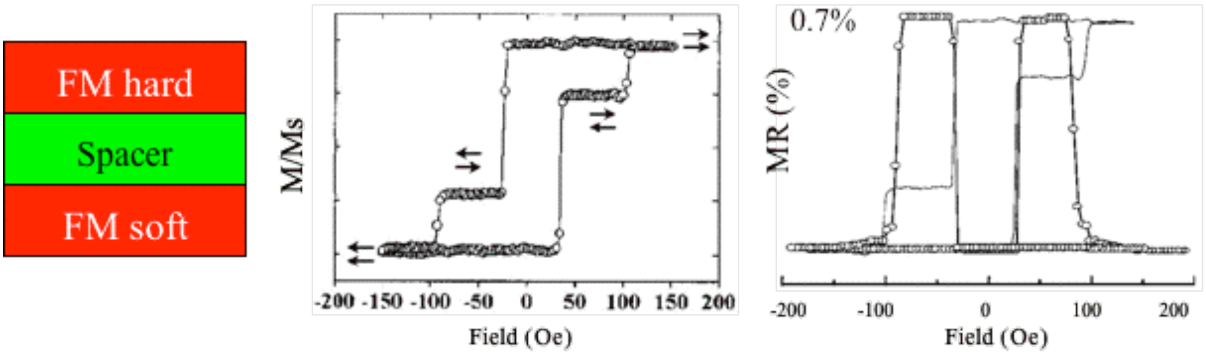

Fig. 2.14: *Magnetic and transport behaviour of typical pseudo-spin valve structures.*

because of their large saturation fields, and also the nonlinear response near the zero-field point. The most straightforward way to reduce the saturation field is to reduce the exchange coupling between the ferromagnetic layers through increasing the thickness of the spacer. However, a completely decoupled or weakly coupled multilayer structure does not function properly as a sensor because of the possible inconsistent movement of all of the magnetic layers under an external field. One of the possible ways to overcome the drawback of the decoupled GMR stack is to use two decoupled layers with one of them much softer than the other, so that the former will respond to a small field, while the latter will only change its magnetic state when it is subjected to a large field. This kind of structure, called *pseudo-spin-valve* can, in principle, form a good sensor. Different coercive fields can be achieved by using two different materials, for instance NiFe/Cu/Co trilayer, or the same material but reducing the coercivity of one of the layers by reducing its thickness [37], for instance Co/Cu/Co systems. If the soft layer has a very small coercivity, the MR(H) characteristic (Fig. 2.14) shows narrow hysteresis and the device can be used as a sensor in the range of field determined by the coercivity of the hard layer. The device can be also used for digital data storage applications (see Sec. 2.4.3). Although a relatively large magnetoresistance with a small saturation field has been obtained in these kinds of structures, they are not much reliable because of the impossibility to have hard layers with very large coercivity, and hence prevent the accidental switching of this layer. However, this type of structure is a good object for studying spin-dependent transport in magnetic/nonmagnetic multilayers.

The magnetic stiffness of the hard layer can be improved by using the *exchange bias (EB) effect* [38,39]. The EB effect occurs in ferromagnet/antiferromagnet (F/AF) systems and consists in an increased of the coercivity and in a shift of the hysteresis loop from the zero field axis, in a direction opposite to that of the cooling field, after the sample is heated up to above the Néel temperature.

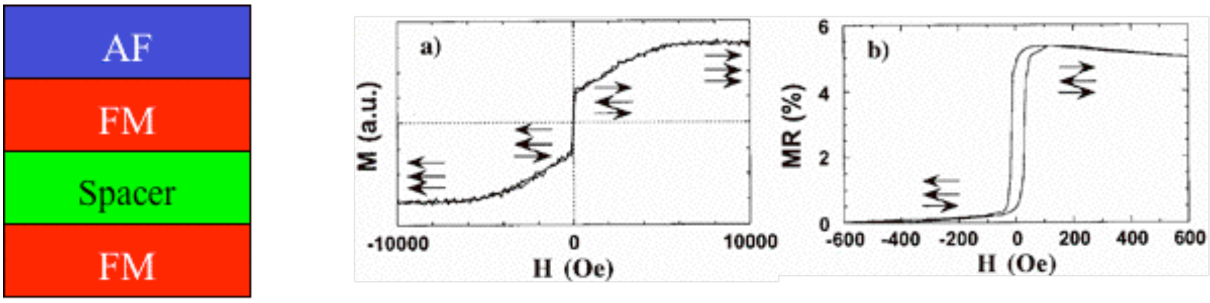

Fig. 2.15: *Magnetic and transport behaviour of typical conventional-spin valve structures.*

The magnetization of the F-layers that is in direct contact with the AF-layer is "pinned" by the latter, and thus this F-layer is commonly called the *pinned layer*. On the other hand, the magnetization of the other F-layer is free to rotate to respond to an external field, and thus it is called the *free layer*. In case common AF materials (such as FeMn or IrMn) are used for the pinning, the structure is called *conventional spin-valve*. If interlayer AF exchange coupled multilayers (such as Fr/Cr or Co/Cu) are used for the pinning the structure is called *synthetic spin-valve*. Typical $M(H)$ and MR(H) loops are shown in Fig. 2.15.

It must be noted that, in order to have sharp $M(H)$ loops, and hence high sensitivity, the spacer thickness has to be chosen such that there is not exchange coupling between the soft and hard layers. Unfortunately, the exchange coupling is not the only origin of possible coupling between these layers. Pinholes in the spacer can smooth the hysteresis loop because of localized direct coupling. Another important source of coupling is the so-called *magnetostatic "orange peel"* coupling, which rises from the generation of magnetic dipoles due to the films roughness (Fig. 2.16). With the device approaching sub-micron size, stray field from the F-layers can be another magnetostatic source of coupling. Of course, increasing the spacer thickness can reduce all these effects, but this is paid with a reduction of the MR ratio.

Another source of reduction of MR can be the presence of thick magnetic "dead layers" at the F/N or F/I interfaces. Consider whatever magnetic film. At whatever magnetic/non-magnetic interface, the atoms of the F-layer cannot exchange energy at one side. In other

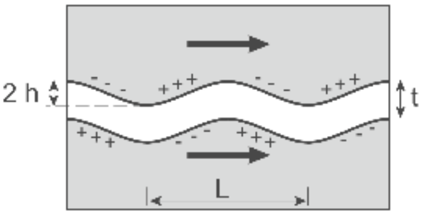

Fig. 2.16: *Ferromagnetic coupling of magnetic layers due to formation of magnetic dipoles at rough interfaces.*

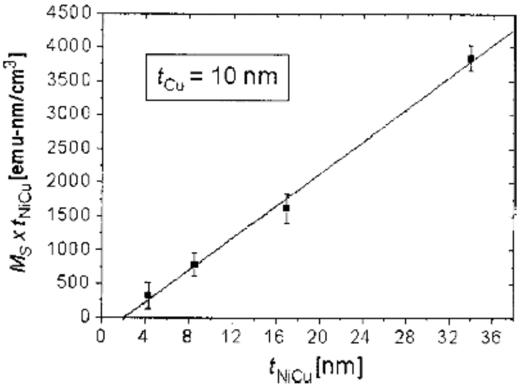

Fig. 2.17: *Estimation of the dead layer thickness at T = 30 K in NiCu/Cu multilayers. From Ruotolo et al. [40].*

words, for these atoms the exchange integral J_{ex} is smaller. This forms a layer at the interface where J_{ex} is much smaller than it is in the inner atomic layers. At a certain temperature, this layer can be magnetically inactive, i.e. magnetically "dead". The effect usually extends over an atomic single cell length. Thus, in metal it is of the order of 1-2 Å and can be neglected. In more complex materials like manganites it can be of several nm. The thickness of the dead layer can be roughly estimated by macroscopic measurements. If one measures the saturation magnetization (M_S) for magnetic films with different thickness, it is generally observed that M_S follows the relation:

$$M_S = M_0\left(1 - \frac{2\delta}{t}\right) \tag{2.4.6}$$

with M_0 saturation magnetization of the bulk material, t and δ film and dead layer thickness, respectively. By plotting M_S in a M_St vs t representation (see Fig. 2.17) one can estimate the value of δ. Notice that in eq. (2.4.6) it is assumed that the thickness of dead layers at the top and bottom interface/surface of the film is the same, which could not be true, i.e. δ is an average dead layer.

2.4.3 TMR magnetic field sensors

Magnetic tunnel junctions can be used either as read sensors in hard disk drives or as memory cells in MRAMs (see Sec. 2.4.4). Following are some advantages and drawbacks of MTJs compared to spin valves when they are used as read sensors.

For an MTJ sensor element with width W, height H, and thickness T, the maximum output voltage is given by:

$$\Delta V_{MTJ} = \frac{I\Delta RA}{WH} = J\Delta RA \tag{2.4.7}$$

where J is the current density, and ΔRA is the change in resistance–area product of the MTJ. The maximum output voltage refers to the value that is obtained when the magnetizations of the two F-layers are switched from a parallel alignment to an antiparallel alignment or vice versa. The actual output is normally a fraction of this due to the limited dynamic range of the read sensor and the head efficiency factor. In practice, however, the output is limited by the characteristic dependence of JMR on the dc bias voltage, that is:

$$\Delta V_{MTJ}(V) = V_B \mathrm{MR}_0 (V_{\max} - V_B)/V_{\max} \tag{2.4.8}$$

where V_B is the bias voltage, MR_0 is the MR ratio at zero bias, and V_{max} is the voltage at which the MR becomes zero. In deriving the above equation, we have considered that the MR ratio decreases with the bias voltage. Although the mechanism is still not fully understood, it is believed that it is caused by both the bias-induced change in the barrier profile and the energy-dependent density of states for both the majority and minority electrons [41]. Magnon excitation in the magnetic layer might also be one of the possible reasons [42]. As a first approximation we have considered the decreasing linear with bias voltage in eq. (2.4.8).

The maximum output signal is thus given by:

$$\Delta V_{MTJ}(V_B = V_{\max}/2) = \frac{1}{2} V_{\max} \mathrm{MR}_0 . \tag{2.4.9}$$

Assume that MR_0 = 5–10% at device level, and V_{max} = 800 mV; it gives an output voltage of 20 – 40 mV. On the other hand, the maximum output signal of a CIP spin valve is of a few tens of mV. We can see that the maximum output signal of an MTJ is much higher than that of a typical spin valve. Moreover, the output of the spin valve scales with its width. Therefore, the MTJ head becomes more advantageous than the spin-valve head in terms of output signal when the track width shrinks into the submicron regime, which is already the case in the latest products.

The primary drawback of MTJ is its large junction resistance, in particular, when its size shrinks. The large junction resistance will result in both a small bandwidth and a low signal-to-noise (SNR) ratio of the read signal. For high-frequency operations, the sensor resistance is required to be less than 100Ω. This makes the MTJ not suitable for read heads at an areal density of more than 200 Gbits/in^2. MTJ are instead the best candidates for magnetic data storage.

2.4.4 Magnetic data storage

Magnetic random access memories (MRAMs) are memories based on magnetoresistive devices that have the advantage of being non volatile, which is a typical characteristic of read-only-memories (ROMs) and sequential memories (FLASH), while keeping the random access work mode at potentially the same work frequency of the widely-used semiconductor-based dynamic RAM (DRAM).

Fig. 2.17 shows a schematic of an MRAM design using MTJs. The memory cells are formed at the cross junctions of the bit and word lines. A peripheral circuitry pilots the bit and word lines.

The signal readout is based on the spin-dependent tunneling resistance of the MTJ by supplying a small sensing current to a specific cell. As the sensing current is only used to detect the relative orientation of the magnetization of the two magnetic layers instead of being used to switch the magnetization, it can be kept at a relatively low level. The write operation relies on the oersted field generated by making currents pass on the word and the bit lines. Assume amplitudes h_b and h_w for the reduced oersted field produced by the currents on the bit

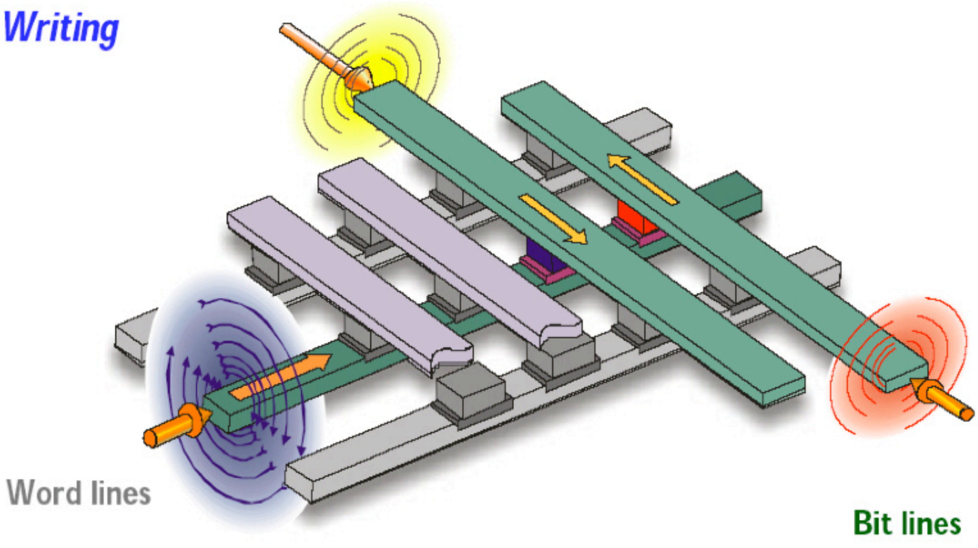

Fig. 2.18: *Schematic picture of an MRAM in writing operation.*

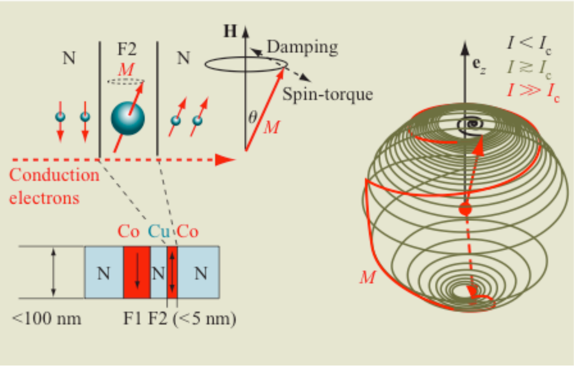

Fig. 2.19: *Illustration of spin-transfer and associated macro-spin dynamics. A uniaxial anisotropy is assumed to exist with its easy axis. After [45].*

and word line, respectively. They act like the $h_\perp$ *and* $h_{//}$ of the SW model (Sec. 1.4.7). The currents on the lines are calibrated such as (h_b, h_w) falls outside the SW asteroid (switching occurs), while (h_b, 0) and (0, h_w) fall inside so not to produce switching. Things are more complicated since the single domain approximation is not valid. With such a writing operation, nearest neighbor cells must be put as far as not to produce accidental writing (*cross talk error*). For this reason, current commercial MRAMs are strongly limited in density.

A proposed way to overcome this problem is using *current-induced magnetization switching* of the free layer through the so-called *spin-transfer torque effect*.

2.4.4.1 Spin transfer torque

The spin-transfer-induced magnetization reversal is a relatively new phenomenon, and it is unambiguously observable only in magnetic structures smaller than ~ 0.1 µm in size [43,44]. The phenomenon originates from the exchange of angular momentum between a spin-polarized current and the magnetization. A sketch for the basic concept of spin-transfer and its related macro-spin dynamics is shown in Fig. 2.18. At the lower left in the figure is a two-ferromagnet layered spin-valve structure. The current passes through the left ferromagnet (F1) and becomes spin-polarized. When it passes through the second, thinner ferromagnet on the right (F2), the polarization direction of the current may have to change depending on the relative orientation of F2 and F1. This is illustrated at the upper left in the figure, where N designates a nonmagnetic conductor. In the process, some of the angular momentum from the electron spins is absorbed by the ferromagnet, resulting in the exertion of a net torque (spin-torque) on the ferromagnet.

This ‘‘repolarization’’ process is what causes the second ferromagnet to experience an effective torque [46]. This spin-current-induced torque for the relative orientations illustrated here, is in a direction that opposes the magnetic damping torque for F2, as shown in the figure. For a large enough current, the spin-torque overcomes magnetic damping. This causes an instability to develop, and the precession cone angle increases over time. When the cone angle increases past the equator, both the damping torque and the spin-torque point toward the south pole, which becomes a stable point for F2, thus completing the magnetic reversal, as depicted at the right in the figure. The situation for reversed current direction is a bit more complex, but the net spin-torque on F2 remains proportional to the current. The reversal process remains essentially the same as the one described above [47].

For a nanomagnet macro-spin within which the magnetization is uniform, the transverse component of the spin-torque is [46]:

$$\begin{aligned} \boldsymbol{\Gamma} &= -g\left(\mathbf{M},\hat{\mathbf{M}}_P\right)\frac{a_J}{M_S}\mathbf{M}\times(\mathbf{M}\times\hat{\mathbf{M}}_P) \\ a_J &= \frac{JPg\mu_B}{2e} \cong \frac{JP\mu_B}{e} \end{aligned} \tag{2.4.10}$$

where J is the current density, $\mathbf{M}$ is the magnetization of the free layer, $\hat{\mathbf{M}}_P$ is the unit vector along the direction of the magnetization of the pinned layer**,** i.e. the direction of spin-polarization of the incoming current, and M_S is the saturation magnetization. The term $g(\mathbf{M}, \hat{\mathbf{M}}_P)$ is a numerical prefactor that describes the angular dependence of the efficiency of spin-angular momentum transfer, originating from the quantum-mechanical nature of the interaction between spin-polarized current and the macro-spin; it may also depend on the global spin-current and the boundary condition of the spin-density. The case of a constant $g(\mathbf{M}, \hat{\mathbf{M}}_P) = 1$ within the macrospin-based phenomenological model describes a simple redirection of the spin-current polarization direction and complete absorption of its transverse angular momentum by the macrospin. In reality, the detailed angular dependence of $g(\mathbf{M}, \hat{\mathbf{M}}_P)$ is model-dependent and is never an angle-independent quantity. Its macroscopic form in real materials systems has yet to be firmly established experimentally. For simplicity of discussion on a semi-quantitative level, however, for now we assume a constant $g(\mathbf{M}, \hat{\mathbf{M}}_P)$, and use Equation (2.4.10) as the basic interaction that enters the magneto-dynamics equation for the motion of the macro-spin.

The spin torque term can be taken into account by rewriting the LLG equation (1.4.26) as:

$$\frac{d\mathbf{m}}{dt} = -\gamma'\left(\mathbf{m}\times\mathbf{H}_{eff}\right) - \alpha'\mathbf{m}\times\left[\mathbf{m}\times\left(\mathbf{H}_{eff} + \frac{JP\mu_B}{e\alpha'}\hat{\mathbf{m}}_p\right)\right]. \qquad (2.4.11)$$

For simple geometries and under a macro-spin approximation, eq. (2.4.11) can be linearized and solved for its stability boundary. For a thin free-layer nanomagnet in a collinear geometry with the easy axis of its uniaxial anisotropy field aligned with that of the applied field and the easy-plane anisotropy sharing its easy plane with the film plane, a stability threshold current I_{cr} of:

$$I_{cr} = \left(\frac{e}{\mu_B}\right)\left(\frac{\alpha'}{P}\right)abtM_S\left(H_a + H_{an} + \frac{1}{2}M_S\right) \qquad (2.4.12)$$

where $abtM_S$ is the total magnetic moment of the free layer with a, b lateral dimension and t thickness.

Eq. (2.4.12) gives a current threshold above which the linearized LLG equation becomes unstable over time, and a net gain of the precession cone-angle results. In comparing with experimental results, however, effects of large cone-angle precession must often be carefully taken into account, since the development of an initial cone-angle increase dictated by the linear stability threshold may not necessarily lead to complete magnetic reversal.

There is another mechanism that can cause interaction between a magnetic moment and a current: current-induced magnetic field (the oersted field). A current-induced magnetic field for a wire of radius r can be related to the maximum field (usually around the surface of the wire) and the current passing through the wire I. From Maxwell's equations, the relation is $I = 2\pi rH$. A spin-valve of similar lateral size ($2r$) would have a spin-torque threshold current [following Eq. (2.4.12)] of the order of $I_{cr} = (e/\mu_B)(\alpha'/P)(4r^2tM_S)[H_a + H_{an} + (1/2)M_S]$. The spin-torque threshold is proportional to r^2, and the oersted-field-related current (for a given threshold field such as the anisotropy field H_{an}) is proportional to r. Thus, at large dimensions the threshold from the oersted field is the lower threshold. The crossover point for high-moment thin films such as cobalt, with $H_a = 0$ and $H_{an} \ll \frac{1}{2}M_S$ gives, for reasonable experimental values of $3d$ transition metals, $2r_c \approx 0.1$ µm, below which the spin-torque effect is more significant. This explains why spin-torque is observed only in submicron-size systems. Notice that using half-metals ($P = 1$) can either reduce the critical current (keeping constant the size) or increase the minimum lateral size (for the same critical current).

Unfortunately, although magnetization switching based on spin transfer has been studied extensively, the current that is needed to switch the magnetization is still comparable to the write current of existing MRAMs. Novel approaches are being considered to improve the density of MRAMs, among which the use of system based on DWMR and DW motion. One of the main goals of the present work is to investigate such new approaches.

2.4.5 Domain-wall based devices

We have already seen how a DW can give a resistive contribution that rapidly increases with the reduction of the DW width. The other ingredients to make this magnetoresistive effect suitable for practical application is, on one side, the possibility to change the DW width, and hence the DWMR, for sensing applications, and, on the other side, to displace a DW and hence switch the state of the device, for digital applications.

When a DW is constrained, either by a geometrical constrain or because it has to pass from a region with low coercivity to a region with high coercivity (see Fig.2.20a) a simple micromagnetic simulation based on the LLG equation is needed to understand that, when a magnetic field H_a is applied in the film plane so that to exert a force on the wall, for values of H_a smaller than a certain H_{cr}, it is more energetically favourable for the system to reduce the DW width, rather than displace it [48]. On the contrary, when H_a reaches H_{cr}, the wall is displaced.

In the range $0 < H_a < H_{cr}$, the resistance changes as a function of the field, and the system works as a field sensor (Fig.19b), although a circuitry is needed to linearize the output.

The force on the wall can be exerted by a current, instead of by an external applied magnetic field. The theoretical description of *current-induced domain wall motion*, or in other words, the interaction of spin polarized charge carriers with the magnetization of the material,

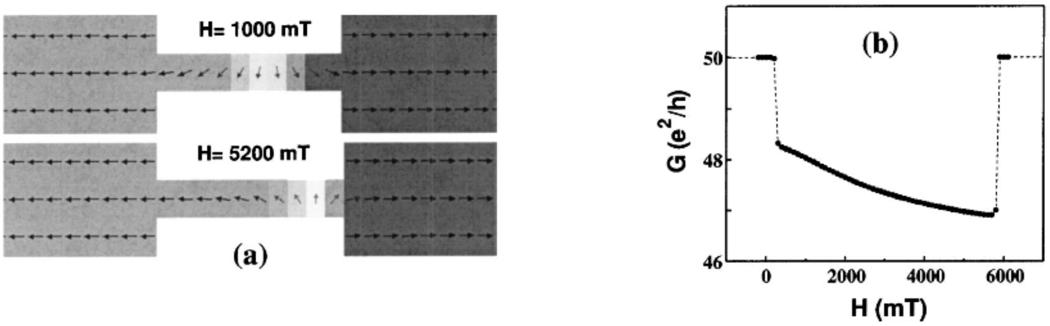

Fig. 2.20: *(a) LLG micromagnetic simulation for a DW in a nano-channel comprised between two region with different coercivity (dark grey correspond to the region with higher coercivity); (b) conductance vs. applied field detected on the connecting arms. Taken from [48].*

is a complicated issue which is still the subject of much debate. We will briefly describe the phenomenon here in the framework of the spin transfer torque model starting from the Landau-Lifshitz-Gilbert equation.

Considering the geometrical similarity between a GMR structure and a domain wall, as described in Sec. 2.3, the spin transfer of a polarized current on a DW can be simply phenomenologically introduced adding an additional term in the LLG, similar to the form in eq. (2.4.10):

$$\frac{d\mathbf{m}}{dt} = -\gamma'\left(\mathbf{m}\times\mathbf{H}_{eff}\right) - \alpha'\mathbf{m}\times\left[\mathbf{m}\times\left(\mathbf{H}_{eff} + b\hat{\mathbf{m}}_p\right)\right] \tag{2.4.13}$$

where b must be a constant depending on current intensity and current polarization. In case of a DW in a film, we cannot distinguish between free and pinned layers. The "pinned layer" is just the same layer in which the magnetization changes. It is more appropriate to consider the same magnetization vector **m** and its variation in the space. Eq. (2.4.10) can be rewritten as suggested by Li and Zhang [49]:

$$\tau = -\frac{1}{M_S^2}\mathbf{M}\times\left[\mathbf{M}\times\left(\mathbf{u}\cdot\nabla\right)\mathbf{M}\right] \tag{2.4.14}$$

where

$$\mathbf{u} = \frac{gP\mu_B}{2eM_S}\mathbf{J} \tag{2.4.15}$$

is a velocity vector whose amplitude is a_J/M_S (see eq. (2.4.10)) and direction the current direction.

If the torque of eq. (2.4.14) is integrated across a multilayer, assuming the free and the pinned layer being in single domain states, eq. (2.4.14) turns out to be equivalent to eq. (2.4.10). In other words, the torque term of eq. (2.4.10) can be regarded as the continuous limit of eq. (2.4.14). However, the velocity u depends on the spin polarization P of the bulk material, while in the multilayer situation the interfaces are important (and here neglected by considering $g(\mathbf{M}, \hat{\mathbf{M}}_P) = 1$). Therefore a direct relation between u and a is not obvious. Anyway, Li and Zhang [49] have shown that the spin transfer torque on a domain wall has many features in common with that at an interface with the ratio between eqs. (2.4.10) and (2.4.14) being given by the ratio t_F/w of the thickness of the ferromagnetic layer to the width of the domain wall, i.e. the torque is proportional to the volume of the material that experiences spin transfer effects.

Using the form of the LLG given by eq. (1.4.23) and adding the additional spin transfer term, we can write the modified LLG, in case of current flowing in the x direction, as:

$$\frac{\partial \mathbf{m}}{\partial t} = -\gamma_0 \mathbf{m} \times \mathbf{H}_{eff} + \alpha \mathbf{m} \times \frac{\partial \mathbf{m}}{\partial t} - u \mathbf{m} \times \left(\mathbf{m} \times \frac{\partial \mathbf{m}}{\partial x} \right) \tag{2.4.16}$$

where the last term is the *torque term in the adiabatic limit.*

By implementing the modified LLG equation into micromagnetic code and applying the code to a 5 nm thick and 100 nm wide wire with a domain wall in the center, Li and Zhang found that the wall is moved by a current with initial velocity $u/(1+\alpha^2)$, but stops on a nanosecond timescale after a displacement in the sub-micron range. This is in disagreement with experiments, which show that the wall keeps moving on a long distance.

They went on to publish a second paper where they discuss the differences between adiabatic and non-adiabatic torques [50]. The calculation was based on a very simple *s-d* Hamiltonian, $H_{sd} = -J_{ex}\, \mathbf{s} \cdot \mathbf{S}$ where **s** and **S** are the dimensionless spins of itinerant and local electrons and J_{ex} is the exchange integral between them. This exchange integral was used to define an exchange time $\tau_{ex} = \hbar / S J_{ex}$ then compared to the spin-flip lifetime in the dimensionless parameter $\xi = \tau_{ex} / \tau_{sf}$.

Four torques were then found, two arising from temporal variations in the magnetization, and two arising from spatial variations. Those arising from the time variations have no effect other than to renormalize the gyromagnetic ratio and the Gilbert damping parameter in the LLG equation. The other two appear in the modified form of this equation:

$$\frac{\partial \mathbf{m}}{\partial t} = -\gamma_0 \mathbf{m} \times \mathbf{H}_{eff} + \alpha \mathbf{m} \times \frac{\partial \mathbf{m}}{\partial t} - b_J \mathbf{m} \times \left(\mathbf{m} \times \frac{\partial \mathbf{m}}{\partial x} \right) - c_J \mathbf{m} \times \frac{\partial \mathbf{m}}{\partial x} \tag{2.4.17}$$

where $b_J = u/(1+\xi^2)$ and $c_J = u\xi/(1+\xi^2)$. Again, these quantities have dimensions of velocity. The term in b_J is very similar to that in the previous paper and describes adiabatic processes. On the other hand, the term in c_J was new, and is related to spin-mistracking of the conduction electrons.

The new non-adiabatic term, although very small ($c_J/b_J = \xi \sim 0.01$), is actually of great importance as it provides a mechanism for distorting the wall, and although all the adiabatic torque is eventually absorbed after wall deformation, the non-adiabatic part is not. It allows the wall to continue moving; the b_J term gives rise to a large initial velocity, as discussed above, but the c_J term controls the terminal velocity of the wall motion, which is no longer zero in zero field. The theory of this new torque term resolves the experimental discrepancy.

Tatara and Kohno [51] have extended the theory of DW motion to the case of pinned DWs. In the case of adiabatic limit, the alternative way of looking at the problem (which is of particular use in this work) is the following. A current passing through the wall will exert a torque. If ϕ_0 is the angle between spins at the wall center and the easy plane, below a critical value the torque exerted on ϕ_0 by the electrons passing through the wall is balanced by the anisotropy and not efficient in dragging the wall, whether it is pinned or not. For the motion of the wall to occur a critical current density J_{cr} must be reached and the wall will move with velocity:

$$\langle \dot{X} \rangle \propto \sqrt{J^2 - J_{cr}^2} \qquad (2.4.18)$$

with X position of the wall and J_{cr} depending linearly on the transverse anisotropy ($J_{cr} \propto K_\perp$). For $J >> J_{\mathrm{cr}}$, $\dot{X} \propto J$ and hence not depending on $K_\perp$.

Introducing a parabolic pinning potential of depth V_0 and range ν, a second critical current $J_{cr} \propto V_0/\nu$ can be found. These expressions allow strong ($V_0 > \alpha K_\perp$) and weak ($V_0 < \alpha K_\perp$) pinning regimes to be defined, where is either the pinning potential or transverse anisotropy that controls the onset of wall motion. Since in general $\alpha << 1$, we would expect that it is $K_\perp$ that controls the onset of wall motion in most experimental cases of interest.

It should be noted that in thick films, other mechanisms could be responsible for DW motion. The most important are: transversal (perpendicular to the wall) component of the oersted field produced by the current passing through a wall and hydromagnetic drag force.

As far as the former is concerned, the oersted field produced by a current passing through a wall does not usually have a transverse component perpendicular to the wall. This is because wall plane and current direction are usually perpendicular, for instance in stripes or nanowires. Yet, in case of particular geometries, for instance in constrictions, this component could be not zero and must be considered to avoid misinterpretation of the data.

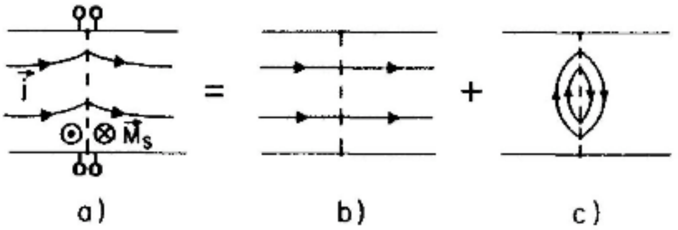

Fig. 2.21: *The non-uniform current distribution (a) in an uniaxial material with a wall can be decomposed into a uniform distribution (b) and an eddy current loop (c) around the wall. Taken from [52].*

The latter has been considered by Berger [52]. The basic principle is the following: the tilted magnetization in the wall region gives rise to a Hall effect. The current path is therefore modified as visualized in Fig. 2.21a and can be regarded as a superposition of the undisturbed current flow (Fig. 2.21b) with an eddy current around the domain wall (Fig. 2.21c). This eddy current causes magnetic fields that exert forces on the domain wall so that the wall is displaced in the direction of the charge carrier drift.

The force is proportional to the cross-section of the wall and therefore to the film thickness, and so this hydrodynamic drag effect will be generally a significant issue only for film thicknesses larger than approximately 100 nm. Furthermore, the model of Berger was developed with the view on Néel or Bloch walls (see Sec. 1.4.6) as present in bulk material of films. In 180° head-to-head (tail to tail) domain walls, an analogous geometrical argument as sketched in Fig. 2.21 for a Néel or Bloch wall shows that the hydromagnetic drag force is negligible in this geometry.

In the frame of this thesis, nanostructures are fabricated from thin film samples and 180° head-to-head (tail o tail) domain walls are observed. Thus the hydromagnetic drag force does not play any significant role here.

2.5 Superconducting spintronics

Consider a S/TMR/S structure in which S is a superconductor. Assume that the thickness and the total moment of the TMR are small enough to still allow overlapping of the two superconducting wavefunctions, i.e. a Josephson current is detectable.

Krivoruchko and Koshina [53] have demonstrated that, considering a S/F/I/F/S junction in hypoteses $d_S >> \xi_S$ and $d_F << \xi_F$ ($d_{S(F)}$ thickness of the S(F) layers, ξ_S superconducting coherence length and ξ_F length of the condensate penetration into the ferromagnet), the Josephson current is enhanced when the AP alignment is established while it is very strongly suppressed in case of P alignment. Most important, in case of P alignment, the Josephson current can become negative, providing a way to switch the device from the so-called “0-state” to the so-called “π-state”, i.e. a way to introduce a π-shift in the Josephson current phase.

The qualitative reasoning for this effect is that, in the AP case, the energy shift due to the exchange field is equal to the local superconducting gap (Δ) induced in the F. In this case, the peak in the local DOS is shifted to zero energy, (i.e. the Fermi level) giving a divergence of the critical Josephson current I_C at $T = 0$K This is analogous to the Riedel singularity of the a.c. Josephson supercurrent when $eV = 2\Delta$ [54]. In case of P alignment the π-phase transition is related to the rotation of π/2 of the wavefunctions at each S/F boundary, in addition to the jump of its modulus. A full understand of the effect cannot be achieved without a detailed analytical approach to the problem, which is indeed cumbersome. The reader is reminded to Ref. 53 for a detailed analysis.

The so-called π-junctions represent an important logic element in the development of solid state quantum computers. They can be realized in several ways, among which the exploitation of the d-wave nature of the cuprates [55] and the controllable properties of normal metal barriers with metallic superconducting electrodes [56]. The idea of realizing π-junctions with S/TMR/S structure, the so-called *spin-valve Josephson junctions*, is a rather new topic and part of the present work is devoted to investigate this possibility (see Sec. 5.3).

References

[1] W. Thomson, *Proc. R. Soc.* **8**, 546 (1857).

[2] R. I. Potter, *Phys. Rev. B* **10**, 4626 (1974).

[3] J. Kessler, *Polarized Electrons* (Springer, Berlin, Heidelberg, 1985).

[4] R. J. Elliot, *Phys. Rev.* **96**, 266(1954).

[5] M. I. D'yakonov and V. I. Perel', *Sov. Phys. JETP* **33**, 1053 (1971).

[6] G. L. Bir, A. G. Aronov and G. E. Pikus, *Sov. Phys. JETP* **42**, 705 (1976).

[7] R. von Helmholt, J. Singleton, D. A. Keen, R. McGreecy and K. Samwer, *Phys. Rev. Lett.* **71**, 2331 (1993).

[8] S. Jin, T. H. Tiefel, M. McCormack, R. A. Fastnach, R. Ramesh and L. H. Chien, *Science* **264**, 413 (1994).

[9] M. N. Baibich, J. M. Broto, A. Fert, F. Nguyen van Dau, F. Petroff, P. Etienne, G. Creuzet, A. Friederich, and J. Chazelas, *Phys. Rev. Lett.* **61**, 2472 (1988).

[10] R. Coehoorn, *Phys. Rev. B* **44**, 9331 (1991).

[11] Y. Yafet, *Phys. Rev. B* **36**, 3948 (1987).

[12] P. Bruno and C. Chappert, *Phys. Rev. B* **46**, 261 (1992).

[13] J. C. S. Kools, R. Coehoorn, W. Folkerts, M. C. DeNooijer and G. H. J. Somers, *Philips J. Res.* **51**, 125 (1998).

[14] N. F. Mott, *Adv. Phys.* **13**, 325-422 (1964).

[15] J. Mathon, *Spin Electronics* (M. Ziese and M. J. Thornton, Eds., Springer, Berlin, 2001).

[16] T. Valet and A. Fert, *Phys. Rev. B* **48**, 7099 (1993).

[17] A. Fert, J. Duvail, and T. Valet, *Phys. Rev. B* **52**, 65136521 (1995).

[18] R. E. Camley and J. Barnas, *Phys. Rev. Lett*. 63, 664 (1989).

[19] J. Barnas, A. Fuss, R. E. Camley, P. Grünberg, and W. Zinn, *Phys. Rev. B* **42**, 8110 (1990).

[20] S. Zhang and P. M. Levy, *J. Appl. Phys*. **69**, 4786 (1991).

[21] P. M. Levy, Solid State Phys. 47, 367 (1994).

[22] X. G. Zhang and W. H. Butler, *Phys. Rev. B* **51**, 10085 (1995).

[23] P. Zahn, I. Mertig, M. Richter, and H. Eschrig, *Phys. Rev. Lett.* **75**, 2996 (1995).

[24] R. Meservey and P. M. Tedrow, Phys. Rep. 238, 173 (1994).

[25] M. Jullière, *Phys. Lett.* **54A**, 225 (1975).

[26] J. F. Gregg, W. Allen, K. Ounadjela, M. Viret, M. Hehn, S. M. Thomson and J. M. D. Coey, *Phys. Rev. Lett.* **77**, 1580 (1996).

[27] M. Viret, D. Vignoles, D. Cole, J. M. D. Coey, W. Allen, D. S. Daniel and J. F. Gregg, *Phys. Rev. B* **53**, 8464 (1996).

[28] S. F. Zhang and P. M. Levy, *Phys. Rev. Lett.* **79**, 5110 (1997).

[29] A. Brataas, G. Tatara and G.E.W. Bauer, Phys. Rev. B, **60**, 3406 (1999).

[30] N. Garcìa, M. Munoz, G. G. Qian, H. Rohrer, I. G. Saveliev, and Y.-W. Zhao, *Appl. Phys. Lett.*, **79**, 4550 (2001) and references therein.

[31] T. R. McGuire and R. I. Potter, IEEE Trans. Magn. MAG **11**, 1018 (1975).

[32] R. Hunt, *IEEE Trans. Magn. MAG* **7**, 150 (1971).

[33] X. Wang and A. M. Taratorin, *Magnetic Information Storage Technology,* (Academic, New York, 1999).

[34] J. C. Mallinson, *Magneto-Resistive Heads: Fundamentals and Applications*, (Academic, New York, 1996).

[35] K. B. Klaassen and J.C.L. van Peppen, *IEEE Trans. Magn.* **33**, 2611 (1997).

[36] N. H. Yeh, *IEEE Trans. Magn. MAG* **18**, 1155 (1982).

[37] J. F. Loffler, J. P. Meier, B. Doudin, J. P. Ansermet, and W. Wagner, *Phys. Rev. B* **57**, 2915 (1998).

[38] J. Nogues and I. K. Schuller, *J. Magn. Magn. Mater.* **192**, 203 (1999).

[39] A. E. Berkowitz and K. Takano, *J. Magn. Magn. Mater.* **200**, 552 (1999).

[40] A. Ruotolo, C. Bell, C.W. Leung and M. G. Blamire, *J. Appl. Phys.* **96**, 512 (2004).

[41] G. G. Cabrera and N. García, *Appl. Phys. Lett.* **80**, 1782 (2002).

[42] S. Zhang, P. M. Levy, A. C. Marley, and S. S. P. Parkin, *Phys. Rev. Lett.* **79**, 3744 (1997).

[43] M. Tsoi, A. G. M. Jansen, J. Bass, W.-C. Chiang, M. Seck, V. Tsoi, and P. Wyder, *Phys. Rev. Lett.* **80**, 4281 (1998).

[44] J. Grollier, V. Cros, A. Hamzic, J. M. George, H. Jaffre`s, and A. Fert, *Appl. Phys. Lett.* **78**, 3663 (2001) and references therein.

[45] J.Z. Sun, *IBM J. Res. & Dev.*, **50**, 81 (2006).

[46] J. C. Slonczewski, *J. Magn. Magn. Mater.* **159**, L1 (1996).

[47] M. D. Stiles and A. Zangwill, *Phys. Rev. B* **66**, 014407 (2002).

[48] J. D. Burton, A. Kashyap, M. Ye. Zhuravlev, R. Skomski, E. Y. Tsymbal, and S. S. Jaswal, O. N. Mryasov and R. W. Chantrell, *Appl. Phys. Lett.*, **85**, 251 (2004).

[49] Z. Li and S. Zhang, *Phys. Rev. Lett.* **92**, 207203 (2004).

[50] S. Zhang and Z. Li, *Phys. Rev. Lett.* **93**, 127204 (2004).

[51] G. Tatara, H. Kohno, *Phys. Rev. Lett.* **92**, 086601 (2004).

[52] L. Berger, *J. Appl. Phys.* **49**, 2156 (1978).

[53] V. N. Krivoruchko and E.A. Koshina, *Phys. Rev. B*. **64**, 172511 (2001).

[54] E. Riedel, *Z. Naturforsch. A* **19**, 1634 (1964).

[55] C. C. Tsuei and J. R. Kirtley, *Rev. Mod. Phys.* **72**, 969 (2000).

[56] J. J. A. Baselmans, B. J. van Wees, and T. M. Klapwijk, *Phys. Rev. B* **65**, 224513 (2002).

Chapter 3

Deposition, characterization and micro-patterning of films and multilayers

The film deposition, lithography and milling used to form micron scale tracks is discussed, as well as the method of characterization of the films and multilayers in terms of structural, electrical and magnetic properties.

3.1 Film deposition

3.1.1 Substrate preparation

All films were deposited on (100) silicon substrates with a 250 nm oxidised surface layer, except for $La_{0.7}Sr_{0.3}MnO_3$ (LSMO) films, which were grown on Strontium Titanate ($SrTiO_3$). The dice were always 5 × 5 mm^2. The substrates were cleaned using ultrasounds in acetone and then isopropanol.

3.1.2 Sputter deposition

Sputtering uses plasma gas to bombard a target material to produce molecular or atomic fragments. These fragments are then collected on the substrate and the thin film is built up. The sputtered atoms undergo multiple collisions with the plasma gas before reaching the substrate. In this way the pressure of the sputtering gas allows control over the kinetic energy of the sputtered atoms reaching the substrate. This in turn controls the mobility and the resulting stresses in the film. The gas used to form the plasma is Argon (Ar), except for the LSMO films where the sputtering atmosphere is a mixture of Ar and Oxygen (O_2) with equal partial pressure.

Polycrystalline metal films were grown at room temperature by d.c. sputtering, i.e. at constant power supplied between anode and cathode to sustain the plasma. Epitaxial LSMO films were instead grown at high temperature by r.f. sputtering, with an a.c. power supplied. This is needed because the material is insulating at sputtering temperature and hence d.c. sputtering is not suitable because of target charging.

To make epitaxial growth occur, LSMO films must be deposited on substrates with similar lattice parameter. The fundamental criterion for epitaxy is defined by the lattice mismatch:

$$f = \frac{a_s - a_f}{a_s} \tag{3.1.1}$$

where a_s and a_f are the lattice parameters of the substrate and film, respectively. Ideally, for high quality epitaxial growth, the lattice mismatch should be as small as possible. Tab. III.1 shows the lattice parameters for the substrates commonly used for LSMO growth.

The substrate used in this work is $SrTiO_3$. In order to achieve a magnetocrystalline in-plane anisotropy, LSMO films were grown on (110) STO. As will be discussed in Cap. 5 this

	Cubic cell [Å]	**Cell volume [Å^3]**
$LaAlO_3$	3.790 ± 0.002	54.44 ± 0.08
$NdGaO_3$	3.86 ± 0.01	57.5 ± 0.4
$SrTiO_3$	3.905 ± 0.001	59.32 ± 0.05
$La_{0.67}Sr_{0.33}MnO_3$	3.87 ± 0.01	58.0 ± 0.4

Tab. III.1: Lattice parameters of several substrates and LSMO cubic cell.

gives a sharper hysteresis loop when the external field is applied along the [001] crystal direction.

3.1.3 Evaporation

Some of the multilayers used in this work were grown by electron gun evaporation. A thermoionic filament supplies the current to the beam and the electrons are accelerated by an electric field to strike the surface of the target to evaporate. Sequential deposition of different films is achived by evaporating from different crucibles.

3.1.4 Tunnel oxide formation

The formation of the thin oxide barriers has been obtained in this work by dry thermal oxidation. This technique is the most suitable for the formation of very thin and highly uniform tunnel barriers. The film to be oxidized (Al in our case) is exposed in oxygen athmosphere. Oxygen pressure, temperature of the substrate and exposition time are the parameters of interest to determine the oxide thickness.

The metal-metal oxide interface moves into the metal during the oxidation process. This creates a fresh interface region, with the surface contamination on the original metal film ending up on the oxide surface. The growth of a thickness x of oxide consumes a metal layer σx thick, with σ depending on molecular weight and density of both the metal and the metal oxide [1]. For Al_2O_3, $\sigma = 0.23$.

3.2 Film characterization

3.2.1 Structural characterization

By the term “structural properties” we hereby mean both the film microstructure and the morphological structure. The former deals with the arrangement of atomic planes within the films, while the latter refers to the properties that describe the ‘geometry’ of the layered structures.

In sputtered systems the following microstructure properties are of particular concern:

- Grain sizes: In polycrystalline films, the size of these grains has dramatic impact on the film properties (for example coercivity of magnetic films).
- Crystallinity: In epitaxial films, different crystal structures can be obtained by starting from different oriented substrates. The crystal structure can determine either the electrical or the magnetic properties of the film. Polycristalline films tend to show a particular out-of-plane orientation (in many cases this refers to the stacking of close packed planes), giving rise to *texture* of films. Even so the actual stacking pattern varies from grain to grain, and it tends to show a distribution around the film normal direction. This gives an idea of the degree of *mosaicity* of films.
- Strains: At least two types of strains can occur in sputtered films. The first type is present *globally* throughout the film that induces a strained state on the whole film. The second type is present *locally* as a consequence of, for example defects or local impurities, which leads to a localized stress state different from the rest of the film.

The main morphological properties of concern are:

- The (average) thickness of individual layers t.
- The morphological *roughness* of the layers, which is the deviation of the actual surface from the mean values. While it can be represented by the peak-to-valley value h, statistically this quantity is expressed in terms of the root-mean-squared (rms) deviation from the mean interface, namely σ.
- The chemical roughness of the interfaces: real interface between two film layers is not usually a sharp boundary between two different chemical species. A concentration gradient can be present in the film growth direction due to, for example, intermixing or chemical reactions.

- Spatial and vertical *correlation lengths* ($\xi_{//}$ and $\xi_{\perp}$): these refer to the extent in which the interfacial modulations are copied along and normal to the film planes respectively.

Two major techniques were employed to investigate these aspects of structural properties of magnetic films and heterostructures.

3.2.1.1 Atomic force microscopy (AFM)

The AFM was used to investigate the surface topology of the deposited films. The film surfaces were imaged in the 'tapping mode' configuration. In this configuration, the cantilever is set oscillating as it is dragged across the surface of the sample. As the tip comes across surface features with varying heights, the tip interacts with the surface, inducing a change in the amplitude of oscillation. Such oscillations are detected by a laser spot reflecting at the back of the cantilever, which is probed by a photodiode and converted into surface profile information. Resolution at atomic height scales can be achieved.

The power of the AFM is that it yields the real topology of the film surfaces. Instead of providing only images for qualitative descriptions, AFM data can be quantitatively analysed to obtain useful surface topological data such as surface roughness and spatial correlation length. Such data are useful, for example in estimations of magnetostatic coupling ('orange peel' coupling, see Sec. 2.4.2) in magnetic multilayers.

A brief account on the extraction of the aforementioned parameters using AFM is described as follows [2]. Roughness on its own is not a very precise quantity, as it varies with the lateral dimension being measured. When measurements are made at atomic scale in lateral directions, height variations between any two points are generally small, and the measured roughness is small in this case. The roughness tends to increase with the lateral size of measurement, but it has to converge in physically realistic surfaces. Such kind of lateral scale dependence of roughness has been considered as a consequence of the short-range diffusion-driven smoothing effect, together with a random surface roughening effect by parameter variation (such as deposition rate), which can take effect at all length scales. The result is that growing film surfaces tend to possess a time-invariant short-distance behaviour, together with a long-distance behaviour that is invariant towards lateral scale of measurements. This can be quantified by assuming a self-affine scaling behaviour of the film roughness. Under such a picture, the vertical dimension of measurements on a film surface scales by a factor of k^h

when the lateral dimensions is multiplied by k. h is known as the roughness exponent and contains important information regarding the growth mechanism of films. (The case $h = 1$ is knows as the self-similar case, which is basically a direct scaling of vertical and horizontal dimensions).

A quantity of importance in the growing surface problems is the height-height correlation function, which is defined as the mean of the square of the height difference between two points on the film surface separated by a distance r:

$$H(r) = \left\langle \left[z(r) - z(0) \right]^2 \right\rangle \tag{3.2.1}$$

where the $\langle \; \rangle$ sign refers to the average of the quantity[1]. From the previous discussion the following can be written:

$$H(r) \sim r^{2h}, \quad r << \xi_{//} \tag{3.2.2a}$$

$$H(r) \rightarrow 2\sigma^2, \quad r >> \xi_{//} \tag{3.2.2b}$$

and hence one can write:

$$H(r) = \left\langle \left[z(r) - z(0) \right]^2 \right\rangle = 2\sigma^2 f\left(\frac{r}{\xi_{//}} \right) \tag{3.2.3}$$

where $f(\mathrm{x})$ is a scaling function that can satisfy eqs. (3.2.2). In one of the forms it is written as [3]:

$$f(x) = 1 - \exp\left(-|x|^{2h} \right) \tag{3.2.4}$$

By calculating the height difference function for various r the values of σ, $\xi_{//}$ and h can be extracted. An example of the surface roughness analysis using such technique is shown in Fig. 3.1.

---

[1] A more generalized formulation of the height-height correlation function should take into account the potential directional dependence. In such a case a vector approach should be employed. In the discussions here isotropic roughness behaviour is assumed.

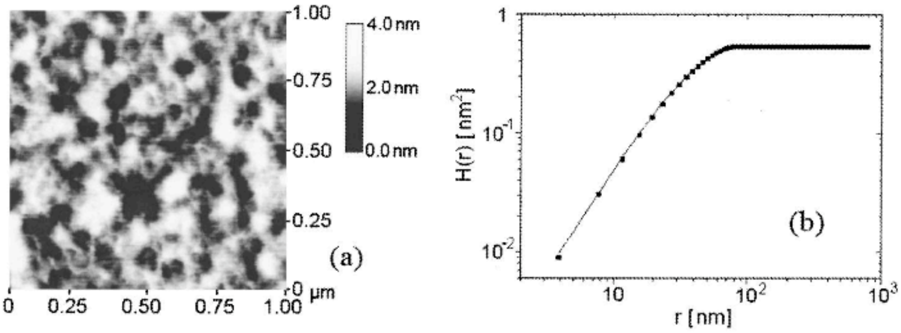

Fig. 3.1: *AFM image (a) and its height-height correlation function (b). The fit by eq. (3.2.3) gives $\sigma = 0.52$ nm, $\xi_{//} = 39$ nm and $h = 0.75$. Published in Ruotolo et al. [4].*

3.2.1.2 X-ray diffractometry (XRD)

As a means of investigating the structural properties of sputtered thin films, X-ray technique has a number of advantages. It is a non-local and non-destructive technique, has a large range of resolution (from tens of nm down to Å), and is relatively low-cost.

Two different regimes of X-ray diffraction can be employed to investigate the structural properties of layered thin films at different length scales.

- *High angle regime* ($2\theta > 15°$):

In θ-2θ scans (Fig. 3.2a), sample and detector angles are moving in a fixed ratio of 1:2 with respect to the direction of incoming radiation, i.e. the constrain $\omega = \theta$ is imposed. In such a configuration, the lattice spacing of the constituent layers can be determined whenever the Bragg condition is met:

$$n\lambda = 2d_{hkl}\sin\theta \qquad (3.2.5)$$

where n is an integer and d_{hkl} refers to the d-spacing between successive (hkl) planes. The

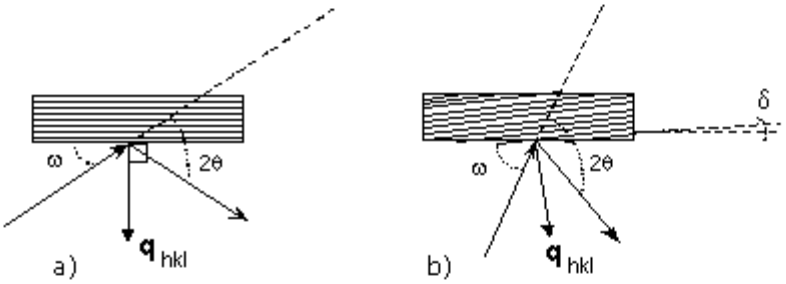

Fig. 3.2: *X-ray measurement geometries; (a) symmetric and (b) asymmetric Bragg diffraction.*

higher is the film epitaxy, the narrower is the peak full width at half maximum (FWHM) $2w_{HM}$.

In polycrystalline films the out-of-plane grain size D can be determined by means of the Scherrer equation [5]:

$$D = \frac{\lambda}{2w_{HM}\cos\theta} \tag{3.2.6}$$

where λ is the radiation wavelength.

ω-scans (*rocking curves*) are used to determine the mosaicity of the films deposited. In this case 2θ is fixed in correspondence of a previously detected Bragg peak and ω is scanned around the fixed 2θ by tilting the sample holder.

An important X-ray diffraction measurement method, which is of interest for this work, is the so-called *Reciprocal Space Mapping* (RSM). It allows a 2-dimension reconstruction of the reciprocal space, and is of particular importance when the diffraction planes are not parallel to the surface, $\delta \neq 0$ (Fig. 3.2b). In this case the Bragg diffraction is called “asymmetric” and, unlike the “symmetric” diffraction case ($\delta = 0$), information on the in-plane lattice parameters cannot be determined from the relative intensity of the peaks of the θ-2θ scan. The RSM is done by transforming a series of one-dimensional ω-scans taken with slightly different *offsets* $\delta = \theta - \omega$, with θ spanned around a previously detected Bragg peak. By combining these two motions and recording the scattered intensity as a function of these two angles (ω and θ), one can produce a 2 dimensional map of the spanned reciprocal space.

The transformation of the recorded angles to components of the reciprocal lattice vector perpendicular ($Q_\perp$) and parallel ($Q_{//}$) to the film plane is done using the following simple transformations:

$$Q_\perp = \Delta Q\cos(\delta) \tag{3.2.7a}$$

$$Q_{//} = \Delta Q\sin(\delta) \tag{3.2.7b}$$

where $\Delta Q = 2q_0\sin(\theta) = 2(2\pi/\lambda)\sin(\theta)$. From $Q_\perp$ and $Q_{//}$ the corresponding lattice parameters can be calculated. In other words, RSMs allow the estimation of both the perpendicular-to-plane and in-plane lattice parameters, which is of great use, for instance, when determining the film stress (strain). An example of RMS on a STO (001) substrate is shown in Fig. 3.3.

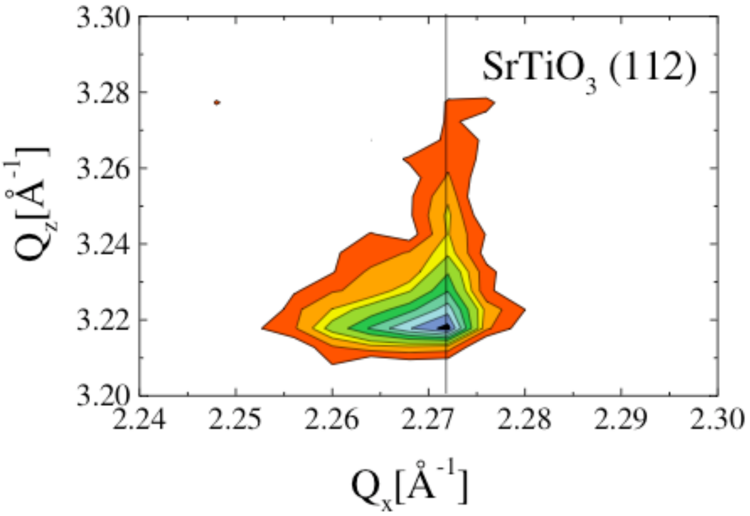

Fig. 3.3: *RSM of a STO (001) substrate around the (112) reflection. Taken from [6].*

- *Low angle regime* ($2\theta < 15°$):

X-ray reflectivity, which exploits the low angle regime ($2\theta < 15°$), is used to investigate the morphological properties of multilayer structures. X-rays travels with different speed in different materials. In general the refractive index of X-ray is slightly below 1, and is determined by the electron density (hence the mass density and the atomic number) of the material [7]. In the high angle regime this is not a problem, since refraction is minimal. In the low angle regime, on the other hand, the effect becomes more important. Potential refraction, absorption and multiple reflections of X-rays have to be taken into account to fully model the effect. Low angle x-rays are suitable to measure the thickness of a film and the thicknesses of films in multilayers with repeated bilayer. The scan shows (see Fig. 3.4) closely spaced oscillations, known as the Kiessig fringes, due to the interference of X-rays from the bottom (film/substrate interface) and the top (film/air interface) surfaces of the films. The closer are the fringes, the thicker is the film. The total film thickness can be roughly calculated, from the 2θ values of consecutive peaks, as [8]:

$$\sin^2\theta_m - \sin^2\theta_{m-1} = \left(\frac{\lambda}{2t_{film}}\right)^2 \tag{3.2.8}$$

By plotting ($\sin^2\theta_{m+1} - \sin^2\theta_m$) for successive peaks against n (n can be an integer starting at any arbitrary value) the film thickness can be determined from the slope.

In the particular case when there is a repeated structure within the sample (for instance repeated GMR bilayers Co/Cu or Fe/Cr) a Bragg peak with the 'lattice parameter' being the

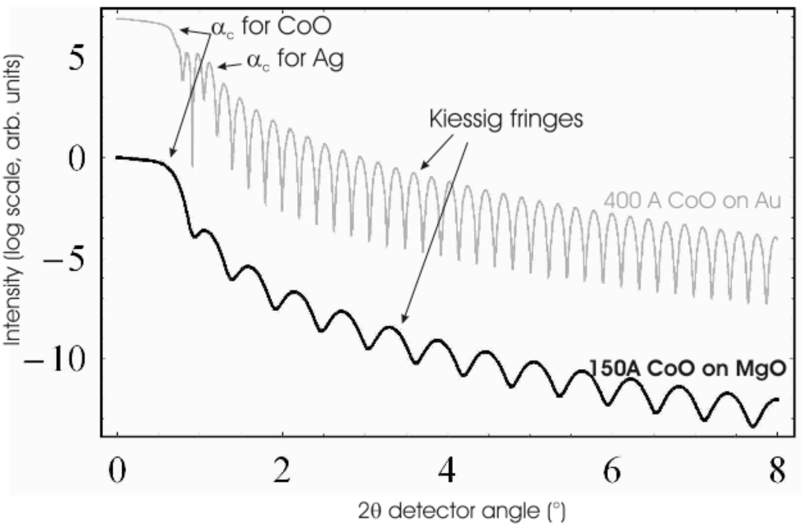

Fig. 3.4: *Simulated reflectivity curve for (top) 40 nm CoO on an Au substrate. The gold having a high electronic density, its critical angle α_{crit} is higher than the one for the CoO over-layer and therefore both can be visible. (bottom) 15 nm of CoO on MgO, where only the critical angle of the CoO is observable.*

repeated bilayer thickness can be observed. This permits a quick estimate of the repeated bilayer thickness.

The very general trend of film or interface roughness on the reflectivity scans is to cause a more rapid drop in the reflectivity. The contrast of modulation can also be reduced due to the presence of film roughness. Therefore, on a principle basis, information on interlayer roughness can be extracted. Yet, this is not easy and a complex fitting must be performed to obtain an accurate estimate of the morphological parameters.

3.2.1.3 Scanning electron microscopy (SEM) and energy dispersive X-ray spectroscopy (EDS)

A schematic diagram of a SEM is provided in Fig. 3.5. The electron gun consists of a cathode (a filament made normally of tungsten (W) wire), which is heated to emit electrons by thermionic emission. The electrons are accelerated towards an anode with a potential difference of several tens of kV (the maximum voltage is typically 30 kV). A series of electromagnetic lenses focus the electron beam to a spot on the surface of the specimen. The beam is rastered over the surface of the specimen using electrostatic coils. A variety of signals can be emitted as a result of interactions between the electron beam and the specimen. Two are of concern for this work. Emitted secondary electrons are detected to form the image of the rastered surface. The use of a SEM to produce images will be discussed in Sec 4.1.2. Let us point out here that, unlike AFM imaging, the SEM does not give the “real” topology of the

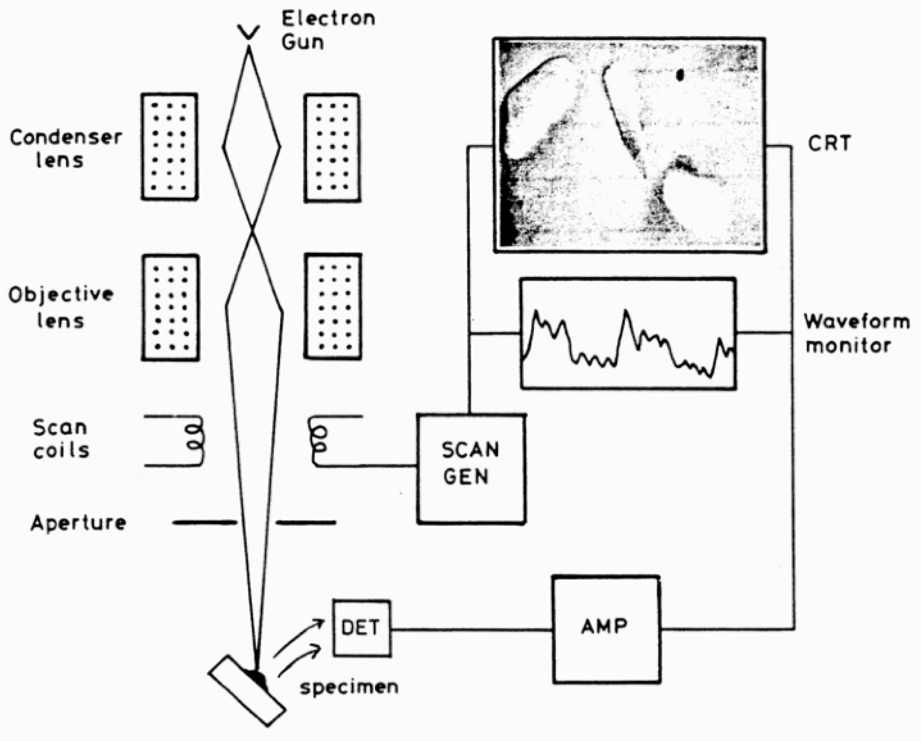

Fig. 3.5: *A schematic diagram showing the main components of an SEM.*

film surface, so it is not suitable for studying the morphology. The qualitative image provided by the SEM is instead of great use to monitor the FIB process in dual beams FIB/SEM microscopes (see Sec. 4.1).

The X-ray signal emitted from the specimen contains characteristic peaks whose energy can be related to an atomic transition and hence to a particular chemical species. There are two electron-beam specimen interactions to consider here. There is core scattering, which results in the emission of a continuous background and inner shell ionization, which gives the characteristic peaks. We will just concentrate on the latter. The incident electron has sufficient energy to knock an inner shell electron out to the vacuum. An electron from a higher energy level falls down to the partially filled lower energy level and a photon is emitted. The energy of the photon corresponds to the difference between the two energy levels. Transitions are labelled as K (*s*-electrons), L (*p*-electrons) or M (*d*-electrons), which is the energy level from which the electron was ejected and they are also given subscripts such as α, β, γ which indicates from which level the electron that fills the hole has come. The X-ray from the most probable transition is designated α. Therefore, a K_α X-ray is formed from a transition from the L shell to the K shell whereas a K_β X-ray results from a transition from the M shell to the K shell.

EDS is the X-ray detector system and is based on a silicon based p-i-n junction. An incoming X-ray generates a photoelectron, which leads to the generation of a number of electron-hole pairs. The number of pairs generated is proportional to the energy of the X-ray. The signal is amplified and is then sorted according to voltage amplitude by a multichannel analyzer. Several thousand pulses per second can be processed and so a spectrum can be obtained in a short space of time. The current produced by the X-ray is small compared to the conductivity of the silicon and so the junction is reverse biased. The silicon is doped with Li to increase its resistivity and the detector is cooled to keep thermally activated conductivity and electronic noise to a minimum.

In order to estimate the amount of an element present in a sample, the number of counts obtained in a fixed time interval, N_{spec}, can be compared with those from a standard of known composition, N_{std}. Therefore, the concentration of the element is given by:

$$C_{spec} = \frac{N_{spec}}{N_{std}} C_{std} = kC_{std} \tag{3.2.9}$$

However, if the specimen is not a pure element then the situation is more complex. Three correction factors must be applied and we will discuss each one in turn now. The atomic number correction (*Z*) accounts for the differences in the efficiency of X-ray generation. This depends on how far the electrons penetrate before they lose too much energy to excite X-rays and how many electrons are backscattered without exciting X-rays. The absorption correction (*A*) accounts for the differences in the mass absorption coefficients of the elements involved. Finally, the fluorescence correction (*F*) is necessary if element Y emits characteristic X-rays of energies greater than the energy for excitation of characteristic X-rays from element Z. It is a very inefficient process but can be significant if elements have a similar atomic mass. These corrections are known as *ZAF* corrections. To determine these factors, the sample-detector geometry must be known accurately and the sample must be flat. If this is the case then errors can be as low as ±3 %. Eq. (3.2.9) can now be modified to include the *ZAF* corrections:

$$C_{spec} = kk_Z k_A k_F C_{std} \tag{3.2.10}$$

k_Z, k_A and k_F require some knowledge of the specimen composition so the process is iterative.

For the quantitative analysis, standardless analysis was used, which is the simplest of the correction procedures and does not rely on obtaining good quality bulk standards. Only the correct beam energy and the elements to be analyzed need to be supplied and the analysis total will always be exactly 100%. There are a few limitations with EDS for measuring thin film samples but once one is aware of these, it can be an accurate method of determining film composition. The first is that the effective probe depth of the incident electrons is about 1 μm. However, the computer program that carries out the analysis assumes that the sample is homogeneous, which is not the case since the thin film is on a substrate. However, if one deposits a thick film (> 100 nm) and uses a low accelerating voltage (for instance 5 keV), all interactions take place within the film.

3.2.2 Magnetic characterization

The study of magnetic properties in this project was done by a vibrating sample magnetometer (VSM), which measures the global magnetic response of the sample with regards to an external applied field. Developed by Foner [9], the VSM is a commonly employed technique in the characterization of all kinds of magnetic samples, ranging from thin films to bulk materials, with sensitivity generally down to the range of 10^{-9} Am^2 (μemu in CGS). The technique is non-destructive, and no sample preparation is needed in general.

The schematic of a VSM set-up is shown in Fig. 3.6. Sample to be examined is placed in the middle of an applied magnetic field, together with a pair of stationary pick-up coils. By vibrating the sample in a uniform field, the sample is set into relative motion with the pick-up coils and signals (in the form of induced e.m.f., according to the Faraday's law) are generated in the pick-up coils due to the presence of the oscillating magnetic flux from the sample. By calibrating the VSM with a known strength of magnetization, absolute values of magnetic moments in the samples along the field direction can be obtained.

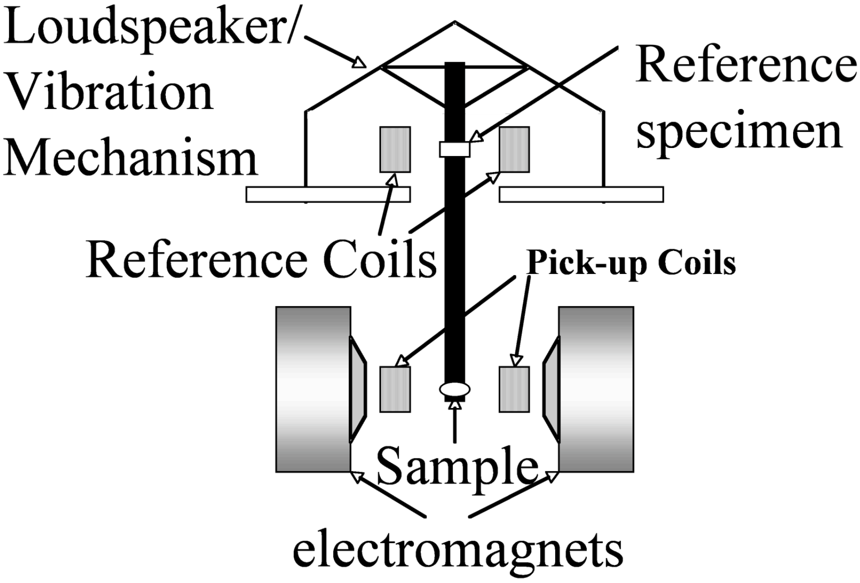

Fig. 3.6: *Schematic of a vibrating sample magnetometer.*

3.2.3 Electrical characterization

All electrical measurements were done with a four-point technique. Chips were secured by silver paste onto a copper chip holder that is then stuck on the dip probe holder with vacuum grease or carbon tape. The chip pads were wire-bonded to the copper wires of the chip holder using an ultrasonic wire-bonder with 25 μm diameter Al wire. The measurement rig and the accompanying software were developed by using standard electronic instruments and LabVIEW^{TM} language, respectively.

The dip probe is provided with a Ge thermometer and a copper coil that allows application of in-plane magnetic fields. A μ-metal shield was placed over the end of the probe to reduce external electromagnetic noise. Measurements were done at temperature ranging from 4.2 K to room temperature.

3.3 Device fabrication

3.3.1 Photolithography

The deposited films and heterostructures were patterned into device structures by using standard photolithographic techniques with ultra-violet (UV) radiation source. The pattern is transferred from a chromium on fused silica photomask to a polymer film (*resist*), which allows replication of the pattern in the underlying film. The photomasks can be either positive or negative. In the first case a chemical or physical etching is followed, whereas, in the second case, a lift-off technique is used to achieve the desired structure. Multiple step fabrication processes were carried out by using a Karl Suss mask-aligner. Fig. 3.7 shows the designed positive mask used for the formation of the 4 μm tracks that would be subsequently processed in the Focused Ion Beam (FIB) microscope. Devices are made in the central thin tracks, while the remnant pattern acts as wiring and connection pads.

3.3.2 Etching

Two kinds of etching processes were used in this work. In both cases the defined resist acts as a thick layer of protection against attack. Regions not covered with resist are therefore etched away, and when the resist is dissolved, the desired pattern remains in the film.

The first kind is wet chemical etching. The sample is immersed in a solvent; a reaction

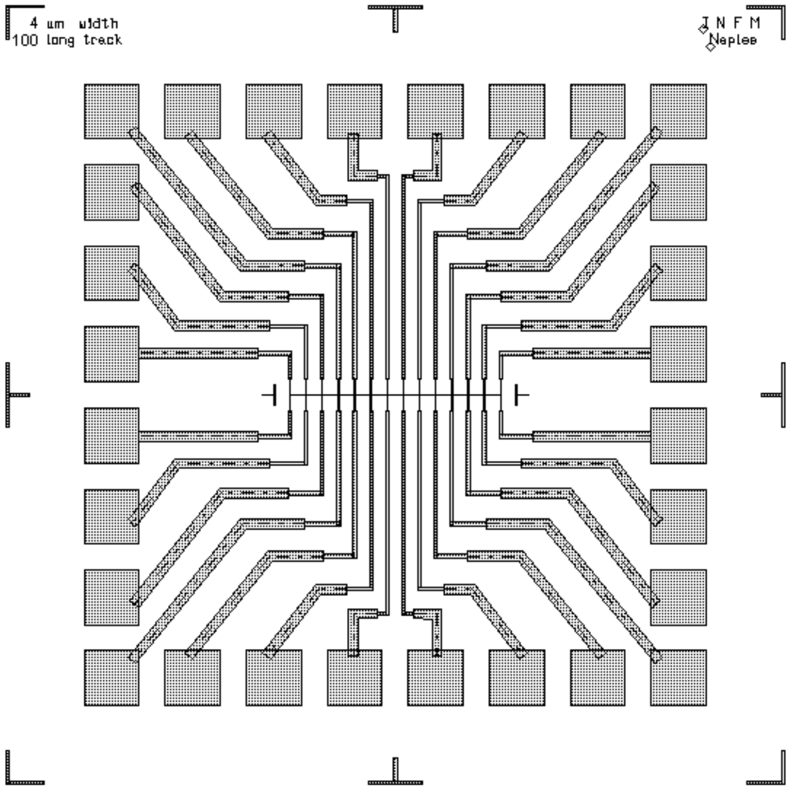

Fig. 3.7: *Spider mask designed for patterning films and multilayers to be subsequently process in FIB.*

occurs that dissolves the film in the area uncovered by the resist. This kind of etching does not provide high resolution (down to 1 μm) and has been used in the present work only for the formation of metal tracks that would be subsequently patterned by FIB.

The second kind of etching is physical. In a vacuum system, Ar^+ ions from an ion gun are accelerated at the sample at high energy, which mills the film away. The etched material is pumped away. This process assures a high resolution, which is limited only by the resolution of the lithography process.

3.3.3 Lift-off

For so-called ‘lift-off ’, the definition occurs before deposition, using a negative version of the mask (Fig. 3.8). After the film is deposited, the material sputtered onto the resist is removed when the resist beneath is dissolved in acetone, leaving the required pattern behind. The rounded resist profile (due to scattering of the UV radiation, which is greatest near the surface of the photoresist) can be a problem. The film grows up the sides of these rounded resist walls, forming a continuous layer that peels off when the resist is dissolved. Large edges sticking up above the tracks can also be left, which is problematic for the Focused Ion Beam processing. Overdeveloping the photoresist will also tend to smooth out the edges of

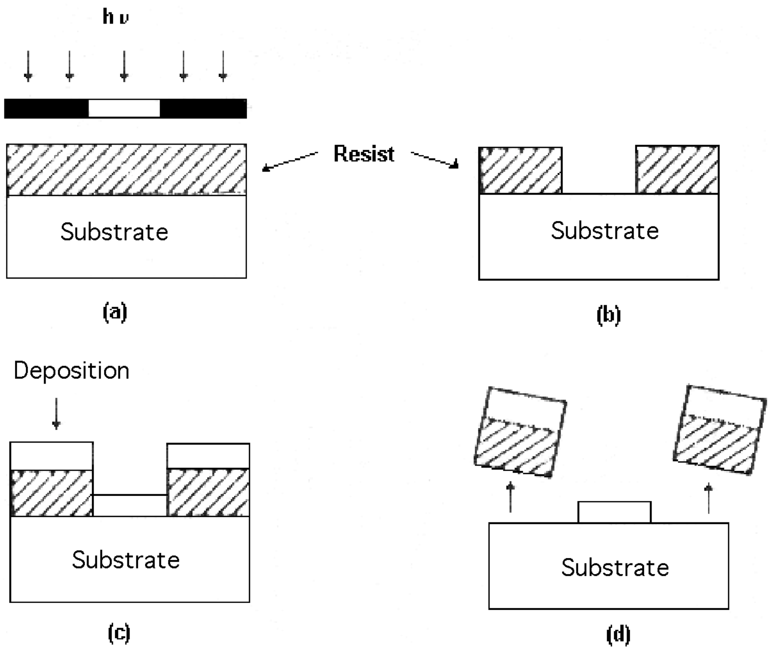

Fig. 3.8: *Lift-off process: (a) a resist pattern is defined by UV-lithography; (b) resist is developed; (c) the film is deposited; (d) the resist is dissolved in acetone.*

the patterns leading to the same effect. Treatment of the resist with chlorobenzene, (after UV exposure but before developing), causes an overhang in the edge profile. This prevents growth of the film over the sides. Given these added complexities, lift-off was used in this work only for the metallization of the pads of the manganite-based devices.

References

[1] S. Sze, *Semiconductor devices* (J. Wiley and sons, Murray Hill, New Jersey, 1985).

[2] H.N. Yang, G.C. Wang and T.M. Lu, *Diffraction from rough surfaces and dynamic growth fronts*, pp. 136-168, (World Scientific Pub., 1993)

[3] V. I. Trofimov and H. S. Park, *Appl. Surf. Sci.* **219**, 93 (2003).

[4] A. Ruotolo, C. Bell, C. W. Leung, and M. G. Blamire, *J. App. Phys.* **96**, 512 (2004).

[5] B.D. Cullity, *Elements of X-ray diffraction*, pp. 99-106, (Addison-Wesley Pub. Co., 1978).

[6] C. Aruta, J. Zegenhagen, B. Cowie, G. Balestrino, G. Pasquini, P.G. Medaglia, F. Ricci, D. Luebbert, T. Baumbach, E. Riedo, L. Ortega, R. Kremer, and J. Albrecht, *phys. stat. sol. (a)* **183**, 353 (2001).

[7] T.P.A. Hase, *Ph.D. Thesis*, University of Durham (1998).

[8] K.Y. Kok, *Ph.D. Thesis*, University of Cambridge (1997).

[9] S. Foner, *IEEE Trans. Magn.* **17**, 3358 (1981).

Chapter 4

Focused Ion Beam nano-patterning techniques

The method of processing the films in the focused ion beam to create planar devices is discussed, as well as the three-dimensional focused ion beam fabrication technique used to create CPP devices.

4.1 The Focused Ion Beam (FIB) microscope

FIB systems operate in a similar fashion to a scanning electron microscope (SEM) (see Sec. 3.2.1.3) except, rather than a beam of electrons and as the name implies, FIB systems use a finely focused beam of ions that can be operated for imaging or for site specific sputtering or milling. Many different ion sources are possible [1], but the most reliable is presently the liquid gallium (Ga) source, which is used in the present work.

A schematic of the system is shown in Fig. 4.1a. The Ga self assembles into a sharp tip (diameter ~ 2 nm) at high electric field. From this tip Ga$^+$ ions are extracted. These ions pass through a series of apertures and electrostatic lenses which focus them onto the sample. The working pressure in the chamber is better than 10^{-3} Pa, while the ion column pressure is maintained at a pressure lower than 10^{-5} Pa.

As Fig. 4.1b shows, the gallium (Ga$^+$) primary ion beam hits the sample surface and sputters a small amount of material, which leaves the surface as either secondary ions (i$^+$ or i$^-$) or neutral atoms (n^0). The primary beam also produces secondary electrons (e$^-$), as in the case of a SEM. As the primary beam rasters on the sample surface, the signal from the sputtered ions or secondary electrons is collected to form an image.

At low primary beam currents, very little material is sputtered and the FIB works as a microscope; modern FIB systems can achieve 5 nm imaging resolution. At higher primary currents, a great deal of material can be removed by sputtering, allowing precision milling of the specimen down to a sub-micron scale. For very precise milling, a large number of

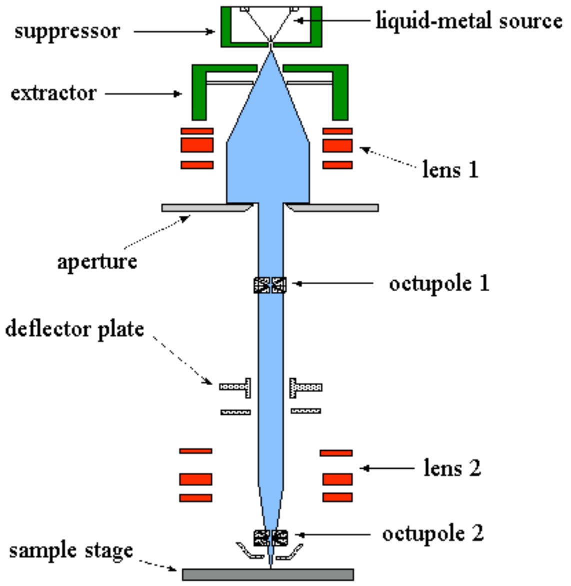

(a)

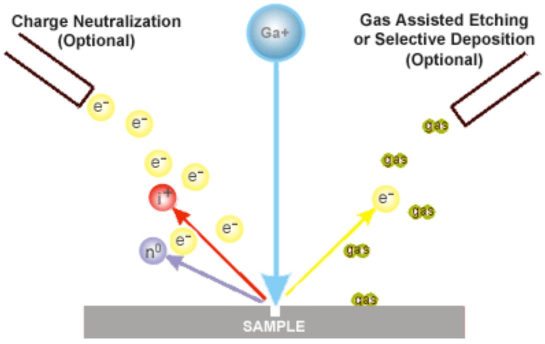

(b)

Fig. 4.1: *(a) Schematic view of a FIB column; (b) FIB operation modes.*

repeated scans are made with low beam currents. The resolution that can be achieved in this way is nominally the imaging resolution. This resolution is to be meant as the minimum spot size available, which is limited by chromatic aberration due to the distribution of ion energies. Yet, the nominal resolution can be misleading in case of milling operation, because it does not take into account the Gaussian profile of the beam. This means that the thicker is the film to cut, the smaller is the actual resolution achievable. We will discuss this and others limitations of the FIB milling in details later in this chapter.

In order to avoid charging of the specimen, the milling ions have to be neutralized after collision. In conductive samples this is simply done by providing the neutralizing charge through the stage and the sample holder. The stage current can be monitored and, as will be discussed later, this monitoring provides a fine method to calibrate the milling rate of films and multilayers.

If the sample is non-conductive, a low energy electron flood gun (see Fig. 4.1b) can be used to provide charge neutralization. In this manner, by imaging with positive secondary ions using the positive primary ion beam, even highly insulating samples may be imaged and milled without a conducting surface coating, as would be required in a SEM.

In addition to primary ion beam sputtering, modern systems permit local "flooding" of the specimen with a variety of gases. These gases can be of two types and used either for local sputtering of metals or for reactive etching.

In the former case, an organometallic gas is injected into the chamber during milling through a needle brought close to the sample surface. Where the beam dwells the compound is broken down, the volatile organic gases escape and the metal is deposited (although in practice the deposited metal film is contaminated by Ga and other organic compounds [2]).

In the latter case, a selective gas is injected into the chamber to produce assisted chemical etching, the so-called *Enhanced Etching* (EE). This reactive gas greatly increases the milling rate of the FIB. It is also believed to reduce the Ga redoposition during the milling process because the gas should form a volatile compound with the milled material, which is subsequently pumped out of the system. Yet, as will be discussed in detail in Sec. 4.3, many authors have tried patterning of tunnel junctions through the use of EE but they have not observed an improvement of the quality of the devices.

4.1.1 Advantages and limitations of the FIB lithography

In contrast to other forms of lithography, FIB processing requires no masking with resist, post-FIB wet or dry etching, or resist removal. The most important advantage is the unique possibility offered by the FIB to operate in 3 dimensions. This “nano-sculpting” possibility is peculiar of this system and has been used in this work, as will be largely discussed in Sec. 4.3. For the reasons above, FIBs are being increasingly used for a range of applications, including the site-specific preparation of transmission electron microscope (TEM) specimens, failure analysis in the semiconductor industry, and micromachining applications.

FIB processing inevitably leads to Ga implantation. Potential poisoning / damage / amorphous layer formation due to this Ga implantation must be considered. Table IV.1 shows stopping and straggling distances of Ga^+ ions calculated by Transport and Ranges of Ions in Matter (TRIM) calculations, for a variety of elements, (the longitudinal straggle is the standard deviation of the distribution of distances about the mean stopping distance). The effect of Ga^+ implantation is particularly important in magnetic materials. Irradiating magnetic materials, even with fluencies of Ga as low as to produce topological changes smaller than 1 nm, strongly changes the magnetic properties of the irradiated material. In particular, it has been observed for the first time by Chappert et al. [4] that the coercivity reduces faster than the saturation magnetization and, when the fluence approaches a few thousand of ions per spot, the material becomes completely paramagnetic. This means that, when making a cut with the ion beam, one can be sure that the film has become paramagnetic close to the cut edges over a distance given by the lateral straggling, in the best case. As will be discussed in Sec. 5.2, this can represent a limit in the reduction of magnetic system on nano-scale. Moreover, it can strongly affect the performance of spintronic devices. A way to reduce this problem is to deposit a protecting metal layer on the film to mill, assuming that the upper layer can be afterwards removed by chemical etching with a solvent that does not react with the film of interest. This condition is particularly hard to meet.

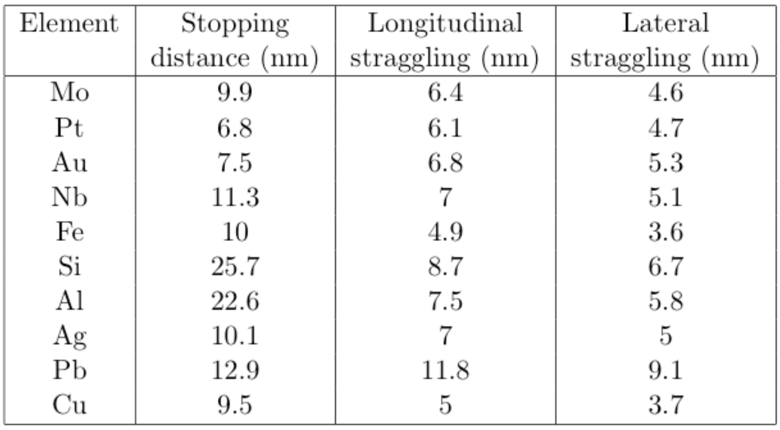

Element	Stopping distance (nm)	Longitudinal straggling (nm)	Lateral straggling (nm)
Mo	9.9	6.4	4.6
Pt	6.8	6.1	4.7
Au	7.5	6.8	5.3
Nb	11.3	7	5.1
Fe	10	4.9	3.6
Si	25.7	8.7	6.7
Al	22.6	7.5	5.8
Ag	10.1	7	5
Pb	12.9	11.8	9.1
Cu	9.5	5	3.7

Tab. IV.1: *Stopping distances and straggling lengths for 30 kV Ga+ ions in various materials. After [3].*

When milling with the FIB, part of the milled material tends to re-deposit and form veils on the film. The amount of this so-called “resputtered” material increases with the milling rate, i.e. with beam current, since the pump is less efficient in pumping it away. This problem is particularly important when trying to fabricate tunnel devices. Enhanced etching has been proved [5] not to reduce the problem. Instead, a post-anodization process has revealed to be successful in removing the shorting veils [6]. The process relies on a very fine control of the anodization dynamics and introduces a further uncertainty on the dimensions of the devices, particularly in the case of very small (lateral size < 200 nm) junctions. This could be one of the reasons of the large changing in resistance from sample to sample reported in Ref. 6.

As will be discussed in the following, a post-cleaning of the sidewalls with very small (1pA) beam has been tried in this work to produce tunnel spin-valve Josephson junctions.

When the thickness of the structure to mill is of several hundreds of nm, beam drift during milling and the beam profile prevent very small (< 50 nm) features being reliably cut. Smaller dimensions are possible in a more uncontrolled manner. Yet, when milling a multilayer, if the upper layer acts as an electrode, the Gaussian beam profile rounding off the top layer does not represent a problem. This rounding is a problem with TEM sample preparation where parallel side walls are crucial, and can be overcome by slightly tilting the sample by ± 1° - 4° away from $\theta = 0°$ (with θ the angle between beam and film normal).

4.1.2 The FEI FIB/SEM Quanta 200 3D

The system used in this work is the dual beam FIB/SEM Quanta 200 3D by the FEI-company shown in Fig. 4.2a.

The Quanta 3D DualBeam is a combination of two systems:

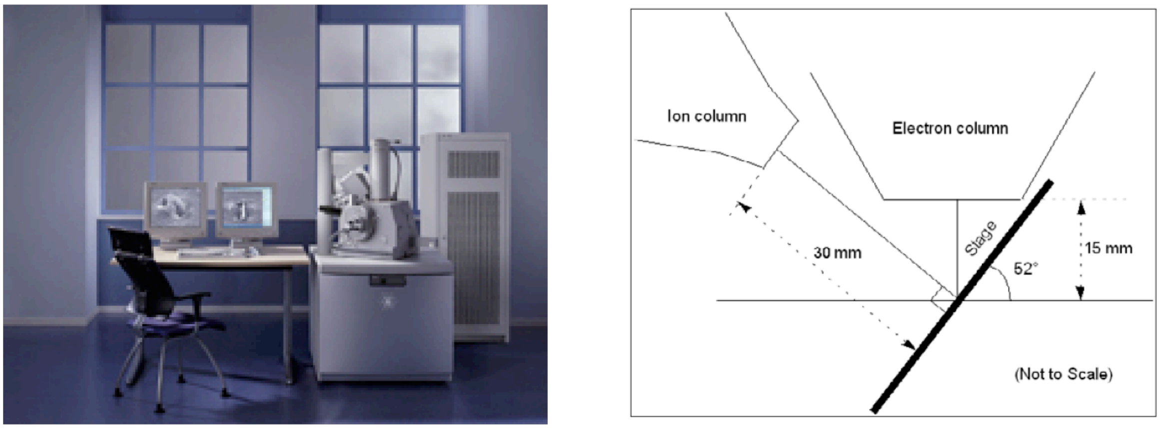

Fig. 4.2: *(a) Picture of the Dual Beam Quanta 200 3D; (b) Schematic view of the relative position of columns and sample. Taken from [7].*

- a SEM achieving magnification over 100000×;

- a FIB that is provided with apertures ranging from 1 pA to 20nA.

The integration of both systems is of particular use for our purposes, since it allows the imaging and positioning of the magnetic sample without irradiating it with Ga^+ ions. After positioning the sample, one can easily switch from SEM to FIB to perform the patterning.

The electron and ion columns are mounted as illustrated in Fig. 4.2b, which shows the stage tilted to 52°. The sample must be placed in the so-called *eucentric point* that is the point at which the stage-tilt axis and the ion and electron beam axes intersect. At this point, no matter which direction the stage is tilted or rotated, the feature of interest remains focused and almost no image displacement occurs. The eucentric point is adjusted after loading any sample. When a feature of interest is at eucentric height, one is able to switch from SEM to FIB, as well as use the other different Quanta 3D workstation components, such as the Gas Injector System (GIS) and EDX, in a safe and optimal way. Positioning the sample at the eucentric height is of crucial importance for two reasons. First of all, the feature of interest would otherwise move during tilt, as shown in Fig. 4.3. Moreover, when the feature of interest is at the eucentric point and has been focused for both the SEM and FIB, one can view by SEM and mill by FIB, without loosing focusing for either SEM or FIB, regardless to stage tilt.

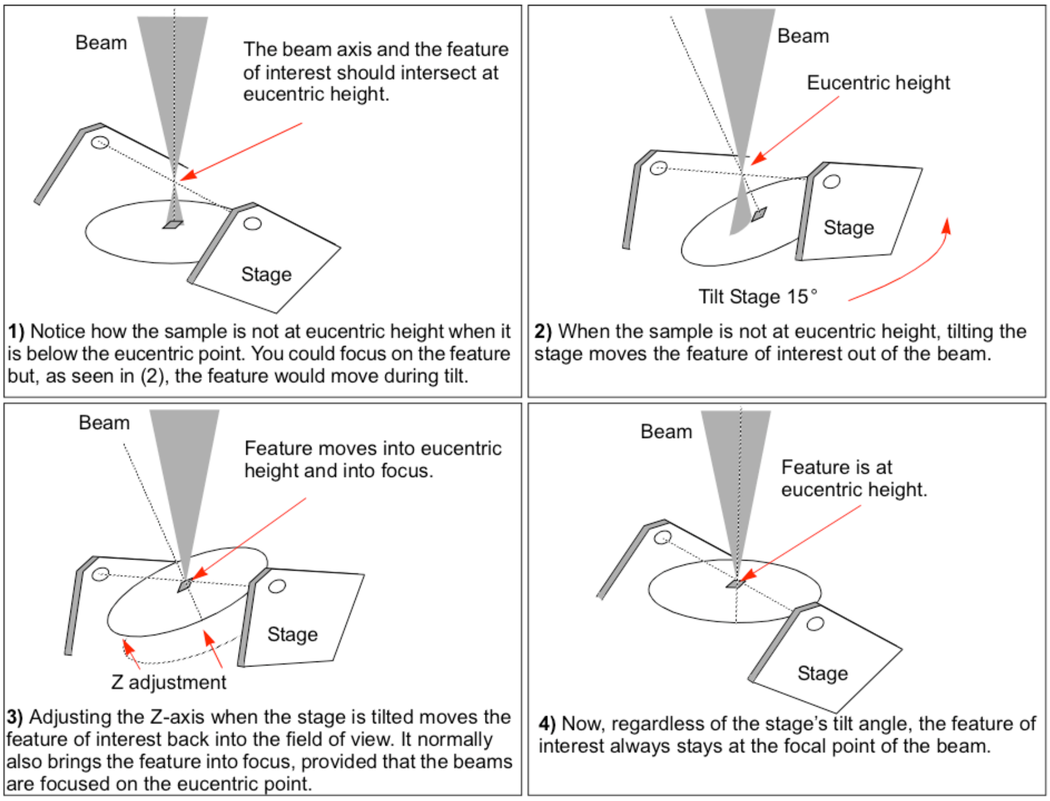

1) Notice how the sample is not at eucentric height when it is below the eucentric point. You could focus on the feature but, as seen in (2), the feature would move during tilt.

2) When the sample is not at eucentric height, tilting the stage moves the feature of interest out of the beam.

3) Adjusting the Z-axis when the stage is tilted moves the feature of interest back into the field of view. It normally also brings the feature into focus, provided that the beams are focused on the eucentric point.

4) Now, regardless of the stage's tilt angle, the feature of interest always stays at the focal point of the beam.

Fig. 4.3: *Understanding eucentric height. Taken from [7].*

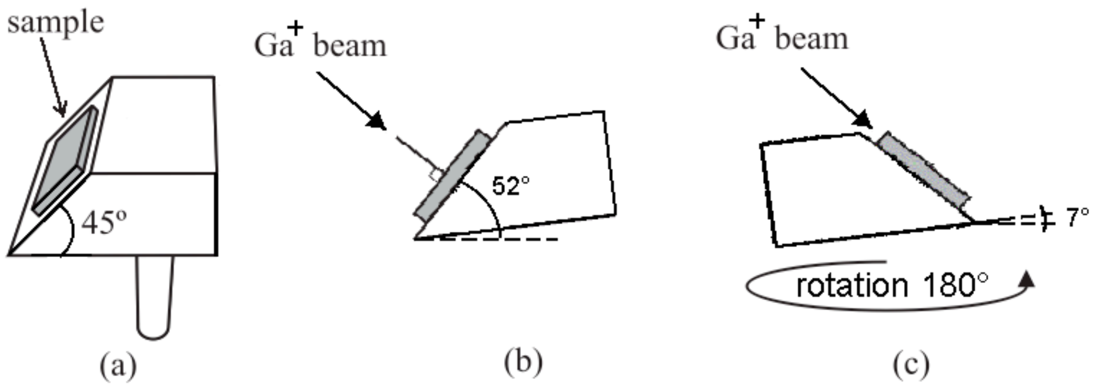

Fig. 4.4: *(a) Schematic of the 45° wedge holder; (b) a tilting of 7° permits milling from θ = 0°; (c) a rotation of 180° and a tilt back of 7° permits milling from θ = 90°.*

The stage can be rotated by 360° but the maximum stage tilt is 60°. This constrain on the maximum tilt does not allow full 3D patterning with the standard sample holders. The FEI company has provided us with a 45° wedge holder, so that, by using tilting and rotation as explained in Fig. 4.4, the full range of $\theta = 0°$ (Fig. 4.4b) to $\theta = 90°$ (Fig. 4.4c) is possible.

The system is provided with several detectors. The only one of use for this work is the Everhart Thornley Detector (ETD). This is a scintillator photo-multiplier type detector that is permanently mounted in the chamber above and to one side of the sample. It works in two modes: i) Secondary Electrons (SEs) and ii) Backscatter Electrons (BSEs). SEs electrons are those pushed out of the sample atoms (see Fig. 4.5b) because of inelastic scattering with the electron beam. Since the SEs are moving very slowly when they leave the sample, they need to be attracted by the detector which is for this reason positively polarized (+250 V). Some of the incident electrons can be elastically scattered back because of the interaction with the nuclei of the topmost layer atoms (see Fig. 4.5c). The number of BSEs leaving the sample surface is significantly lower than that of SEs and the collection efficiency cannot be

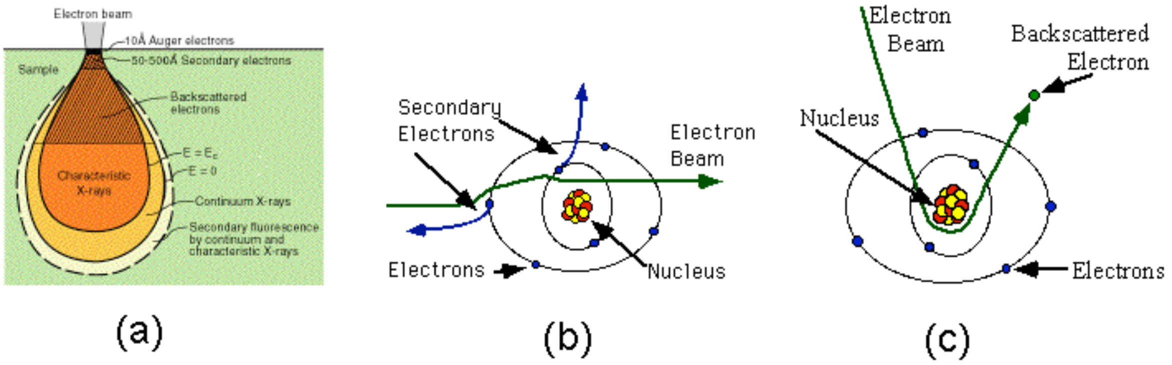

Fig. 4.5: *(a) Volume interaction of electron bombarding; (b) schematic view of the secondary electron emission through electron-electron interaction; (c) schematic view of the backscattering through electron-nucleus interaction.*

significantly improved by positively biasing the ETD. For this, the detector is negatively polarized and the collection of BSEs is made by dedicated detectors. It is worth noticing that the number of BSEs is depending on the atomic configuration of the stroked element; hence BSEs can be used to get an image that shows the different elements present in a sample.

In this work the primary beam was mainly the ion beam, thus the ETD was always used to detect SE. The other detectors provided are not discussed here because not used in this project.

As already explained, the milling ions have to be neutralized after collision. Although the system is provided with a charge neutralizer for non-conductive samples, the neutralization for the conducting samples produced in this work has been done by providing the neutralizing charge through the sample holder.

4.2 Planar device fabrication procedure

In this section, the procedure used to fabricate planar current-in-plane (CIP) devices is discussed. The sample is positioned at the eucentric height and tilted by 52° with respect to the SEM axis (see Fig. 4.2b). The sample is always kept perpendicular to the FIB axis ($\theta = 0°$) for 2D FIB milling.

Staring from a micro-patterned track, the track width is firstly reduced by using a relative high current (100 pA). Fig. 4.6 shows the narrowed track milled with 100 pA beam current

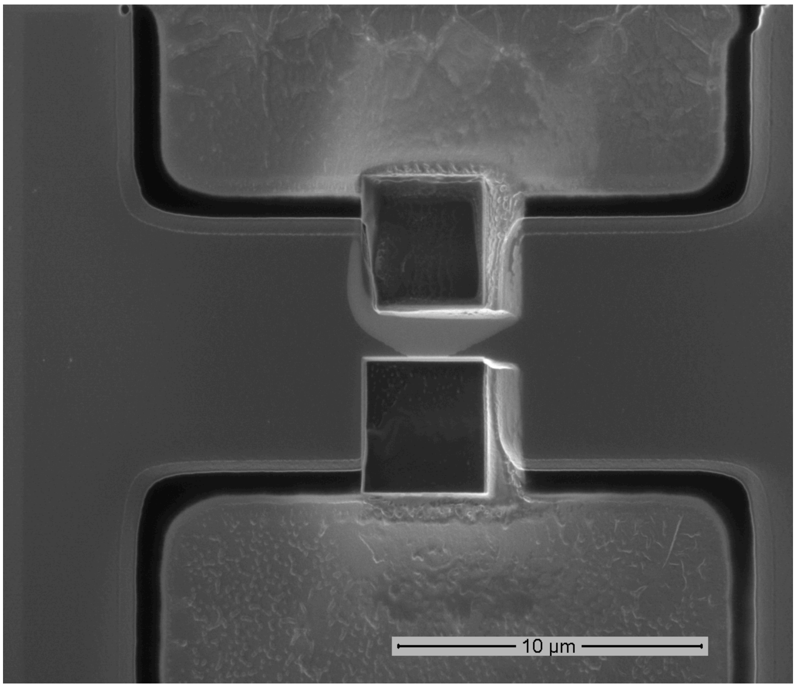

Fig. 4.6: *FIB image of a thick track narrowed with FIB. Light grey is resputtered material.*

for the top cut and 30 pA for the bottom cut (and imagined by 30 pA FIB primary beam) of a thick multilayer structure. This image is illuminating in showing the problem of resputtered material. Notice how, although using relatively low current beam during milling, a veil (light grey in the picture) redeposits on the track and, for 100 pA beam current, it covers the whole track. If the topmost layer of the structure is just the top electrode of a current-perpendicular to plane junction this do not represent a problem (in this case the problem is only represented by the veil formed on the lateral sidewalls, see Sec. 4.3). In case of CIP devices this redeposition must be avoided or confined at the side-borders to be afterward removed by a post-cleaning with very low beam current. For this reason current smaller than 30 pA are more appropriate although the milling time will be longer, which could give problems with stage drifting.

The sidewalls of the narrowed track are usually cleaned with a beam current of 10 pA, using the standard software ‘cleaning tool’, which repeatedly steps in a single pixel wide line. This removes excessive gallium implantation from the larger beam size of the larger beam currents and makes the sidewalls more vertical due to the smaller spot size (Fig. 4.6). Of course the track is further narrowed during the cleaning process. Moreover, the process is meant to remove resputtered material from both the side-borders and sidewalls.

To avoid problems with redeposition, in our planar devices we chose to mill with 10 pA beam and clean with 1 pA beam. This was possible because the structure to mill was just a

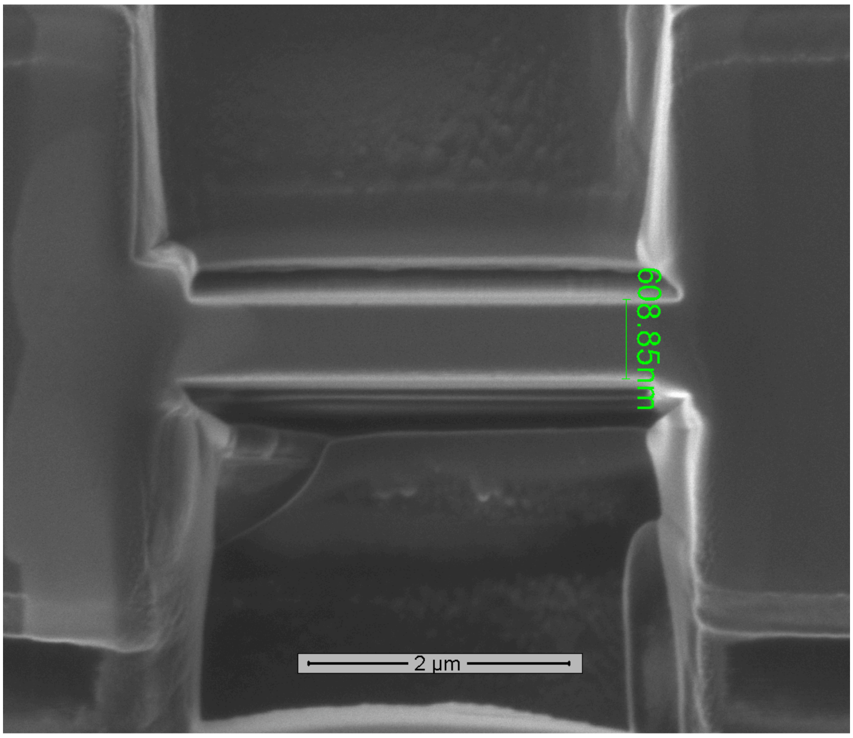

Fig. 4.6: *FIB image of a track after sidewall cleaning with 10pA.*

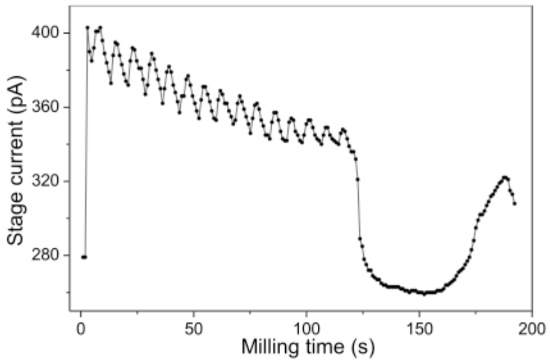

Fig. 4.7: *Stage current during milling of a ~ 3 × 1* μm^2 *box with 150 pA beam through a NiCu(Nb/NiCu)*$_{15}$ *multilayer from* $\theta = 0°$.

thin LSMO film, and hence the milling with 10 pA could be performed in a time smaller than the stage drifting typical time.

During the first cut, the *stage current* (or *end point monitor current*) is monitored. This allows calibration of the milling rates. Fig. 4.7 shows for instance the stage current detecting when milling a CuNi(17nm)/[Nb(20nm)/CuNi(17nm)]$_{15}$ multilayer grown in the UFO system of the Department of Materials Science in Cambridge, UK. One can clearly see and even count the interfaces in the structure from the stage current. The final drop corresponds to the reaching of the SiO_2 surface of the substrate and the following increase indicates the reaching of the SiO_2/Si interface.

After reducing the tracks on submicron-scale, finer nano-structures, as nano-constrains, can be created at high magnification and with very small (≤10 pA) beam currents. Fig. 4.8 shows for instance nano-bridges patterned from superconducting MgB_2 tracks to act as superconducting weak links. Notice how the rounding off can be confined to the spot size for thin films, allowing resolution < 10 nm.

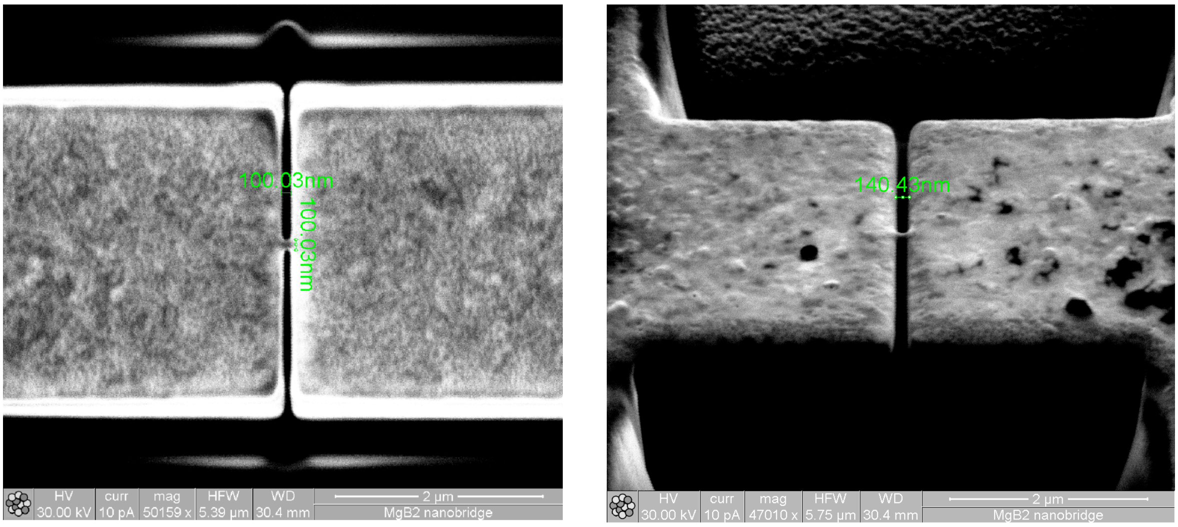

Fig. 4.8: *FIB images of* MgB_2 *nano-bridges taken from* $\theta = 0°$ *(left) and* $\theta = 52°$ *(right). The film was grown by C. Portesi at the "Istituto Elettrotecnico Nazionale" of Turin, IT.*

4.3 Three-dimensional FIB fabrication technique

To compliment the planar FIB technique discussed in Sec. 4.2, a three-dimensional technique for creating current-perpendicular-to-plane (CPP) devices has been developed. In the present work a technique already used by other authors [8,9] has been extended to produce tunnel spin-valve Josephson junctions.

Starting from a micro-patterned track, the track is narrowed down to submicron-size with 100 pA beam (Fig. 4.9 (top)) and the sidewalls are cleaned with 10 pA beam (Fig. 4.9 (bottom)). Notice that, unlike the case of CIP devices, the resputtering material deposited on the top layer of the structure is not a problem here, since the top layer is just a thick electrode layer (and moreover, in our case is superconducting while the resputtering material is not). The cleaning process here is needed to remove excessive Ga implantation and resputtered material from the lateral sidewalls, where the resputtered material acts as a short veil for the tunnel barrier.

This first two steps are identical to those performed to make CIP devices and the angle between beam and film normal is $\theta = 0°$.

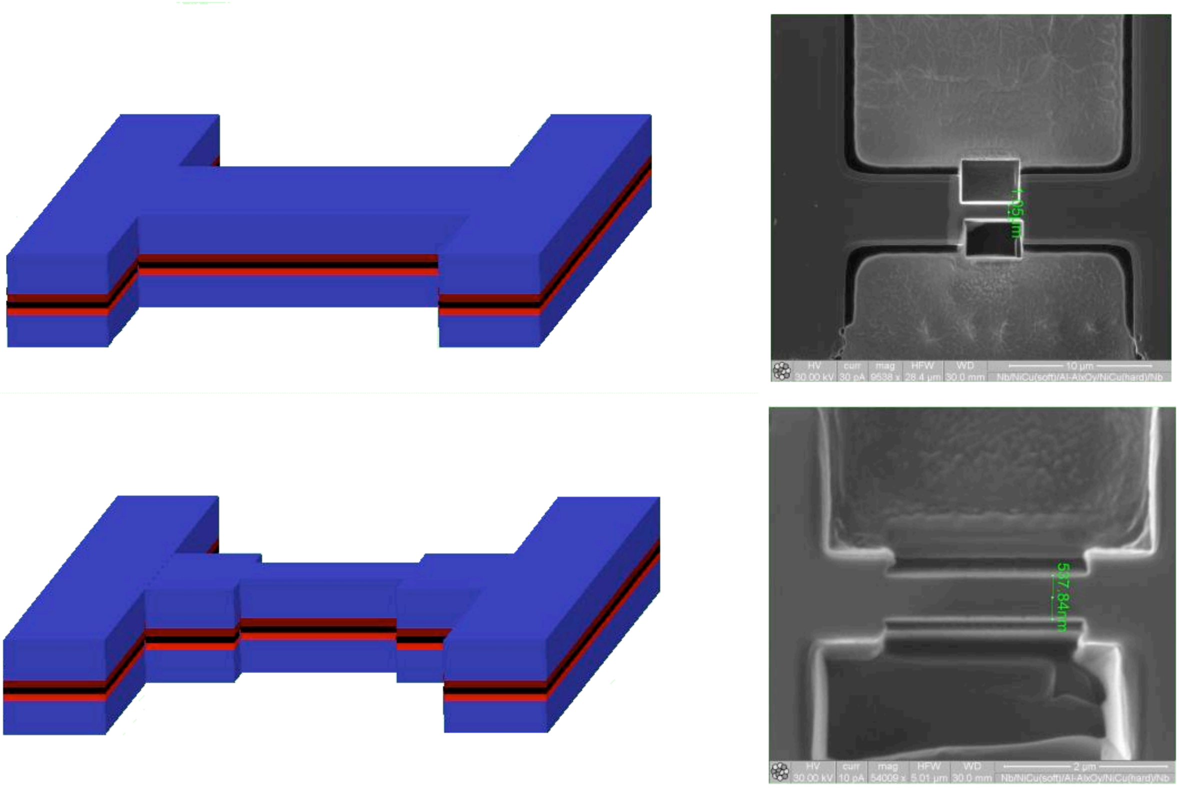

Fig. 4.9: *(top) Track narrowing with 100 pA beam and (bottom) cleaning of the sidewalls with 10 pA beam.*

The sample is tilted to $\theta = 85°$ in the way explained in Fig. 4.4. Notice that the sample is not tilted to $\theta = 90°$ to avoid grazing beam to be distorted or scattered in an uncontrolled manner. From $\theta = 85°$, two side cuts are made with 10 pA beam to force the current vertically through the TMR. When making the cuts, the stage current is monitored. When the milling goes through, a sudden drop in the stage current occurs. Fig. 4.10 shows the sample view from $\theta = 85°$, after the side cuts are made. The two side cuts will be referred to as the ‘undercut’ and ‘overcut’, respectively.

It must be noted that, since the current is injected and removed from the top electrode, there are in fact two junctions in series: the small junction, and a much larger one (on the right hand side of Fig. 4.10). This second device is much larger than the central one, and will have both a much smaller resistance than the first device and such a large critical current, in the case of superconducting devices, that it can be neglected.

The thickness of the device in the y direction is important. Since milling cannot take place at $\theta = 90°$, the overcut and undercut must mill into the top and bottom electrodes by $\Delta z = y\tan((\pi/4)-\theta)$ (see inset Fig. 4.10) to ensure that the isolation between the top and bottom electrodes is achieved. For instance, for $\theta = 85°$ and $y = 500$ nm, it must be $\Delta z \sim 44$ nm. This is limiting for the smallest thickness of topmost and bottommost layers. Fortunately, this outer layers are usually electrodes, and hence rather thick.

Moreover, the Gaussian beam profile makes the side-cuts not squared (see Fig. 4.11). This gives uncertainty on the junction lateral size, uncertainty that depends again on y: the smaller is the side-cut depth, the more squared is the junction.

The process as described so far is similar to that previously used to produce Josephson weak links. It has been demonstrated not to be suitable to produce tunnel junctions [5,6] for the reasons already discussed in Sec. 4.1.1. Post-anodization processes have revealed to be

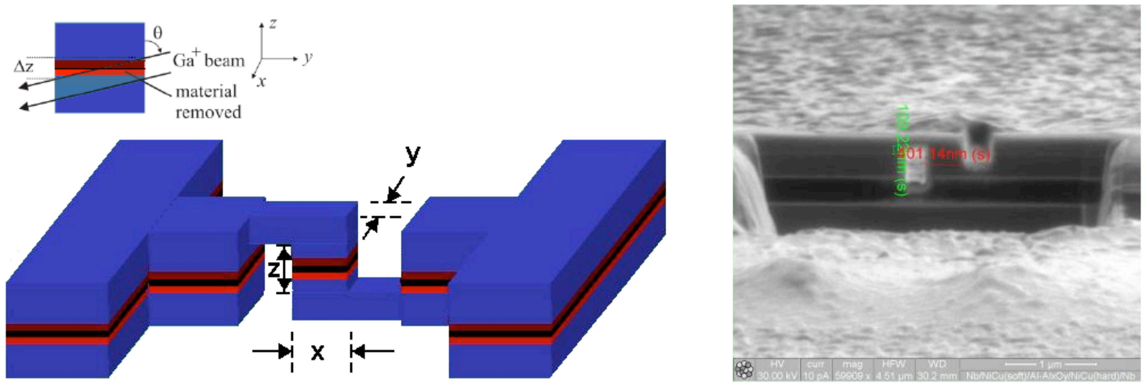

Fig. 4.10: *Isolation cuts made with 10 pA beam from $\theta = 85°$. Inset shows the effect of a milling from $\theta < 90°$.*

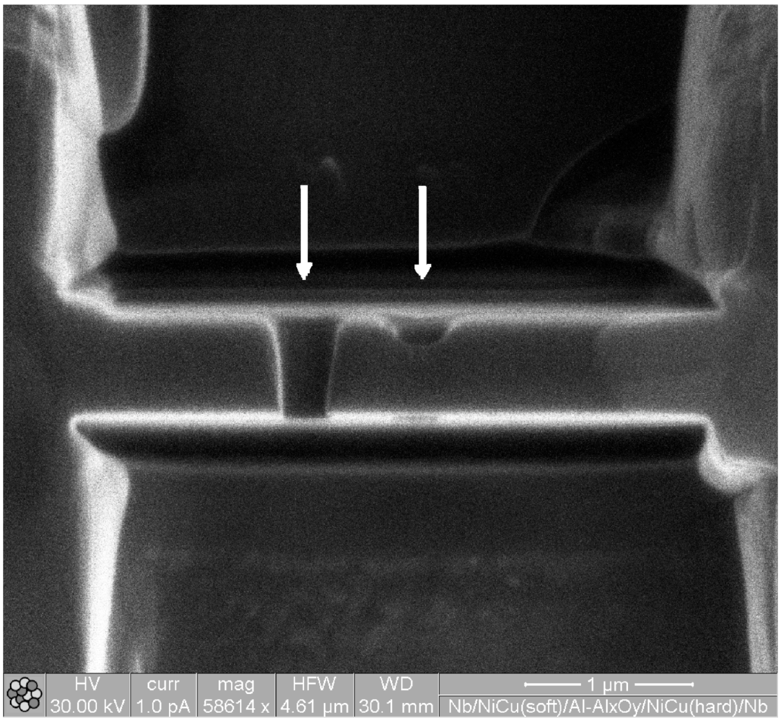

Fig. 4.11: *Effect of Ga beam profile.*

successful in removing the shorting veils [6], but one completely loses control on the device dimensions. In this work we have produced hysteretic Josephson junctions by simply cleaning the sidewalls with a very low beam current (1 pA). The alignment of such a small aperture is strongly sensitive to the sample position and much less stable than the others. By accessing to the maintenance program, the alignment procedure was performed for this aperture always before the post-cleaning. A cleaning of the side cuts was first performed close to the barrier from $\theta = 85°$ (Fig. 4.12 top) and then the sample was tilted back to 0° where the cleaning was performed on the lateral sidewalls (Fig. 4.11 bottom). When the cleaning from $\theta = 0°$ takes place, the previously cleaned side cuts are shielded from resputtering by the upper electrode. Notice (Fig. 4.11 bottom) that the post-cleaning from $\theta = 0°$ reduces the uncertainty on the junction x-dimension introduced by the Gaussian beam profile when making the side-cuts.

The efficiency of this process will be discussed in Sec. 5.3, where the current-voltage characteristics of the devices fabricated are presented and discussed.

Finally, it is worth pointing out how the FIB is a powerful tool for imaging, besides for patterning. Although slow scans risk damaging the observed sample, the images taken with the FIB are much brighter than those taken by SEM, because of the larger number of secondary electrons produced. An example of this is the picture reported in Fig. 4.13 (left). It shows one of the craters spontaneously formed on our samples when etching them with wet chemical etching.

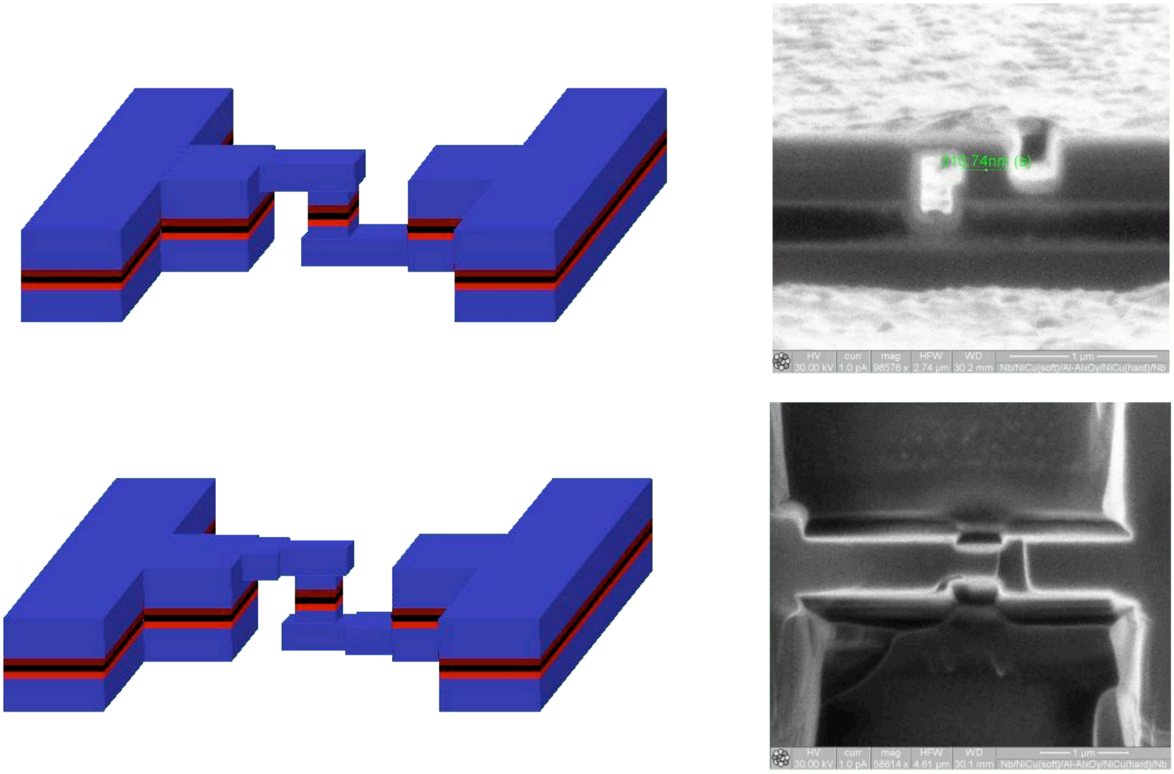

Fig. 4.12: *(top) Post-cleaning of the side-cuts close to the tunnel barrier and (bottom) post-cleaning of the lateral sidewalls with 1 pA beam current.*

Moreover, since the milling rate depends on the material, FIB tends to enhance the contrast between different elements, what with a SEM would require detecting of the small number of backscattered electrons with dedicated detectors. In Fig. 4.13 (right) is reported one of the junctions fabricated from a [Nb(20nm)/NiCu(17nm))$_7$ multilayer grown in Cambridge. The layers can be easily distinguished notwithstanding their small thickness.

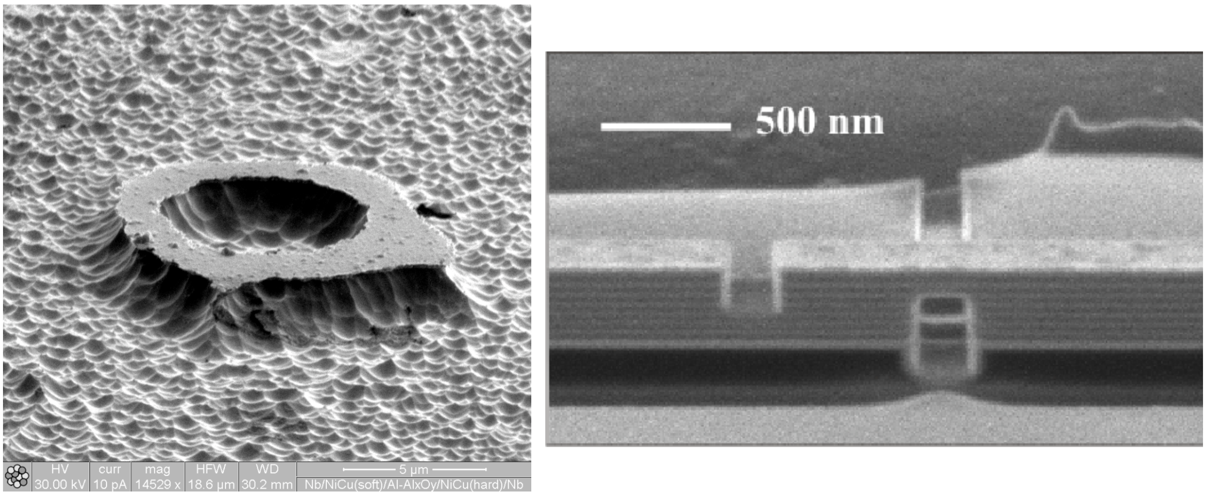

Fig. 4.13: *(left) FIB image of a spontaneously formed crater; (right) CPP device fabricated from a (Nb/NiCu)$_7$ multilayer.*

References

[1] J. Melngailis, *J. Vac. Sci. Technol. B* **5**, 469 (1987).

[2] A. J. De Marcoa and J. Melngailis, *J. Vac. Sci. Technol. B* **19**, 2543 (2001).

[3] J. Ziegler, J. Biersack, and U. Littmark, *The Stopping and Ranges of Ions in Matter* (Pergamon New York, 1985).

[4] C. Chappert, H. Bernas, J. Ferré, V. Kottler, J.-P. Jamet, Y. Chen, E. Cambril, T. Devolder, F. Rousseaux, V. Mathet, H. Launois, *Science* **280**, 1919 (1998).

[5] C. Bell, *PhD Thesis*, University of Cambridge, 2003.

[6] M. Watanabe, Y. Nakamura, and J.-S. Tsai, *Appl. Phys. Lett.* **84**, 410 (2004).

[7] *The Quanta 200 3D User's Operation Manual*, FEI Company (2004).

[8] S.-J. Kim, Y. I. Latyshev, T. Yamashita, and S. Kishida, *Physica C* **362**, 150 (2001).

[9] M. G. Blamire, *Supercond. Sci. Technol.* **19**, S132 (2006) and references therein.

Chapter 5

Results and discussions

The results for the fabricated devices are discussed. The issues related to the fabrication procedure are highlighted for each kind of devices considered.

5.1 CPP spin-valves based on manganite/ferromagnetic-metal bilayers

5.1.1 Motivation

In the room temperature ferromagnetic $La_{0.7}Sr_{0.3}MnO_3$ the dead layer at the surface (see Sec. 2.4.2) can extend to a depth of 6 nm. The thickness of this dead layer strongly depends on different parameters, among which the annealing time, the annealing temperature and even the kind of substrate used [1,2]. The coexistence of paramagnetic phase with insulating phase that usually occurs in manganites, as discussed in Sec. 1.2, suggests that, if the dead layer is magnetically inactive, it must be insulating, or at least highly resistive. Moving from this observation, Freeland et al. [3] have experimentally demonstrated that in the $n = 2$ perovskite $La_{2-2x}Sr_{1+2x}Mn_2O_7$, the dead layer is insulating. More recently, the existence of an insulating dead layer has been proved [2] in the room temperature ferromagnetic $La_{0.7}Ca_{0.3}MnO_3$ at the interface with Platinum (Pt). It is not clear whether the formation of this insulating barrier is localized in the topmost layers of the manganite or it must be rather ascribed to the oxidation of the metal close to the interface because of oxygen diffusing from the manganite [4,5].

This intrinsic insulating layer can be used as a tunnel barrier for the fabrication of high quality magnetic tunnel junctions. Moreover, in order to obtain a magnetoresistive device, the insulating nature of the dead layer is not mandatory. Unlike ferromagnetic metals, the thickness of the dead layer can be large enough to avoid magnetic exchange coupling between the manganite and a ferromagnetic counterelectrode deposited on it. Under this condition, the dead layer can be exploited as a natural spacer at the interface, whether it is insulating or not, to obtain magnetoresistive devices.

In this thesis we studied the magneto-transport properties of CPP pseudo spin-valves fabricated from $La_{0.7}Sr_{0.3}MnO_3/Ni_{80}Fe_{20}$ bilayers.

5.1.2 Films growth and structural characterization

$La_{0.7}Sr_{0.3}MnO_3$ (LSMO) films were provided by the "thin oxide films group" of the Dept. of Physics (University of Naples). The films were grown on (110) $SrTiO_3$ (STO) by rf magnetron sputtering from a single target at a temperature of 840°C and at an incident power of 100 W. The sputtering atmosphere was a mixture of argon (Ar) and oxygen (O_2), with equal partial pressures ($P_{tot} = 66$ Pa). The rate of deposition was 0.03 nm s^{-1}, as calibrated by low angle X-ray measurements and by a profiler. After deposition, the samples were left cooling down in 4.0×10^4 Pa O_2 atmosphere for 2 hours. The stoichiometry was checked by

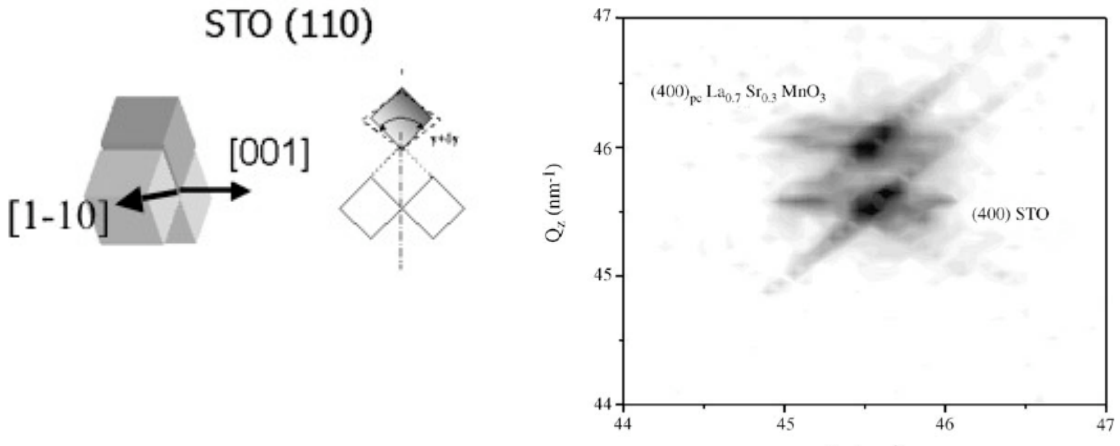

(a) (b)

Fig. 5.1: *(a) Sketch showing the elastic forces acting on a LSMO cell epitaxially grown on (110) STO. (b) Reciprocal space map around the (400) reflection. Courtesy of U. Scotti di Uccio [6].*

Rutherford backscattering analyses [6]. The X-ray diffraction measurements confirmed the cube-on-cube epitaxial growth that is typical of matched perovskitic films deposited on (110) STO. In the pseudocubic notation, the LSMO films have therefore the [110] direction perpendicular to the substrate plane, while the $[1\bar{1}0]$ and [001] lay in the substrate plane. All the specified crystal vectors are parallel to the homologous of STO. The quality of the crystal structure was confirmed by a full width at half maximum (FHWM) of the rocking curve less than 0.1°. The coincidence of the Q_x position for film and substrate in the reciprocal maps (Fig. 5.1) indicates the in-plane matching of the structure.

Polycrystalline $Ni_{80}Fe_{20}$ (Permalloy, Py) was dc-sputter deposited at room temperature in a separate system with base pressure $P_b = 1\times10^{-6}$ Pa and Ar atmosphere of $P_{Ar} = 0.5$ Pa. It was found to be fcc(111) textured. The rate of deposition was 0.1 nm s^{-1}. During the growth, a magnetic field of ~ 50 mT was applied in the plane of the film and along the easy axis of the underlying LSMO, in order to induce an easy axis for the Py in the same direction.

5.1.3 Magnetic characterization of the LSMO films

The magnetic properties of the films were studied by a Vibrating Sample Magnetometer (VSM). The Curie temperature was determined by measuring the magnetization vs. temperature $M(T)$ curves (Fig. 5.2). In Fig. 5.2 is also reported for comparison the measured resistivity vs. temperature $\rho(T)$. The Curie temperature was found to be always above the room temperature for films thicker than 15 nm.

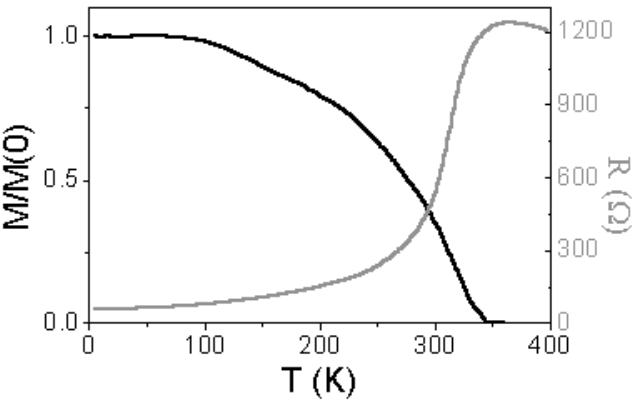

Fig. 5.2: *Magnetization vs temperature of a LSMO film 30 nm thick. A Curie temperature of 350 K can be estimated. The resistance vs temperature curve of the same film confirms the value of the Curie temperature.*

The thickness of the dead layer was estimated by using the “dead layer model” as explained in Sec. 2.4.2. An average layer thickness of ~ 4 nm was found.

Hysteresis loops *M*(*H*) were measured for several film thicknesses at different temperatures. We will focus here on the magnetic properties of 30 nm thick films, that were those used to fabricate the devices.

The films show an in-plane uniaxial anisotropy with the easy axis along [001] and hard axis along $[1\bar{1}0]$ (see Fig. 5.3a). This behavior is in agreement with that reported in other works [7,8] and is known to be due to the stress induced in the LSMO by the cubic (110) STO underlying substrate. The anisotropy constants can be estimated in the framework of the Stoner-Wohlfarth model, as explained in Sec. 1.4.7. Starting from eq. (1.4.41) and considering the external field applied along the hard axis ($\phi = 90°$), the equilibrium condition $\partial E/\partial \theta = 0$ for $H = H_S$ yields: $K(T = 100\ K) = \mu_0 M_S H_S / 2 = 2.7 \times 10^4$ J/m^3 with $H_S = 100$ mT saturation field in the hard direction. In terms of the magnetostriction constant λ and strain ε,

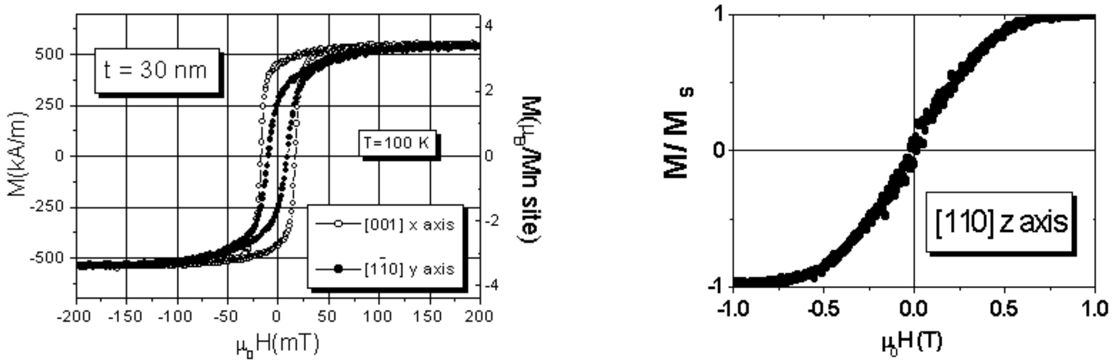

Fig. 5.3: *Magnetization vs. field applied along (left) the in-plane [001] easy, in-plane [1-10] hard and (right) out-of plane [110] axes at T = 100 K for a film 30 nm thick of* $La_{0.7}Sr_{0.3}MnO_3$ *grown on (110)* $SrTiO_3$.

the induced anisotropy can be written as [9] $K_{stress} = 3\lambda\varepsilon Y/2$ where Y is the Young's modulus. Assuming [10] λ (T = 100 K) = 2.2×10^{-5} and [11] $Y = 5 \times 10^{11}$ N/m^2 yields ε = 0.8 %, which, according with the data reported in Tab. III.1, corresponds to the film/substrate lattice misfit.

The M(H) loop with field applied along the direction [110], *i.e.* perpendicular to the film plane, is shown in Fig. 5.3b for the same film. The measured anisotropy field of H_K ~ 0.7 T is equal to the demagnetizing field of 0.69 T within less than 2% of accuracy. The agreement indicates that, to within 2.7×10^2 J/m^3, there is no perpendicular uniaxial anisotropy.

5.1.4 Magnetic characterization of the LSMO/Permalloy bilayers

The devices were fabricated from bilayers LSMO(30nm)/Py(10nm). The M(H) loop of the bilayer (Fig. 5.4a) does not show a double coercivity at room temperature. This is because the coercive filed of the LSMO is close to that of the Py at this temperature. When the temperature is lowered down to T = 4.2 K, the coercive field of the manganite increases more than that of the metal, revealing the double coercivity behavior of the bilayer.

The separation between the LSMO and the Py loops in the bilayer is not obvious because of the smaller thickness of the Py compared with that of the LSMO. By subtracting the *M(H)* loop of the LSMO alone from the *M(H)* loop of the bilayer (inset Fig. 5.4b), a coercivity of 3.6 mT for the Py in the bilayer is estimated. This value is not far from a coercivity value of 3.2 mT measured on a Py film of the same thickness at 4.2 K (Fig. 5.4c).

Yet, the sharpness of the Py loop in the bilayer is smoother as compared with that of the Py layer alone. This is likely to be due to magnetostatic "orange peel" coupling as confirmed by a roughness of ~ 1.0 nm as measured by Atomic Force Microscopy (AFM) on a single LSMO layer of the same thickness. The consequence of the smooth reversing of the Py magnetization is that the antiparallel (AP) configuration is not well-established.

5.1.5 Magneto-transport characterization of the LSMO films

In order to exclude any possible misinterpretation on the magneto-transport data on the CPP devices, we checked the value of the AMR of our samples. This is because AMR is known to strongly increase in polycrystalline LSMO films (up to 15%) because of spin-dependent scattering of polarized electrons at the grain boundaries [12]. Although our X-ray analyses, performed before and after the deposition of Py, indicate a high degree of epitaxy of the LSMO films, we measured the AMR in our films for a double check.

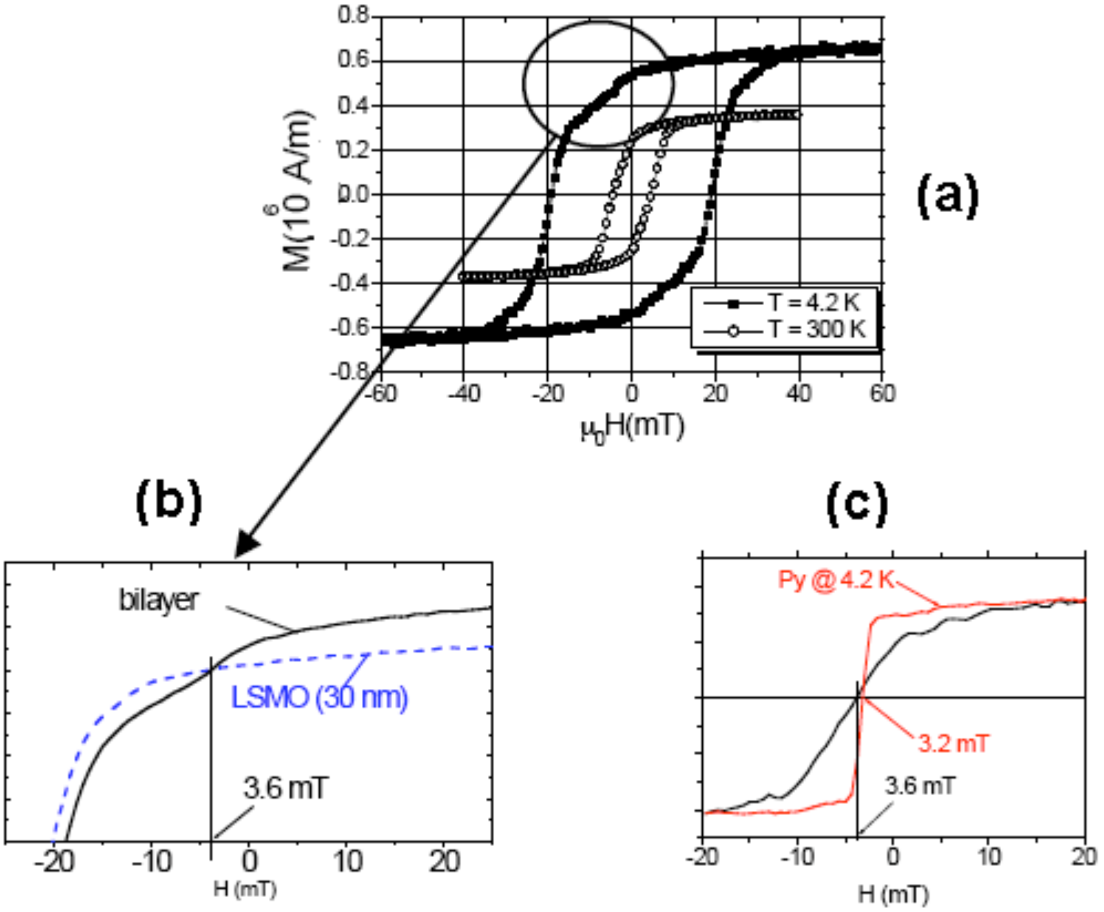

Fig. 5.4: *(a) M(H) loop of a LSMO(30nm)/Py(10nm) bilayer. At 4.2K the bilayer shows its double coercivity behavior. (b) The coercivity of the Py in the loop is estimated by subtracting the M(H) loop of the LSMO alone from the M(H) loop of the bilayer. (c) the coercivity of the Py in the bilayer is not far from that of the Py alone but the loop extracted is smoother, suggesting orange peel coupling in the bilayer.*

A LSMO film was patterned employing a standard photolithography resist definition and Ar^+ ion milling film into 100 μm wide, 500 μm long tracks parallel to the easy magnetization axis (Fig. 5.6a). Fig. 5.6b shows the current in-plane (CIP) *R(H)* curve measured with field applied parallel and perpendicular to the tracks. MR_{max} was always smaller than 0.3% as expected [12].

5.1.6 Magneto-transport characterization of the LSMO/Py bilayers

The CPP MR of the bilayer as a function of an external applied magnetic field was measured at $T = 4.2$ K (Fig. 5.7b). Part of the LSMO surface was preserved uncovered for contacts by resorting to a shadow mask during Py deposition. Four contacts were wire-bonded in line with the easy axis of magnetization. The external magnetic field was applied in the same direction. The measurement configuration is shown in Fig. 5.7a. *R*(*H*) shows hysteresis

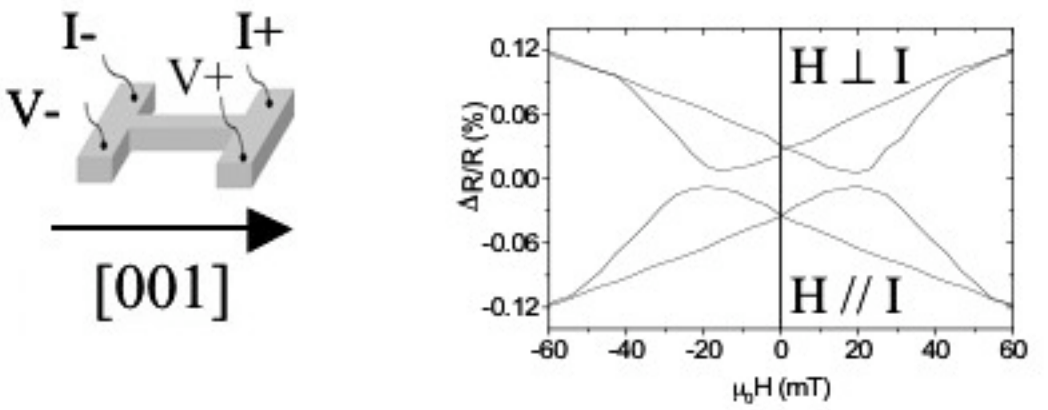

(a) **(b)**

Fig. 5.6: *CIP-R(H) measured at T = 4.2 K for a 30 nm thick, 100 μm wide and 500 μm long track of $La_{0.7}Sr_{0.3}MnO_3$ with field applied parallel and perpendicular to the current direction. The measurement configuration is also shown.*

with maximum peaks corresponding to the coercivity of the LSMO. It is not dependent on the bias current, in agreement with the measured linear changing of the voltage (*V*) with the current (*I*). The maximum change in resistance, measured as $MR_{max} = -\Delta R/R_{H_C} = -(R(60mT)-R(H_C))/R(H_C)$, where H_C is the coercivity of the LSMO, is 1.7%. The measured magnetoresistance cannot be attributed to the anisotropic magnetoresistance (AMR) effect of Py, even though values of the order of 1% can be achieved for this material, because in this case the maximum would have occurred at the coercivity of the Py in the bilayer. Moreover, the observed MR_{max} is too large to be attributed to the single LSMO layer, as demonstrated in the previous section.

Yet, if the bilayer were behaving as a spin valve, an abrupt increasing of resistance should take place at the coercivity of the Py, whilst the increasing of it is smooth everywhere. Also,

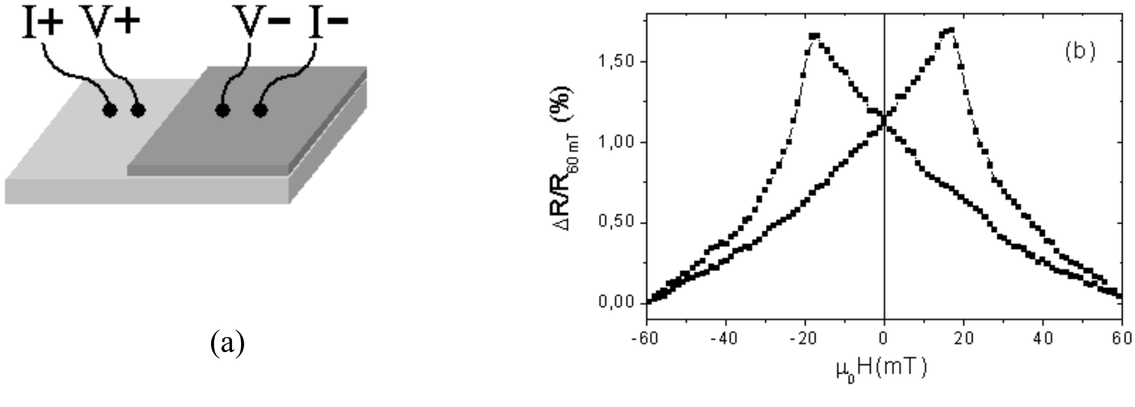

(a)

Fig. 5.7: *CPP-R(H) measured at T = 4.2 K with field applied along the in-plane [001] easy axis for a bilayer $La_{0.7}Sr_{0.3}MnO_3$ (30nm)/Py (10nm). The measurement configuration is also shown.*

R(*H*) should saturate and reach a minimum in correspondence with the saturation field of the *M*(*H*) loop of Fig. 5.4a. The abrupt increase of resistance could be concealed by two effects. One is the previously discussed AMR effect. The other one is the not well-established AP configuration as suggested by the *M*(*H*) loop. If the AP state is not well established, the reversing of the LSMO magnetization starts taking place when the Py magnetization has not saturated yet. As a consequence, the change of resistance is smaller and smoothed.

The AMR effect is easily suppressed by fabricating planar junctions.

5.1.7 Magneto-transport behavior of the LSMO/Py planar junctions

Planar junctions were fabricated by processing the bilayer with a two-step lithography process. The bilayer was first patterned by Ar^+ ion milling into tracks 100 μm wide and 500 μm long with the associated connections and contact pads. The areas of the square junctions were defined in correspondence of the tracks by a second photolithographic step and milling of the uncovered Py. The etching rate of the layers had been previously calibrated to stop the milling at a few nm below the bilayer interface. The final configuration is shown in Fig. 5.8a. The four contact measurement configuration allows the resistance, and hence the AMR of the wiring, to be suppressed. Moreover, the direction of the current is better defined in the patterned devices. We fabricated junctions with area ranging from 30 × 30 μm^2 to 100 × 70 μm^2. Fig. 5.8b shows the CPP-*R*(*H*) for a 100 × 70 μm^2 junction. The shape is typical of a pseudospin-valve device with a flat baseline. Moreover, increasing *H* from the negative lowest field value, the resistance does not change smoothly but an abrupt changing occurs around the zero field value. This is reflected in a value of resistance at zero field which is

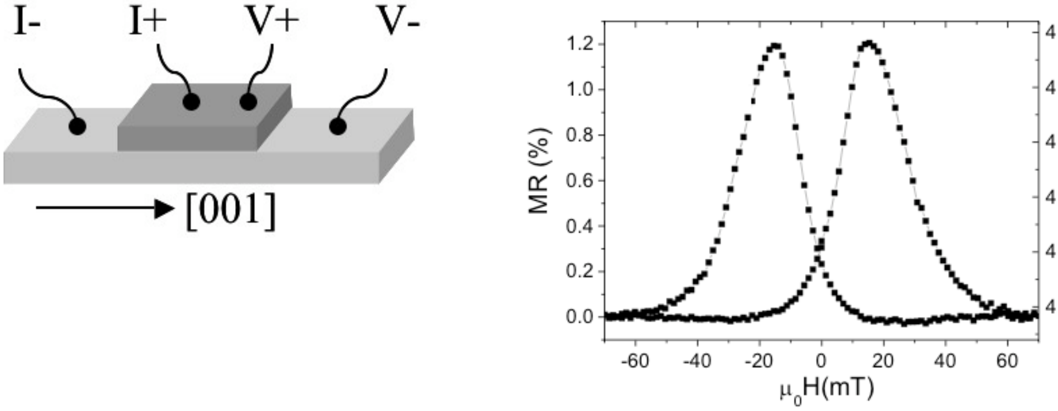

(a) (b)

Fig. 5.8: *CPP-R(H) at T = 4.2 K of a junction with area 100 × 70 μm². The magnetic field was applied along the in-plane [001] easy axis. The measurement configuration is also shown.*

much closer to the minimum value compared to the cases of Figs. 5.6 and 5.7. The change of resistance between the maximum value and the zero field value, $MR_0 = (R_{max}-R(0mT))/R(0mT)$, is 0,95% compared to a change of MR_{max} = 1.2% as referred to the minimum value. The mismatch between MR_0 and MR_{max} is consistent with a not well-established AP state as suggested by the $M(H)$ loop.

It is important to notice that the CPP resistance measurements are not affected by problems due to inhomogeneous current distributions that are known to give rise to large apparent MR ratios [13]. This effect occurs for junctions with resistances of the electrodes (in the junction area) comparable or higher than the junction resistance. For the largest of our junctions (worst case), the junction resistance is $R_J = 571\ \Omega$, whereas the square resistances of the electrodes are $R_{LSMO} = 40\ \Omega$ and $R_{Py} = 16\ \Omega$ corresponding to resistivities measured to be $\rho_{LSMO} \sim 1.2 \times 10^{-6}\ \Omega m$ and $\rho_{Py} \sim 1.6 \times 10^{-7}\ \Omega m$ at 4.2 K. The ratio R_j/R_{lead} is 14.2 for the largest junctions and greater than 100 for the smallest ones. Such ratios (see Fig. 3 of Ref. 13) rule out any contribution from the magnetoresistance of the electrodes and any geometrical effect.

The change of MR is much smaller than that predicted by the Jullière's model for tunneling junctions. On the other hand, it has been widely demonstrated [14] that the Jullière's model does not apply to ferromagnetic metal/insulator/LSMO junctions. Moreover, the amplitude of the MR ratio, and even its sign, depend on the choice of the tunnel barrier. De Teresa et al. [14] have observed that, if the insulating barrier is a lattice matched epitaxial oxide ($SrTiO_3$ or $Ce_{0.69}La_{0.31}O_{1.845}$), the MR ratio is negative ($R_{AP} < R_P$), whereas it is positive ($R_{AP} > R_P$), but much smaller than that predicted by the Jullière's model, when the barrier is a metal oxide. This seems to suggest that in our devices, if an insulating barrier is present at the interface, it is formed in the metal layer because of oxygen diffusion from the manganite. The low value of MR in our devices can be partially ascribed to a large boundary resistance that masks the effect. In LSMO/metal heterostructures, the series of bulk resistances and interface resistances through which the transport is not spin dependent inevitably reduces the measured change of MR. Particularly when normal metal layers are used as electrodes, the total resistance can be as high as to completely mask the MR effect [15]. In our devices the two ferromagnetic layers are themselves the electrodes of the junction. Therefore, only the resistance at the interface between the two ferromagnetic layers plays a role. Yet, this resistance is still rather large. This suggests an insulating nature of the topmost part of the magnetic dead layer. The effect of the dead layer on the reduction of the MR is then twofold. While the metallic part of the dead layer works as a spin scattering region, the non-metallic one provides disordered spins at the interface that contribute to the spin depolarization. A reduction of the dead layer thickness, and in particular of the non-metallic region of it, could increase the MR. This reduction is limited by the necessity of keeping the layers magnetically decoupled.

Anyway, during this work we demonstrated for the first time the possibility of using the dead layer of a manganite as an intrinsic spacer. A suitable choice of the dead layer thickness could allow the fabrication of devices with high MR ratio in which any metal or insulating deposited spacer is needed.

5.2 CIP planar artificial spin-valves

5.2.1 Motivation

The common expectation of a forthcoming mass production and marketing of magnetoresistive random access memories (MRAMs) have been unmet, so far. As already discussed in Sec. 2.4.4, the main reason of it is the impossibility of increasing the bit density because of the fast increasing of the cross-talk error probability with the reduction of the distance between nearest neighbor bit cells. The magnetization reversal of the soft layer in tunneling magnetoresistive (TMR) cells through a spin polarized current requires rather high current densities to take place. Thus, while removing any risk of cross-talk, the high integration density is now limited by the power dissipation.

More promising for digital applications seem to be those systems in which the magnetic configuration is defined by domains separated by domain walls (DWs). The two ingredients to make devices out of these systems is to make the wall provide an additional resistance, so to permit the read-out, and the possibility to displace the wall through a current, i.e. write information. In Secs. 1.5 and 2.3 we have seen how to make a wall give a resistance contribution, while in Sec. 2.4.5 we have discussed how walls can be displaced by a current. These concepts have been used in this work to make planar artificial spin-valves. We chose to use LSMO as a starting material in order to exploit its high polarization and hence achieve a sensible MR with relatively thick DWs.

5.2.2 Fabrication process

We chose to use (110)-oriented substrates in order to exploit the stress induced in-plane anisotropy that makes the hysteresis loop sharper along the [001] easy axis.

The films were patterned into 5 μm wide, 100 μm long tracks parallel to the easy magnetization axis (Fig. 5.9a) by standard UV lithography and Argon (Ar) ion milling. The pattern provides any track with connections and contact pads for standard four-points current-voltage and resistance measurements. The samples were then processed in the Quanta 200 3D. The tracks were narrowed down to 500 nm from an angle of $\theta = 0$ with a beam current of 10 pA to achieve nano-bridges 3 μm long (Fig. 5.9b). The sidewalls of the nano-bridges were then cleaned with a beam current of 1 pA. The aspect ratio (3 μm × 500 nm) of the narrowed bridges was chosen so to have pinning effect by shape anisotropy after the patterning with 1 pA beam current of two constrictions 30 - 50 nm wide at the bridge borders (Fig. 5.9c).

The scanning electron microscope (SEM) images of the constrictions (Fig. 5.9d) indicate that the rounding off due to the Gaussian profile of the FIB beam can be confined within a few nm for films with thickness up to 100 nm if a spot size of 7 nm (corresponding to 1 pA beam current) is used.

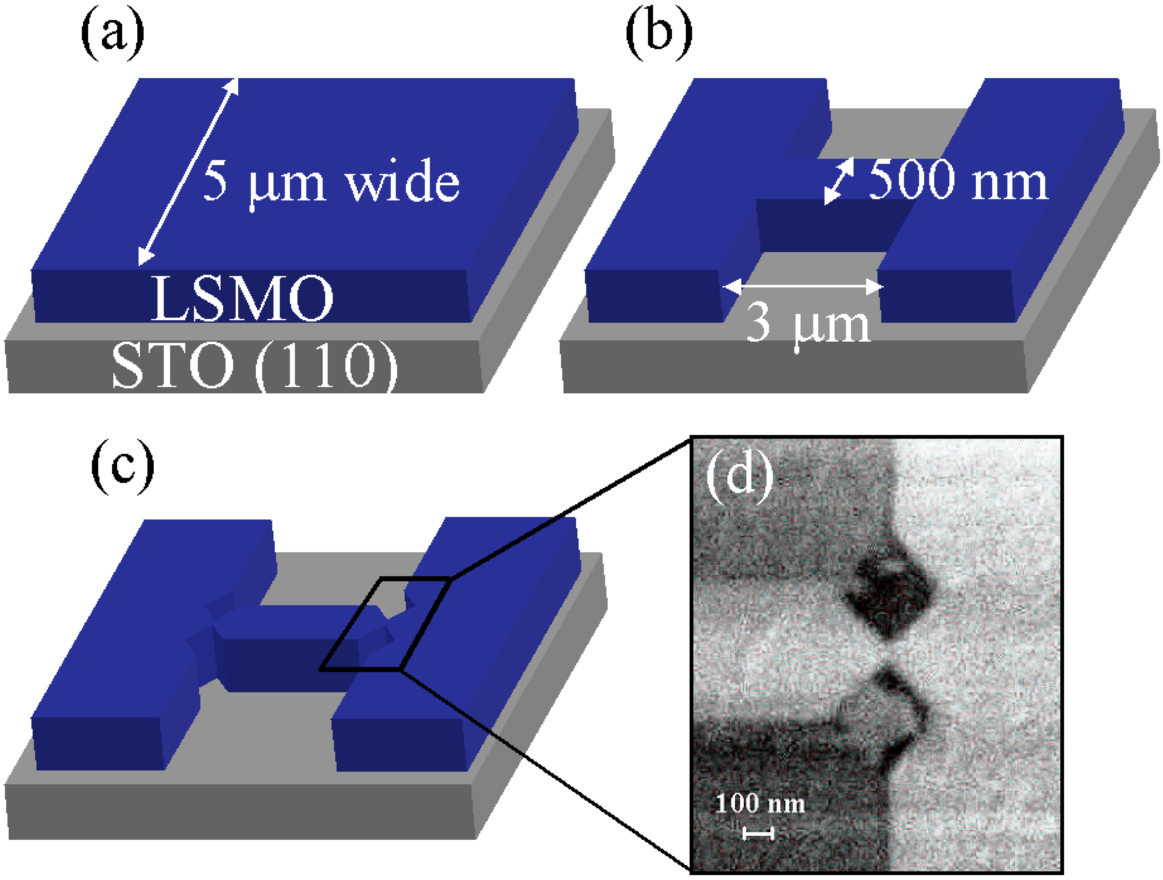

Fig. 5.9: *Schematic of the fabrication process: (a) Argon ion milling of 5 μm wide tracks; (b) FIB milling of 3 μm long, 500 nm wide bridges; (c) FIB milling of nanoconstrictions at the bridge borders; (d) SEM image of a patterned nano-constrain.*

5.2.3 I-V characteristics

The devices with 30 nm wide constrains showed a strong non-linearity in a wide range of temperatures (Fig. 5.10a). The shown curves are those recorded after negative saturation and in absence of external field (low-resistance state). This means that the non-linear shape of the *I-V*s is not due to a pressure effect exerted by either the bias current or the external field over DWs pinned at the nano-constrains. Non-linear *I-V* curves are quite common in nano-constrains obtained by FIB milling of either magnetic oxides [16,17] or magnetic diluted semiconductors [18,19]. Moreover, the plot of $\ln(I/V^2)$ vs V^{-1} (Fig. 5.11b) gives a negative slop at high voltage for all the temperatures in the range 4.2 K - 77 K. This behavior is typical of a device working in field emission regime. This regime can be induced in LSMO nano-constrictions by making a current of the order of 10^{12} A/m passing through [17]. The current is able to displace material out of the constriction, changing it into a nanogap. This is not our case for the following reasons:

(i) In the field emission regime, the voltage threshold in the *I-V*s must be of the order of the work function, which is ~ 4.5 V [20] in LSMO. In our constrictions, the threshold is always smaller than 1 V (on each constriction).

(ii) In LSMO, the changing of the work function with the temperature is ~ 0.4 meV/K [20]. This is not consistent with the change of voltage threshold with the temperature in our devices.

(iii) In the field emission regime the dependence on the applied magnetic field disappears in LSMO constrictions [17], while we measure a MR well above the

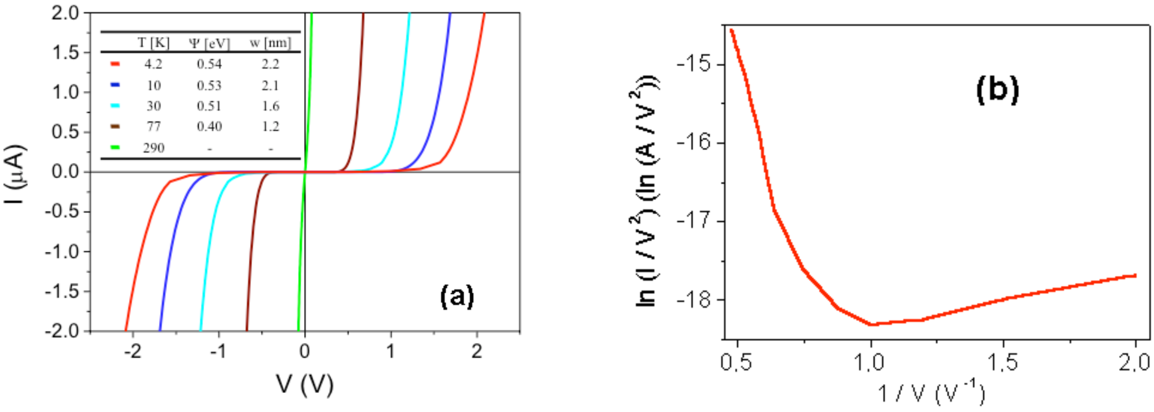

Fig. 5.10: *(a) I-V characteristics measured on a device with 30 nm wide constrictions in the low resistance state at different temperatures. Upper left inset reports the fitting parameters by eq. (5.2.1). (b) The Fowler-Nordheim plot at T = 4.2 K.*

onset of the regime.

(iv) The *I-V*s could be reversibly cycled many times.

(v) We were able to irreversibly change the *I-V*s by applying much higher currents.

Yet, the devices behave as a thick tunnel barrier is somehow formed and a bias voltage higher than the barrier height has to be applied to make a current flow. The height and width of this barrier can be determined by fitting the *I-Vs* with the Fowler-Nordheim model [21]:

$$J = \frac{e^3}{8\pi h}\frac{1}{\psi}\left(\frac{V'}{w}\right)^2 \exp\left(-\frac{8\pi\sqrt{2m}}{3eh}\frac{w}{V'}\psi^{3/2}\right) \tag{5.2.1}$$

where J is the current density, e is the electron charge, h is the Planck's constant, m is the electron mass, ψ and w are the barrier height and width, respectively. In eq. (5.2.1), V' is the voltage drop on each of the constrictions, i.e. $V' = V/2$ if V is the voltage drop measured on the devices. The best fitting parameters are reported in Fig. 5.10a (upper left inset). As expected, ψ is not consistent with the work function of LSMO.

The devices with nominal 50 nm wide constrictions showed instead only a very weak non-linearity at very low temperatures (Fig. 5.11), that was visible, in the range of applied currents, only by looking at the differential conductance as a function of the voltage (*dI/dV-V*).

5.2.4 TRIM calculations

In order to shed light on the origin of the tunnel barrier we performed TRIM calculations by using the public software *SRIM* [22].

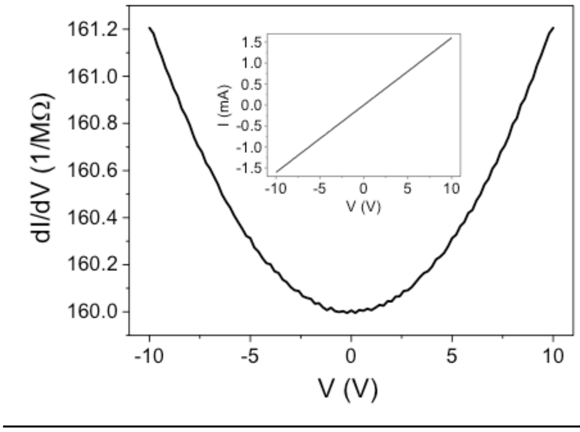

Fig. 5.11: *I-V and dI/dV–V characteristics measured on a device with 50 nm wide constrictions in the low resistance state (T = 4.2 K).*

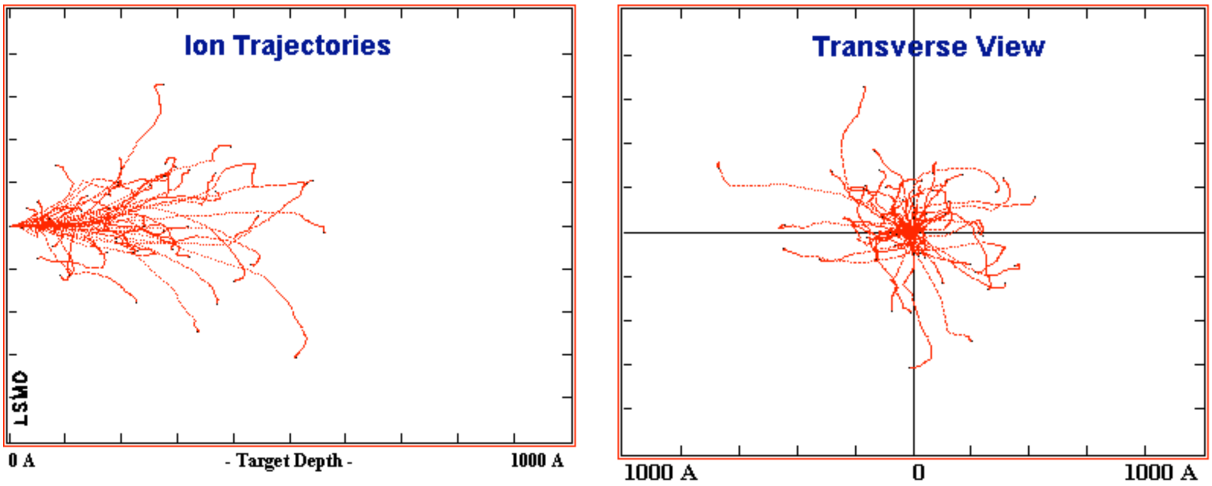

Fig. 5.12: *Results of the TRIM calculation: 50 Ga$^+$ ions collide with a 100 nm thick LSMO film at 30 keV.*

Fig. 5.12 shows the lateral and transverse view of the trajectories of 50 Ga$^+$ ions colliding with a 100 nm thick LSMO film at 30 keV energy. The lateral straggling converges to a value of about 12 nm when increasing the number of ions. This value can be considered underestimated, because the calculations do not take into account the spot size and the gaussian profile of the Ga beam.

Moreover, the calculations show that the number of oxygen vacancies left behind by the Ga ion travelling into the target (Fig. 5.13) is significatevely higher than those of the other elements (for instance the ratio between O- and Sr-vacancies is about 10). This means that the Ga irradiation is very efficient in breaking the Mn-O-Mn chains, which are responsible of electron conduction and ferromagnetic coupling in manganites. In other words, as in the case of normal metals, a low dose Ga irradiation is able to drive locally the material from ferromagnetic to paramagnetic, even if the dose is low enough not to be detectable by Energy

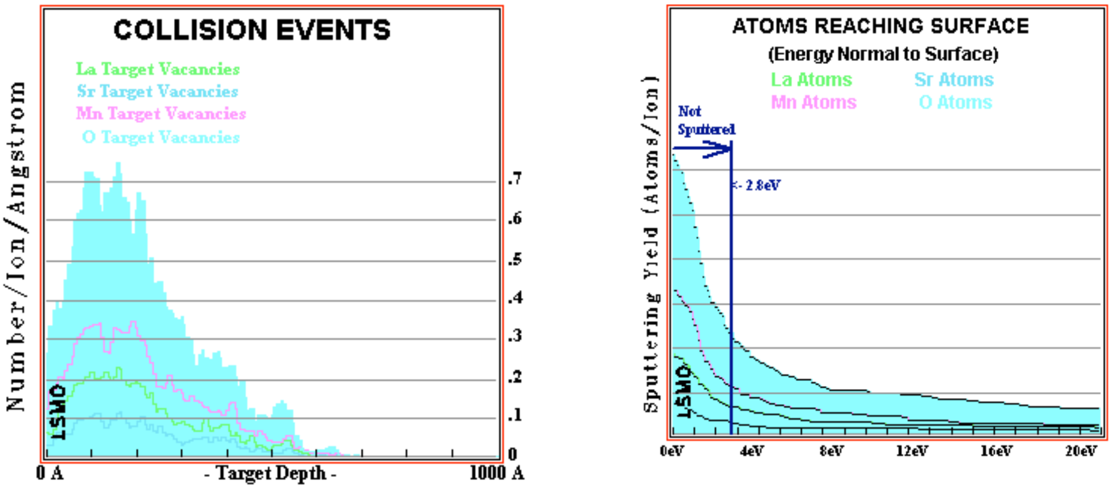

Fig. 5.13: *Collision events of Ga ions at 30 keV with La Sr Mn O atoms and number of atoms reaching surface per colliding Ga ion.*

Dispersive X-ray analyses. But, in the case of manganites, this means driving the material out of the metal phase. In a manganite constriction, when the width is about twice the Ga lateral straggling, an insulating barrier is formed and the conduction is by tunnelling. On the other hand, the unique feature of coexistence of paramagnetic and insulating phase makes manganites the best candidate for studying DWMR in FIB-milled nanostructures. In fact, in normal metal nano-constrictions the over-irradiated paramagnetic borders would short and hence hide, or at least strongly reduce, the contribution to the resistivity of the constrained DW. On the contrary, in manganite-based constriction, the paramagnetic border, although thicker, will be highly-resistive. This assumption is confirmed by the detectable MR in 50 nm wide constrictions (see following section). For such large constrictions (and hence large DWs) no contribution to the resistivity of the DW should be detected. If a MR is detected, the lateral width of the constriction must be smaller than the nominal physical width and the irradiated border must be highly-resistive. This also consistent with the linear *I-V* shown by 50 nm wide constrictions. The weak non-linearity at very low temperatures in these constrictions could be due to spin excitation of magnons [23] or presence of regions with reduces Hund's coupling near the over-irradiated borders.

5.2.5 MR measurements

Fig. 5.14 shows a typical resistance versus magnetic field *R(H)* recorded at $T = 4.2$ K and with low bias current (2 μA). Starting from $H = -60$ mT, the resistance has a sharp increase at $H_r = +20$ mT, which is the measured coercive field of the unpatterned LSMO film. This first phase corresponds to the reversing of the magnetization in the regions outside the central bridge, the latter having higher reversing field because of the geometrically induced shape anisotropy. The sharpness and the amplitude of the increase of *R* confirm that two DWs have

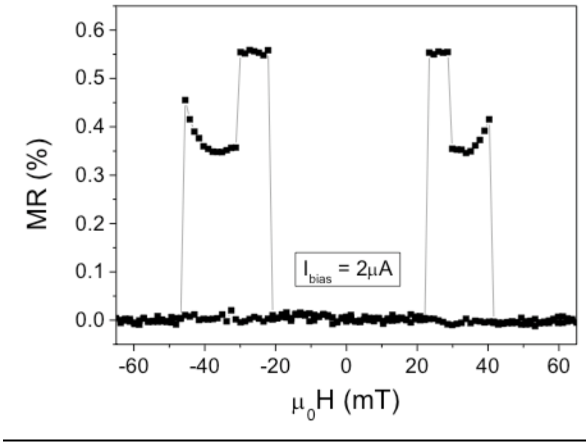

Fig. 5.14: *MR of a device with 50 nm wide constrictions measured at T = 4.2 K.*

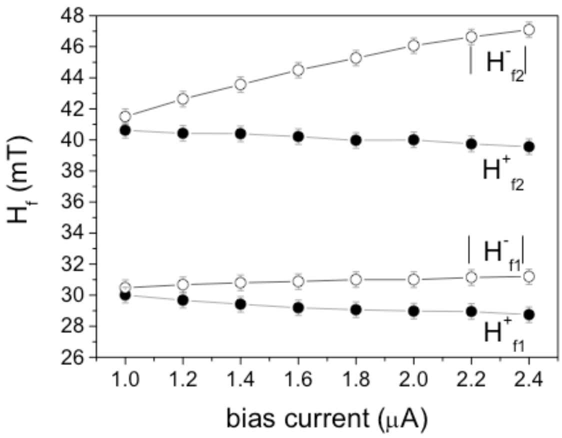

Fig. 5.15: *Switching field vs. bias current. The switching is assisted or hindered by the polarized current.*

been pinned at the nano-constrictions and are responsible of the detected change of *R*. In fact, as far as the amplitude of the change is concerned, it is too large to be attributed to anisotropic magnetoresistance (AMR), which is measured to be, in the field of interest, 0.1% in our films (see Sec. 5.1.5). Moreover, the AMR effect in epitaxial films is smooth and lacking of switching features.

This increase is followed by two decreases. This behavior is due to multi-domain configuration in the bridge. The bridge is too long to form single domain, and hence the reversing of magnetization in the bridge occurs by propagation of one of the two previously annihilated DWs. During this phase, the device can be seen as a series of two spin valves, one of which has switched in the low resistance state.

The values of the switching fields change with both sign and amplitude of the bias current (Fig. 5.15). When the field has the same direction of the electrons flow, the dropping fields decrease with the increase of the bias current, whereas they increase when field and electrons flow act against each other. Unambiguously, the depinning of the DWs is assisted (or hindered) by the bias current.

5.2.6 DW motion

A DW displacement in absence of external field can be observed when applying larger current densities. We used the following protocol to trap two DWs at the constrictions. The sample was negatively saturated by applying –100 mT field. The field was then swept up to 30 mT and back to zero to reverse the magnetization in the connecting arms. This procedure sets the device in the high resistance state. Then an electrical current was swept up to 1.5 mA and back to zero. The current was able to induce the first switch in the device (depinning of one of the two DWs), as detected by measuring the differential conductance vs bias current *dI/dV* (*I*) (Fig. 5.16). The depinning current density was $J = 1.6 \times 10^{11}$ A/m as calculated assuming the nominal lateral width. The second switch needs the application of a negative current of the same value to take place.

The DWs in our devices are trapped between two regions with different in-plane anisotropy. As discussed in Sec. 2.4.5, an external field is more efficient in moving the wall towards the region with lower anisotropy (i.e. lower coercivity) rather than towards that with higher anisotropy. Moreover, when pushing the DW towards the region with high anisotropy, a pressure is exerted on the wall (until depinning takes place) that produces an upturn in the *R*(*H*) like that observed in Fig. 5.14 after the depinning of the first DW.

When the force is exerted by a polarized current, if the acting mechanism is spin transfer torque (thick walls), the situation is not much different. As described in Sec. 2.4.5, in case of Bloch walls, the key parameter in determining the threshold current density and velocity of the wall is the out of plane anisotropy constant K_{out}. This is because, if ϕ_0 is the angle between spins at the wall center and the easy plane, below a critical value the force exerted on ϕ_0 by the electrons passing through the wall is balanced by the anisotropy and not efficient in dragging the wall, whether it is pinned or not. In case of thin films (that do not show perpendicular magnetic anisotropy), where the walls lay mainly in the plane, the in-plane anisotropy has to be the key parameter. The scenario is indeed much more complicated since, in the presence of the spin torque, the magnetization of the DW is no longer confined in the plane of the film [24] and then the threshold current density must depend on both the out of plane and in plane anisotropy constants.

In our geometry, the ratio between the transverse effective anisotropy constants related to the bridge (*b*) and the connecting arms (*ca*) is $K_\perp^b / K_\perp^{ca} = 4.1$, where the shape contribution in $K_\perp$ is calculated in the limits of the *Stoner-Wohlfarth* model and rectangular prism geometry

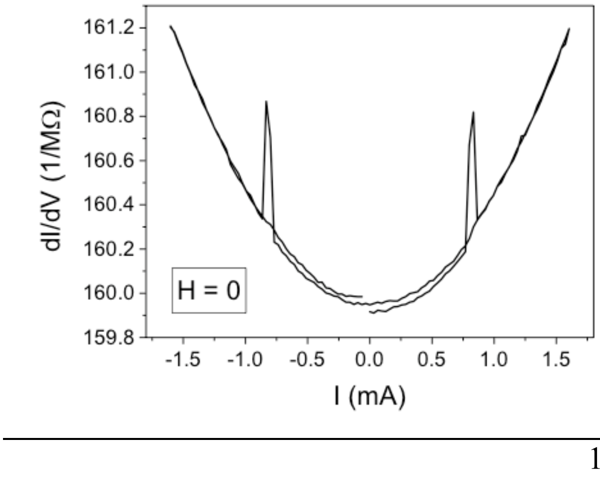

Fig. 5.16: *dI/dV-I at T = 4.2 K for a device with 50 nm wide constrictions after trapping DWs at the constrictions and in absence of external field. The peaks correspond to the depinning of the DWs.*

[25] and the magnetostrictive contribution has estimated to be $K = 2.7 \times 10^4$ J/m^3 in our films (see Sec. 5.1.3). It must be considered that, given the acicular shape of the central bridge, this ratio is underestimated. This means that a force is more efficient in depinning the DW that is pushed in the connecting arms rather than that being pushed towards the bridge.

In this framework, we can now explain the result shown in Fig. 5.14. When the bias current is increased the sharp change of dI/dV must be due to the depinning of the DW that is forced towards the connecting arm. A much larger current (as large as to produce irreversible changing in the I-V) would be required to depin the DW forced towards the central bridge. While sweeping back the current, nothing happens at $I = 0.8$ mA but a second sharp change is detected at $I = -0.8$ mA that must correspond to the depinning of the second DW being pushed towards the other connecting arm.

It is important to notice that, unlike switching due to spin torque in MTJs, the biasing current do not need to completely reverse the magnetization of the free electrodes. As soon as the wall is pushed away from the constriction, the resistance will drop, the wall surface (energy) will increase and the current density will decrease. As a consequence, the current will no longer be able to move to wall that remains close to the constriction.

Finally, we want to point out that the geometry of our devices rules out other mechanisms for current-induced DW motion. Hydromagnetic drag force (see Sec. 2.4.5) can be ruled out because it arises from the Hall effect and thus neither significant in thin films nor depending on the direction of electrons motion. The maximum oersted field induced by the threshold current in absence of external field is 6 mT, which is enough smaller as compared with the coercivity of the unpatterned LSMO film. Of course the transverse component perpendicular to the wall is smaller than 6 mT. Moreover, the magnetic configuration in the high resistance state is such that a head-to-head wall at a constriction implies a tail-to-tail wall at the other. The oersted field moves head-to-head and tail-to-tail walls in opposite directions. Then, if it were the dominant mechanism, the two DWs should be pushed simultaneously towards the connecting arms regardless current direction, which contradicts our observations.

5.3 CPP tunnel spin valve Josephson junctions

5.3.1 Motivation

The possibility of changing the magnitude and the sign of a Josephson current by applying an external control has large potentials in superconducting electronics as well as in quantum computing. The use of controllable π-junctions in superconducting quantum interference devices (SQUIDs) represents one of the most promising realization of the quantum bit. One way of obtaining a switch from the 0-phase state to the π-phase state is to apply a voltage along the layer of the normal metal in a S-N-S (superconductor-normal-superconductor) junction [26]. A drawback of using such phase switching in quantum circuits is the necessity to keep the external control switched on, which brings noise into the coherent circuit. In other words, the device does not have memory and comes back to its built-in 0-phase state when the voltage control is switched off.

An alternative way to fabricate non-volatile controllable π-junctions by conventional technologies is to use superconductor/ferromagnet (S/F) heterostructures. The critical Josephson current (I_C) flowing through a S/F heterostructure-based junction strongly depends on the relative orientation of the magnetizations in the F-layers. The exchange field $H_{\text{ex}} = E_{ex}/M_S$ due to the ferromagnetic state can be used to enhance the Josephson critical current or even, under certain conditions, to reverse its sign. The conditions are quite simple to meet. The first condition is that the thickness of the *F*-layers must be much smaller than the condensate penetration into the ferromagnet ξ_F. As far as it goes, it is important to note that the physics underlying this unconventional behavior is different from the π-state induced by the oscillation of the superconducting order parameter in the F-layer in S-F-S or S-F-I-S junctions. The condition can be easily met experimentally by using weak ferromagnets, e.g. ferromagnetic solid solutions like $\text{Cu}_x\text{Ni}_{1\text{-x}}$ and $\text{Pd}_x\text{Ni}_{1\text{-x}}$, in which the exchange energy, and hence ξ_F, is easily controllable via the composition. The second condition is that the thickness of the superconductor must be at least of the order of the superconducting coherence length ξ_S. Under these conditions, the current I_C^P of the parallel (P) configuration is always smaller than the current I_C^{AP} corresponding to the antiparallel (AP) one. Moreover, I_C^P could be negative. The feature important for practical applications is that, unlike the S-F-S or S-F-I-S junctions, the condition for critical current inversion can be achieved by applying an external magnetic field, keeping constant the temperature. The device can be designed so that the state is kept after the field has been removed.

5.3.2 Materials choice

In order to be able to fulfil the condition $t_F << \xi_F$ and, at the same time, have good control on t_F, we chose to use the solid solution $\text{Cu}_x\text{Ni}_{1\text{-}x}$ alloys as F-layers. In these alloys the exchange energy, and hence $\xi_F = \sqrt{(hv_F)/\mu_B H_{ex}}$, is easily controlable via the composition.

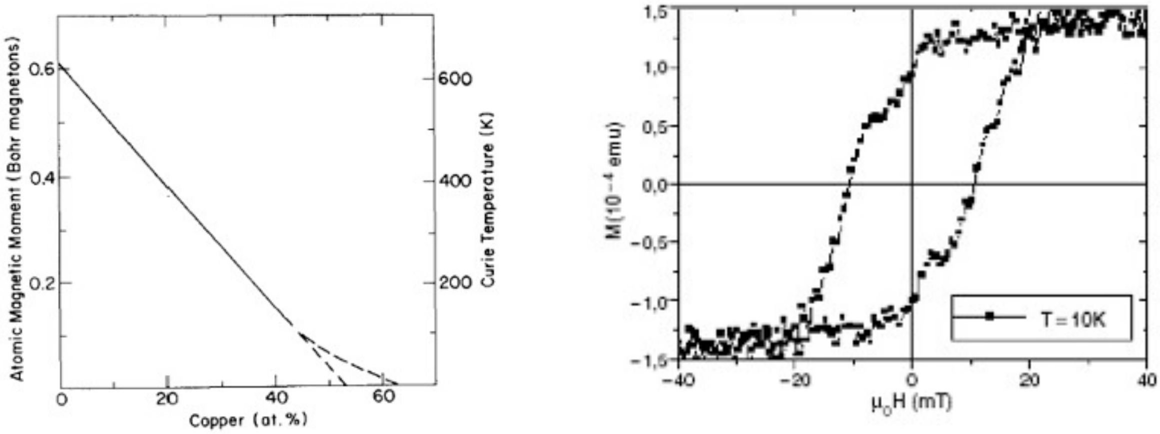

(a) (b)

Fig. 5.17: *(a) Linear changing of moment and Curie Temperature with composition in $Ni_{1-x}Cu_x$ alloys. Taken from [27]. (b) M(H) of a $Ni_{63}Cu_{37}$(8nm)/Nb(24nm)/$Ni_{53}Cu_{47}$(8nm)/Nb(24nm)$]_5$/ $Ni_{63}Cu_{37}$(8nm) multilayer: the structure behaves as a pseudo spin-valve. (From Ruotolo et al. [28]).*

Cu_xNi_{1-x} is particularly of use because the moment increases linearly with x. In particular, the magnetic moment increases of $0.01\mu_B$ per atomic percentage of Cu (see Fig. 5.17a).

In order to get a pseudo spin-valve behavior we chose to grow the two facing ferromagnetic layers with the same thickness $t_{F_1} = t_{F_2} = t_F$, and composition $Cu_{0.47}Ni_{0.53}$ and $Cu_{0.37}Ni_{0.63}$. A previous study, reported in Ref. 28, has revealed that with these two compositions, different coercive fields can be achieved for the two layers of the same thickness at low temperatures (see Fig. 5.17b).

The exact compositions of the alloys were previously checked on thick films by EDS. In order to exclude any significant formation of Ni clusters in the alloys, we measured the Curie temperature of the films by measuring the electrical resistivity as a function of the temperature (Fig. 5.18a). The measured T_{Curie} were ~ 200 K and ~ 50 K for $Cu_{0.37}Ni_{0.63}$ and $Cu_{0.47}Ni_{0.53}$, respectively. The values are in agreement with those reported in the literature

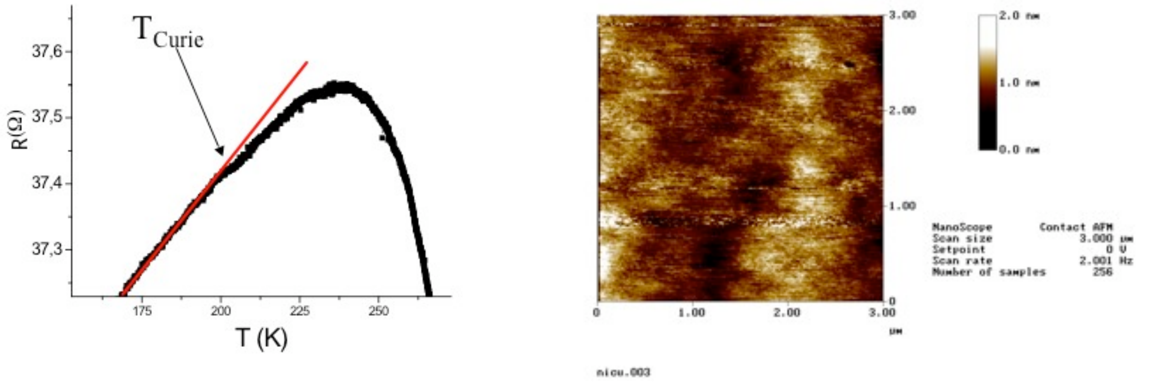

Fig. 5.18: *(a) R(T) of a $Cu_{0.37}Ni_{0.63}$ film. A T_{Curie} ~ 200 K can be estimated. (b) AFM of the top surface of bottommost bilayer of the superconducting spin-valve.*

[27,28] for the same composition of the alloys.

The tunnel barrier was obtained by thermal oxidation of Al. Since the roughness of the bottom bilayer could not be kept below 2 nm, as determined by AFM (Fig. 5.18b), we deposited 5 nm of Al. This means leaving a layer of ~ 3-4 nm of Al between the bottom F-layer and the tunnel barrier in the spin-valve. In other words, the structure sandwiched between the two thick Nb layers is actually a F/N/I/F structure instead of a F/I/F. This inevitably reduces the performances of the devices.

5.3.3 Fabrication process

The devices were fabricated by growing the whole multilayers without breaking vacuum and making all the patterning afterwards by the three-dimensional FIB etching technique explained in Sec. 4.3. Nb / $Cu_{0.37}Ni_{0.63}$ / Al-Al_xO_y / $Cu_{0.47}Ni_{0.53}$ / Nb multilayers were grown on oxidized Si (100) substrates by electron beam deposition. The base pressure in the chamber was always better than $P_b = 4 \times 10^{-8}$ Pa. The Nb was deposited at a rate of 1.5 nm s^{-1} for a total thickness of $t_{Nb} = 250$ nm for both the superconducting electrodes. The CuNi layers were grown by evaporating Cu and Ni at the same time from two different crucibles. The evaporation rates were $r_{Cu} = 0.04$ nm s^{-1} and $r_{Ni} = 0.06$ nm s^{-1} for the $Cu_{0.37}Ni_{0.63}$ whereas $r_{Cu} = 0.05$ nm s^{-1} and $r_{Ni} = 0.05$ nm s^{-1} were used for growing $Cu_{0.47}Ni_{0.53}$. The crucibles were shielded one from another in order to avoid cross contamination. The two facing ferromagnetic layers have thickness $t_{F_1} = t_{F_2} = t_F = 6$ nm. This value is quite smaller than the pair-decay length ξ_F in Nb/Ni_xCu_{1-x} multilayers reported in the literature for similar compositions of the alloys [29,30]. The Al_xO_y tunnel barrier was obtained by thermal oxidation at room temperature of a 5 nm thick Al film evaporated at a rate of $r_{Al} = 0.09$ nm s^{-1} and oxidized in pure oxygen atmosphere of $P_{O_2} = 1 \times 10^5$ Pa for a time of 30 minutes. All the rates of deposition were controlled by a feedback system using quartz crystal oscillators as monitors.

The multilayers were first patterned with standard photolithography and wet chemical etching into a pattern with 20 μm long and 4 μm wide tracks with the associated connections and contact pads. The chemical solution used for the etching was composed by one part of 40% aqueous diluted hydrofluoric acid (HF) and two part of 65% aqueous dilute nitric acid (HNO_3). The samples were then processed in the FEI Dual Beam FIB/SEM Quanta 200 3D with Gallium (Ga) ion source with the 5-step process discussed in Sec. 4.3. A typical final device is shown in Fig. 5.19.

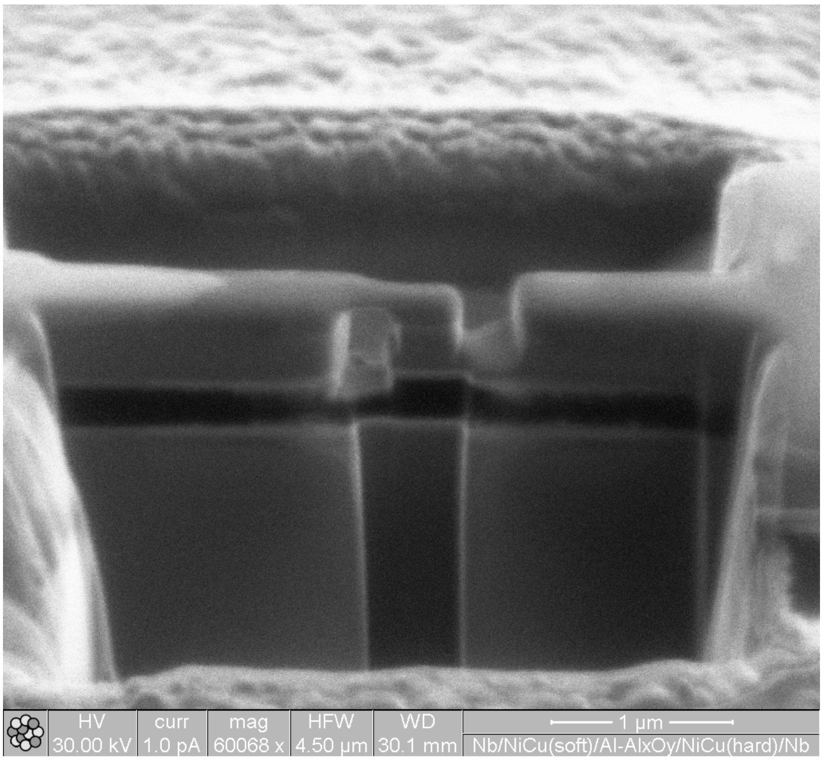

Fig. 5.19: *FIB image of a final device from 65°.*

5.3.4 I-V characteristics

Fig. 5.20a shows a typical *I-V* curve and the corresponding numerical conductance *dI/dV-V*. The *I-V* curve is hysteretic and displays two different measurable critical currents, I_C and I_R. I_C is the maximum current that can be carried before the jump into the high voltage regime. I_R, the retrapping critical current, is the current at which the system returns to the zero voltage

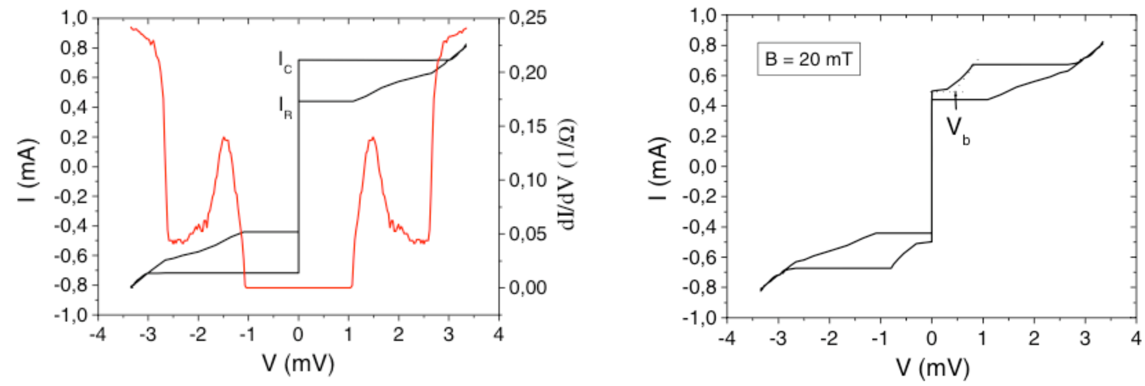

(a) (b)

Fig. 5.20: (a) *Typical I(V) curve measured at T = 4.2 K and the corresponding numerical dI/dV(V). (b) I(V) curve measured at T = 4.2 K in a magnetic field of 20 mT. From the knee, an intrinsic capacitance of 0.16 fF is estimated for this junction.*

state. The numerical conductance has been calculated after suppressing the critical currents. As can be seen, the subgap voltage V_g is around 1.5 mV. This reduction of the energy gap, due to proximity effect at the S/F interfaces, is consistent with that reported in other studies [31] on S/F/I/S junctions with composition of the CuNi alloy similar to our weaker one.

The *I-V* characteristic is typical of a resistively shunted Josephson junction with a quality factor $Q = 4I_C/\pi I_R = 2$ (at T = 4.2 K). Although we cannot completely exclude so far that this low quality factor is due to shorts on the sidewalls that persist in spite of the accurate post-cleaning, there are at least three experimental observations that suggest that pinholes or localized single particle states in the tunnel barrier can be present. The Josephson current density is about 500 A/cm^2, which is quite larger than expected for our oxidation parameters. There is a low modulation of the *Ic* by the field *H* (see following section). The maximum changing in tunneling MR is only 0.07 %, which is rather smaller than expected. These experimental results are all consistent with the presence of highly conducting channels for electron transport in the barrier.

If the transition in the shape of the *I-V* curve (see Fig. 5.20b) that we observe when applying a magnetic field is due to standard Coulomb blockade effect (see discussion in Sec. 5.3.6), a precise estimation of the intrinsic capacitance of the junctions can be made. For example, for the junction whose *I-V* is reported in Fig. 5.20b, with a field of 20 mT applied, a knee is present at V_b = 0.5 mV. The measured V_b must correspond to $e/2C$ that yields C = 0.16 fF. The intrinsic capacitance must be also given by $C = \varepsilon_0\varepsilon_r A/d$ with A area of the junction and d thickness of the tunnel barrier. The junction area, obtained by FIB imaging is ~ 0,15 μm^2. Using a typical value for Al_xO_y of the dielectric constant ε_r ~ 10 [32], the estimated barrier thickness is of the order of tens of nanometers which is impossible for our junctions, given the high Josephson current density. The mismatch must be due to a significant lower effective area of the device, which is unlikely to be caused by Ga diffusion or shorting veils on the sidewalls. Another way to see it is considering the very small value of the measured normal resistance (R_n) of the junctions. Considering, for example, the junction of Fig. 5.20b, the normal resistance (evaluated at a voltage $V >> 2\Delta$) is R_n = 10 Ω. This value for such a small tunnel junction definitely indicates the presence of other conduction channels in the barrier. The question is whether the shorting takes place on the sidewalls or into the barrier. If thin Nb veils were the reason of the shorts, the resputtered Nb would be highly polluted with Ga, Cu and even ferromagnetic Ni. This makes very unlikely that the shorting veils are superconducting at T = 4.2 K. According with the size of the devices and the used oxidation parameters, the intrinsic resistance (R_i) of the junctions must be in the range of 1 – 100 kΩ.

This is also consistent with the condition $R_i >> R_Q = h/(2e)^2 \cong 6$ kΩ for the Coulomb blockade to set in, where R_Q is the so-called quantum resistance. Given the value of the measured R_n, we can assume a shorting parallel resistance value of 10 Ω. If the shorting took place on the sidewalls, even assuming a strongly underestimated resistivity of thin Nb in normal state at 4.2 K of ~ 1 μΩcm [33,34] and a shorting length of the barrier thickness, a resistance of 10 Ω would require a thickness of the veils greater than the lateral dimension of the junctions. This leads once again to the conclusion that superconducting shorts must be present into the barrier.

5.3.5 Ic(H) and R(H) characteristics

The magnetic pattern $I_C(H)$ in Fig. 5.21 has a hysteretic behavior that is clearly correlated with the MR measured at a current bias of 2.5 mA ($V > V_g$). Increasing H from the negative lowest field value, for positive values of H, as the soft F-layer reverses its magnetization, the MR rises and so does I_C. The maximum value of I_C corresponds to the maximum changing in MR. After the relative orientation of the F-layers magnetization has reached its maximum, the MR starts decreasing and so, then again, does I_C. The reduction of MR due to the reversing of the hard F-layer is rapidly overwhelmed by the direct action of the field on the superconducting films that tends to increase the resistance of the whole structure. When lowering H from the positive upper field value, the spin-valve barrier remains in the parallel state until the negative coercive field of the soft F-layer is reached and the reversing of its magnetization starts taking place.

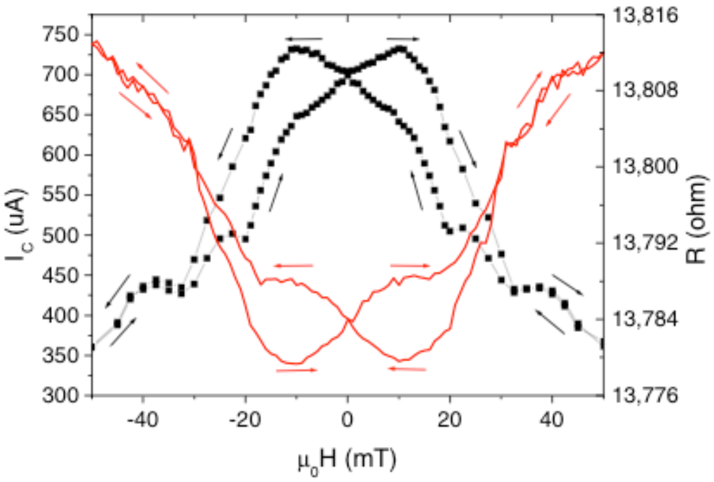

Fig. 5.21: *Dependence of (black) Josephson critical current I_C and (red) magnetoresistance MR at T = 4.2 K on magnetic field H for a junction of area 400 × 400 nm^2. Field sweep direction is indicated by the arrows.*

5.3.6 Coexistence of Coulomb blockade effect with Josephson tunnelling

Finally, let us discuss the transition in the shape of the *I-V* curve in the presence of a magnetic field shown in Fig. 5.20b. This kind of transition is rather common [35,36] in ultrasmall Josephson junctions when the charging energy $E_C = e^2/2C$ becomes larger than the Josephson energy $E_J = h\Delta/8e^2R_i$ (regime of very small Josephson energy), although it is usually observed at very low temperatures and large magnetic fields. It is attributed to the coexistence of a Coulomb blockade effect with the Josephson tunnelling. When the conditions for the Coulomb blockade to be observed are satisfied ($E_C > k_BT, R_i > R_Q$), if the Josephson coupling is weakened by a magnetic field, the charging energy dominates on the Josephson energy and the aspects of the Coulomb blockade come out. Assuming a minimum value of $R_i = R_Q$, an upper limit of the Josephson coupling energy can be estimated for our junctions from the measured value of the energy gap as $E_J < 1$ K, when no external field is applied. Assuming the value of the intrinsic capacitance previously estimated, the charging energy is $E_C = 5.8$ K which is smaller but comparable with the Josephson energy. A relatively small magnetic field further reduces the Josephson coupling, and hence E_J. On the other hand, the switching towards parallel orientation of the F-layers in the barrier is known to facilitate the reduction of the Josephson coupling, which can lead to the regime of very small Josephson coupling energy with relatively small applied magnetic fields. Once the typical Coulomb knee sets in, the value of V_b was found to be insensitive to magnetic field and temperature (above 4.2 K). It is finally worth noticing that, given the very low value of the intrinsic capacitance, the condition $E_C > k_BT$ for the Coulomb blockade to be observed is satisfied even at $T = 4.2$ K, whereas lower temperatures are usually requested. Such a low value of the intrinsic capacitance suggests the presence of quantum traps in the barrier, capacitively coupled with the junction electrodes. Repeated filling of single-particle states is a rather generic phenomenon [37]. It has been observed in systems where, either by accident or by specific design, quantum dots exist between two electrodes.

References

[1] J. Z. Sun, D.W. Abraham, R.A. Rao, and C. B. Geballe, *Appl. Phys. Lett.* **74**, 3017 (1999).

[2] L. Abad, B. Martinez, and L. Balcells, *Appl. Phys. Lett.* **87**, 212502 (2005).

[3] J. W. Freeland, K. E. Gray, L. Ozyuzer, P. Berghuis, E. Badica, J. Kavich, H. Zheng, and J. F. Mitchell, *Nat. Mater.* **4**, 62 (2005).

[4] D. C. Worledge and T. H. Geballe, *Appl. Phys. Lett.* **76**, 900 (2000).

[5] A. Plecenik, K. Fröhlich, J. P. Espinós, J. P. Holgado, A. Halabica, M. Pripko, and A. Gilabert, *Appl. Phys. Lett.* **81**, 859 (2002).

[6] U. Scotti di Uccio, B. Davidson, R. Di Capua, F. Miletto Granozio, G. Pepe, P. Perna, A. Ruotolo, M. Salluzzo, *J. Alloy Compd.* **423**, 228 (2006).

[7] Y. Suzuki, H.Y. Hwang, S-W. Cheong, and R.B. van Dover, *Appl. Phys. Lett.* **71**, 140 (1997).

[8] J. O'Donnel, M.S. Rzchowski, J.N. Eckstein, and I. Bozovic, *Appl. Phys. Lett.* **72**, 1775 (1998).

[9] B. D. Cullity, *Introduction to magnetic materials* (Addison-Wesley, Reading, MA, 1972).

[10] K. Steenbeck, T. Habisreuther, C. Dubourdieu and J.P. Sénateur, *Appl. Phys. Lett.* **80**, 3361 (2002).

[11] *American Institute of Physics Handbook*, edited by D.E. Gray (McGraw-Hill, New York, 1972).

[12] X.W. Li, A. Gupta, Gang Xiao and G.Q. Gong, *Appl. Phys. Lett.* **71**, 1124 (1997).

[13] R.J.M. van de Veerdonk, J. Nowak, R. Meservey, J.S. Moodera, W.J.M. de Jonge, *Appl. Phys. Lett*. **71**, 2839 (1997).

[14] J.M. De Teresa, A. Barthélémy, A. Fert, J.P. Contour, F. Montaigne, P. Seneor, *Science*, **286**, 507 (1999).

[15] M. Ziese, S. Sena, C. Shearwood, H.J. Blythe, M.R.J. Gibbs, and G.A. Gehring, *Phys. Rev. B* **57**, 2963 (1998).

[16] O. Céspedes, S. M. Watts, and J.M.D. Coey, K. Dörr, M. Ziese, *Appl. Phys. Lett.* **87** 083102 (2005).

[17] O. Céspedes, E. Clifford, and J.M.D. Coey, *J. Appl. Phys*. **97** 064305 (2005).

[18] C. Ruster, T. Borzenko, C. Gould, G. Schmidt, and L.W. Molenkamp, X. Liu, T. J.Wojtowicz, and J. K. Furdyna, Z.G. Yu and M. E. Flatte, *Phys. Rev. Lett.* **91**, 216602 (2003).

[19] A. D. Giddings, M. N. Khalid, T. Jungwirth, J.Wunderlich, S. Yasin, R. P. Campion, K.W. Edmonds, J. Sinova, K. Ito, K.-Y. Wang, D. Williams, B. L. Gallagher, and C. T. Foxon, *Phys. Rev. Lett.* **94**, 127202 (2005).

[20] Schulte, M.A. James, L.H. Tjeng, P.G. Steeneken, G.A. Sawatzky, R. Suryanarayanan, G. Dhalenne, A. Revcolevschi, *Phys. Rev. B* **64**, 134428 (2001).

[21] R.H. Fowler and L.W. Nordheim, *Proc. Roy. Soc.* (London) **119**, 173 (1928).

[22] *SRIM computer program*, available at www.srim.org.

[23] R.Y. Gu, L. Sheng, and C.S. Ting, *Phys. Rev. B* **63**, 220406 (2001).

[24] Z. Li and S. Zhang, *Phys. Rev. B* **70**, 024417 (2004).

[25] A. Aharoni, *J. Appl. Phys*. **83**, 3432 (1998).

[26] J.J.A. Baselmans, A.F. Morpurgo, B.J. van Wees and T.M. Klapwijk, *Nature* (London) **397**, 43 (1999);

[27] J. Q. Zheng and J. B. Ketterson, *J. Appl. Phys.* **53**, 3150 (1982).

[28] A. Ruotolo, G. P. Pepe, C. Bell, C. W. Leung and M. G. Blamire, *Supercond. Sci. Technol.* **18**, 921 (2005).

[29] V.V. Ryazanov, V.A. Oboznov, A. Rusanov, A.V. Veretennikov, A.A. Golubov and J. Aarts, *Phys. Rev. Lett.* **86**, 2427 (2001).

[30] A. Rusanov, R. Boogaard, M. Hesselberth, H. Sellier, J. Aarts, *Physica C* **369**, 300 (2002).

[31] G.P. Pepe, R. Latempa, L. Parlato, A. Ruotolo, G. Ausanio, G. Peluso, A. Barone A.A. Golubov, Ya.V. Fominov, M. Yu.Kupriyanov, *Phys. Rev. B* **73**, 054506 (2006).

[32] S. Guha, E. Cartier, N. A. Bojarczuk, J. Bruley, L. Gignac and J. Karasinski, *J. Appl. Phys.* **90**, 512 (2001).

[33] Q. D. Jiang, Y. L. Xie, W. B. Zheng, H. Gu, Z. Y. Ye, K. Wu, J. L. Zhang, C. Y. Li, D. L. Yin, *J. Phys.:Cond. Mat.* **2**, 3567 (1990).

[34] A. I. Gubin, K. S. Il'in, S. A. Vitusevich, M. Siegel, N. Klein, *Phys. Rev. B* **72** 64503 (2005).

[35] M. Iansiti, M. Tinkham, A. T. Johnson, W. F. Smith, C. J. Lobb, *Phys. Rev. B* **39**, 6465 (1989).

[36] T. A. Fulton and G.J. Dolan, *Phys. Rev. Lett.* **59**, 109 (1987).

[37] R. Berkovits, F. von Oppen, and Y. Gefen, *Phys. Rev. Lett.* **94,** 076802 (2005).

Conclusions and outlook

In this thesis some categories of novel spintronic devices, connected with high-end technological applications, have been produced and investigated. Experimental results have been interpreted in the framework of micromagnetics, which is capable of properly describing magnetic phenomena on sub-micron scale.

Three kinds of devices have been investigated.

In the first kind, we studied the current perpendicular to plane (CPP) magnetotransport behavior of $La_{0.7}Sr_{0.3}MnO_3/Ni_{80}Fe_{20}$ in low magnetic fields. We demonstrated that, because of the presence of a significatively thick dead layer, the ferromagnetic layers show only a weak exchange coupling. The possibility of reversing the layers independently was exploited to fabricate magnetoresistive devices. The devices show the unique feature of a low field magnetoresistive effect. We were for the first time able to use the dead layer of a manganite as an intrinsic spacer. The MR shown by the devices is still small because of the presence of a rather thick highly-resistive dead layer. A suitable choice of the dead layer thickness should allow the fabrication of devices with high MR ratio in which any metal or insulating deposited spacer is needed.

We studied the effect of a current over domain walls in $La_{0.7}Sr_{0.3}MnO_3$ nano-constrains patterned by Gallium (Ga) focused ion beam. An insight into the effect of Ga implantation on the current-voltage characteristics of LSMO nano-constrictions was given with the help of TRIM (acronym for Transport and Ranges of Ions in Matter) calculations. Planar spin-valve devices were structured in order to study the effect of the bias current on the displacement of DWs pinned at the nano-constrictions. In devices showing diffusive transport, we found that the DW depinning threshold depends on the transverse anisotropy constant of the region toward which the DW is depinned. This suggests that, for transverse walls, the DW threshold, and likely its velocity, can be simply controlled by changing the lateral track width on submicron-scale. If the electrodes have significatevely different magnetic anisotropy, the DW can be compressed by either an external field or a polarized current resulting in an enhanced DW resistance.

Applications in magnetic field sensing and magnetic data storage can be envisaged for the devices produced.

Finally, we set up a new fabrication process making use of a focused ion beam microscope in order to produce superconducting tunneling spin-valve Josephson junctions.

The structure investigated was a $S/F_1/I/F_2/S$ Josephson junction where the superconducting (S) electrodes were Niobium (Nb) and the insulator (I) barrier was Aluminum oxide (Al_xO_y). The structure sandwiched between the two thick Nb electrodes was a magnetic tunnel junction (MTJ) in which the ferromagnetic layers were Cu_xNi_{1-x} with different composition but of the same thickness. The compositions were chosen so that the F-layers reversed at different applied magnetic fields.

First of all, we demonstrated that, despite the common knowledge, good quality tunnel junctions can be made by focused ion beam milling without any other post-processing. The devices showed an enhancement of the Josephson critical current when the sandwiched magnetic tunnel barrier is in antiparallel state as compared to the case of parallel orientation. Moreover, when the spin-valve barrier was switched towards the parallel state, the Josephson coupling was rapidly weakened and the system showed Coulomb blockade of the supercurrent.

A systematic investigation of such a structure with different F-layer thickness and composition will be the next step forward the realization of a controllable non-volatile π-junction, i.e. a superconducting device in which the sign of the Josephson current can be reversed by a removable external control. This kind of device is of potential in quantum computing applications.